

Rock-Mass Classification in Tunneling
based on Seismic Velocities and Tunnel-Driving Data
using Support Vector Machines

Dissertation

zur Erlangung des akademischen Grades
doctor rerum naturalium (Dr. rer. nat.)

eingereicht im Fachbereich Geowissenschaften
der Freien Universität Berlin

von

Aissa Jemela Rechlin

Berlin, Dezember 2012

Tag der Disputation: 07.12.2012

Gutachter

Prof. Dr. Frank Schilling
Freie Universität Berlin, Karlsruher Institut für Technologie

Prof. Dr. Thomas Bohlen
Karlsruher Institut für Technologie

Eidesstattliche Erklärung

Hiermit versichere ich, dass ich die vorliegende Arbeit selbständig verfaßt und ohne Benutzung anderer als der angegebenen Hilfsmittel angefertigt habe. Die aus fremden Quellen direkt oder indirekt übernommenen Gedanken sind durch entsprechende Quellenangaben kenntlich gemacht. Diese Arbeit hat in gleicher oder ähnlicher Form noch keiner Prüfungsbehörde vorgelegen.

Aissa Jemela Rechlin, März 2013

Abstract

The continuously increasing demand on safe and cost-efficient tunnel constructions world-wide has led to the development of seismic systems as a predictive tool ahead of tunneling. These seismic systems are either specialized for hard rock or soft rock excavations. In this study, the hypothesis is tested, if artificial intelligence approaches are capable to deduce automatically and in real time critical rock parameters out of seismic observations. The hypothesis is tested in hard rock environments, using combined geological and seismic observations of the Faido Adit (Gotthard Base Tunnel - Switzerland) and the Glendoe Tunnel (Hydro Electric Power Plant near Loch Ness - Scotland UK).

The evaluation of geotechnical rock-mass behavior in hard rock is commonly based on a rock-mass classification. Especially, a fast assessment of the hard rocks' bearing capacity is mandatory to quickly ascertain the required structural tunnel support. Therefore, a user-oriented geotechnical interpretation of seismic results in real time is tested. Within this study, a support vector machine (SVM) is applied to the discovery and automated prediction of relationships between seismic P- and S-wave velocities with heuristic rock-mass classification systems, such as the widely used Rock Quality Designation (RQD) index or the Rock Mass Rating (RMR) factor. The data available for this task were acquired during two field surveys in hard rock using the Integrated Seismic Imaging System ISIS and geotechnical mapping of the rock mass. The first survey was carried out in the gneisses of the Faido Adit, which is part of the Gotthard Base Tunnel in Switzerland. Seismic velocity data from a 2-D tomography with a cells size of 0.5 m in direction of the excavation along a 448 m long seismic profile have been used. The second seismic survey took place along a 300-m long profile in quartz schists and quartz-mica schists in the headrace tunnel of the Glendoe Hydro Electric Power Plant in the Scottish Highlands. The Glendoe Tunnel was excavated with a tunnel-boring machine (TBM), such that adaptations had to be made to the seismic setup of the TBM-integrated seismic measurements. These adaptations led to a 1-D tomography with a cell size in tunnel direction of 4 m and therefore, to a considerably reduced resolution in the available seismic velocity data, compared to the Faido Adit data set. Thus, the SVM approach was applied separately to the two data sets. As there may exist some direct or indirect link between rock-mass classes and tunnel-driving parameters, such as the thrust force, the penetration rate, the cutter-head torque and the cutter-head speed, these properties were included in the data base of the Glendoe Tunnel survey. The tunnel-driving parameters exhibit a much higher spatial resolution than the seismic data, such that their information content was first explored by training and testing a SVM solely

on this data with a resolution of 1 m. In both data sets, 3 RQD classes and 2 RMR classes were distinguished. Two fundamentally different results are achieved during rock-mass classification based on the data sets from the Faido Adit and the Glendoe Tunnel:

1. Based on high-resolution seismic data from the Faido Adit, the classification of RQD or RMR classes proved feasible.
2. Based on either tunnel-driving data, or else tunnel-driving and seismic data combined, from the Glendoe Tunnel with lower resolution, the RQD and RMR classification did not provide satisfying results.

The variability in the rock-mass quality, expressed either as RQD or RMR, is extremely low for the Faido Adit, leading to strong proximity of most data samples to the class boundaries. The detection of patterns that link the rock-mass classes to the seismic velocities in the Faido Adit data set is therefore remarkable, especially for the small number of training samples available and despite a strong tendency to overfit.

For the Glendoe Tunnel, the training and testing of the SVM reveals that the classes were not or poorly classified by the automated classification approach. The models based exclusively on tunnel-driving parameters show severe cases of overfitting and extremely low generalization ability. These results do not rule out that higher order correlations exist between tunnel-driving parameters and rock-mass classes in general, but no evidence on this has been discovered in this study.

The additional use of seismic body-wave velocities in the Glendoe Tunnel has been inevitably accompanied by a significant reduction of the data set. Adding the seismic velocities to the data base did not influence the classification result positively. This led to the assumption that the data set is by far too small for a proper learning process, such that no rules were learned from the data set and the prediction failed in consequence. The quality and spatial resolution of the seismic observations is therefore crucial for the reliability of the prediction of rock-mass classes. The quality and cell size of the underlying seismic tomography strongly depends on the seismic layout during the data acquisition, such that the careful planning of the seismic survey can be determined as a key requirement for the success of a fast and automated rock-mass classification and the detection of hazardous zones in the rock mass.

Nevertheless, even with the limited size of the available data sets, it was possible to show that SVMs are a powerful tool in real time expert systems for geotechnical applications. It has been proven within this study that it is possible to predict rock-mass classes out of high resolution seismic data with high accuracy.

Zusammenfassung

Die Entwicklung speziell auf den Tunnelbau abgestimmter seismischer Systeme zielt darauf ab, den stetig wachsenden Ansprüchen an die Sicherheit im Tunnelbau, bei gleichzeitiger Kostenreduktion, gerecht zu werden. Diese seismischen Methoden sind auf die speziellen Anforderungen im Hart- oder Lockergestein angepasst. In der vorliegenden Arbeit wird die Hypothese getestet, dass Methoden der Künstlichen Intelligenz genutzt werden können, um automatisiert und zeitnah kritische Gesteinsparameter aus seismischen Beobachtungen abzuleiten. Zur Überprüfung dieser Hypothese wurden seismische und geologische Daten aus zwei Feldeinsätzen in Hartgestein verwendet, und zwar aus dem Faido Zugangsstollen (Gotthard Basis Tunnel - Schweiz) und dem Glendoe Tunnel (Wasserkraftwerk am Loch Ness - Schottland).

Besonders im Hartgestein erfolgt eine zeitnahe Einteilung der geotechnisch relevanten Eigenschaften meist über Systeme zur Gesteinsklassifikation. Die geotechnische Klassifikation von Gesteinen dient vor allem der Abschätzung der Standfestigkeit des Gebirges vor Ort, als wichtiger Voraussetzung zur Ermittlung des nötigen Ausbaus und damit für die Stabilität und Sicherheit des Tunnels. Da eine umfassende, anwendungsorientierte und zeitnahe, geotechnische Interpretation der im Hartgestein gewonnenen seismischen Daten bisher nicht gewährleistet ist, wurde in der vorliegenden Arbeit eine auf seismischen Daten basierende Routine zur automatischen und zeitnahen geotechnischen Gesteinsklassifikation mit Support Vektor Maschinen (SVMs) entwickelt. Der Ansatz wurde auf zwei verbreitete Systeme zur Gesteinsklassifikation angewendet: den Rock Quality Designation (RQD) Index und den Rock Mass Rating (RMR) Faktor. Datensätze aus zwei Feldeinsätzen im Hartgestein, die mit dem Integrated Seismic Imaging System ISIS durchgeführt wurden, standen hierfür zur Verfügung. Der erste Feldeinsatz erfolgte über eine Profillänge von 448 m in den Gneisen des, im Sprengvortrieb errichteten, Faido Zugangsstollens zum Gotthard Basis Tunnel (südliche Schweiz). Die seismischen Geschwindigkeiten entlang des Profils im Faido Zugangsstollens basieren auf einer 2D-Tomographie mit einer Zellgröße entlang der Tunnelachse von 0.5 m. Der zweite Feldeinsatz wurde in Quarzschiefern und Quarzglimmerschiefern entlang eines 300 m langen Profils im Triebwassertunnel des Wasserkraftwerkes Glendoe (schottisches Hochland) durchgeführt. Der Glendoe Tunnel wurde maschinell vorgetrieben, wodurch entsprechende Anpassungen in der Geometrie der seismischen Datenakquisition nötig wurden. Diese Anpassungen führten zu einer verringerten Qualität und Auflösung der seismischen Daten, woraus eine 1D-Tomographie mit 4 m Zellgröße entlang der Tunnelachse berechnet wurde. Die Datensätze des Faido

Stollens und des Glendoe Tunnels wurden daher getrennt evaluiert.

Es wurde ein Zusammenhang zwischen Vortriebsparametern der Tunnelbohrmaschine, wie Vortriebspresenkraft, Penetration sowie Drehmoment und Drehzahl des Schneidrads, mit dem RQD und RMR angenommen. Die Vortriebsparameter wurden daher in den Ansatz zur automatischen Vorhersage von Gesteinsklassen integriert. Da die Vortriebsparameter eine sehr viel höhere Auflösung als die seismischen Daten besitzen, wurden diese über 1 m große Intervalle gemittelt und zuerst separat betrachtet. In beiden Feldstudien wurden drei RQD-Klassen, sowie zwei RMR-Klassen unterschieden. Zwei grundsätzlich verschiedene Ergebnisse wurden für die Gesteinsklassifikationen auf Grundlage der Daten aus dem Faïdo Zugangstollen oder dem Glendoe Tunnel erreicht:

1. Basierend auf den höher aufgelösten seismischen Daten des Faïdo Zugangstollens konnte eine erfolgreiche Gesteinsklassifikation sowohl für die RQD als auch für die RMR-Klassen vorgenommen werden.
2. Basierend auf den niedriger aufgelösten Daten des Glendoe Tunnels konnten keine zufriedenstellenden Klassifikationsergebnisse erreicht werden. Dies gilt sowohl für eine getrennte Betrachtung von Vortriebsparametern mit einer höheren Auflösung von 1 m, als auch für den kombinierten Datensatz aus seismischen Daten und Vortriebsparametern mit einer Auflösung von 4 m.

Die Variabilität des RQD und RMR im Datensatz des Faïdo Stollens ist gering. Die erfolgreiche Klassifikation ist daher, insbesondere trotz der geringen Anzahl von zur Verfügung stehenden Datenpunkten und einer deutlichen Tendenz des SVM-Modells hin zu Überanpassung an die Trainingsdaten, bemerkenswert. Eine Analyse der Ergebnisse zum Glendoe Tunnel zeigte, dass die Klassen nicht oder sehr schlecht klassifiziert wurden. Die SVM-Modelle der RQD und RMR Klassifikation, die ausschließlich auf Vortriebsparametern basieren, zeigten extreme Anpassung an die Trainingsdaten und geringe Generalisationsfähigkeit. Diese Ergebnisse schließen zwar nicht aus, dass generell ein Zusammenhang zwischen Vortriebsparametern und Gesteinsklassen bestehen kann, in dieser Arbeit konnte dies jedoch nicht verifiziert werden. Der Einbezug der seismischen Geschwindigkeiten, mit einhergehender Reduktion der Datensatzgröße, ergab keine positive Beeinflussung des Ergebnisses. Dies lässt den Schluss zu, dass der Datensatz eine zu geringe Anzahl und Qualität an Datenpunkten aufweist, so dass keine Regeln für die Klassifikation aus den Daten abgeleitet werden konnten und eine Vorhersage in der Konsequenz nicht möglich ist. Die Qualität und räumliche Auflösung der Tomographie ist daher entscheidend für die Aussagekraft einer Vorhersage von Gesteinsklassen. Dies hängt stark von der Anordnung der Quellen und Empfänger während der seismischen Datenakquisition ab. Eine umsichtige Planung der Datenakquisition ist daher unerlässliche wichtige Voraussetzung für eine

erfolgreiche automatisierte Gesteinsklassifikation.

Trotz einer stark limitierten Größe der zur Verfügung stehenden Datensätze konnte gezeigt werden, dass SVMs als mächtiges Werkzeug in einem Expertensystem für geotechnische Fragestellungen genutzt werden können. Es konnte in dieser Arbeit gezeigt werden, dass eine genaue Vorhersage von Gesteinsklassen, basierend auf hochauflösenden seismischen Messungen, möglich ist.

Contents

Abstract	I
Zusammenfassung	III
1 Introduction	1
1.1 Motivation	2
1.2 Aim	3
1.3 Selection of a Self-Learning Algorithm	4
1.4 Geological Rock-Mass Properties	8
1.4.1 Calculation of RMR and RQD	9
1.5 Tunnel-Driving Data	15
1.5.1 Operating Mode of an Open Gripper Tunnel-Boring Machine	15
1.6 Relationships between Rock Quality, Seismic Velocities and Tunnel-Driving Parameters	18
1.6.1 Seismic Velocities and Rock-Mass Behavior	18
1.6.2 Tunnel-Driving Parameters and Rock-Mass Behavior	23
1.7 Seismic Systems in Tunneling	24
1.8 Basic Concept of Support Vector Machines	27
2 Field Investigations	35
2.1 Geological Setting	35
2.1.1 The Faido Adit	35
2.1.2 Geological Setting of the Glendoe Tunnel	41
2.2 Seismic Measurements	48
2.2.1 Seismic Data Acquisition in the Faido Adit	48
2.2.2 Seismic Data Acquisition in the Glendoe Tunnel	49
2.3 Acquisition of Tunnel-Driving Data in the Glendoe Tunnel	54
3 Statistical Evaluation	57
3.1 Statistical Evaluation of the Faido Data Set	57
3.2 Statistical Evaluation of the Glendoe Data Set	62
3.2.1 Final Remarks	69

4	Development of a SVM for Rock-Mass Classification	71
4.1	Programming Environment	81
5	Results of Rock-Mass Classification using SVMs	83
5.1	RQD Prediction on the Faido Adit Data Set	84
5.2	RMR Prediction on the Faido Adit Data Set	90
5.3	RQD Prediction in the Glendoe Tunnel 1-m Data Set	93
5.4	RMR Prediction on the Glendoe Tunnel 1-m Data Set	96
5.5	RQD Prediction on the Glendoe Tunnel 4-m Data Set	101
5.6	RMR Prediction on the Glendoe Tunnel 4-m Data Set	103
6	Discussion	107
7	Conclusion	115
8	Outlook	117
	Acknowledgements	119
	References	121
	List of Figures	132
	List of Tables	136
	Appendices	138
	A Nomenclature	141
	B Field Surveys	145
	C Statistics	147
	Curriculum Vitae	154

1 Introduction

The rapid development of infrastructure in both industrialized and developing countries has led to an ever-increasing amount of tunnel excavation in host rocks considered to be geotechnically difficult. These rocks have, for example, strong variations in rock-mass characteristics, or structural features such as faults and fracturing. Detailed knowledge of such obstacles enables engineers to make adjustments to the excavation procedure and the tunnel design as the excavation proceeds, thereby making optimal use of time and resources. The cost-efficiency and, most importantly, the safety of tunneling, is thus strongly influenced by an accurate knowledge of the host rocks' geotechnical behavior.

Traditionally, the determination of the geotechnical rock-mass characteristics along the projected roadway has been done via exploratory wells or surface investigations, such as geological mapping and geophysical profiling. These approaches may produce either high-resolution data sets with a restricted area of validity (exploratory wells), or low-resolution coverage of the entire project (e.g., seismic profiling). Consequently, a detailed knowledge of the geological variations directly along the tunnel axis is often lacking. As a result, increasing importance is attached to research into high-resolution, non-destructive subsurface geophysical methods, especially seismic exploration (among others, Kneib et al., 2000; Brückel et al., 2008; Bruns et al., 2008; Dickmann, 2008; Lüth et al., 2008a). These methods are usually adapted to the needs of specific excavation methods, as the requirements for tunnel excavation and structural rock support in hard rock and soft rock differ strongly. In consequence, the seismic-while-drilling data needs to be examined with respect to its informative value regarding the rock-mass stability (among others, Otto et al., 2002; Ashida, 2001), in order to become of importance for on-site engineering decision-making. Especially for tunneling in hard rock, where the rock-mass stability is particularly dependent on the properties of the discontinuity network, a technological gap that needs to be bridged exists between seismic data acquisition and interpretation.

The Integrated Seismic Imaging System (ISIS) (Borm et al., 2003; Bohlen et al., 2007) has been developed for hard rock excavations using different excavation methods, such as drill and blast or tunnel-boring machine excavation. The seismic images obtained with ISIS reflect changes in rock mass up to 200 m in front of the tunnel face. For the development of an interpretation system, seismic data acquired with ISIS at two different test sites in hard rock is available for this study: The Faido Adit is part of the Gotthard Base Tunnel in Switzerland and was excavated by drill and blast, while the headrace tunnel of the

Glendoe Hydro Electric Power Plant in the British Caledonides was excavated using a tunnel-boring machine.

Depending on the mode of excavation and the rock-mass behavior, the excavation may proceed at an advance speed of 40 to 60 m per day. The high resolution seismic data must therefore be processed and interpreted in the short time interval of a few hours or days to be relevant for the planning of the excavation. Moreover, the engineers on-site are usually not trained to interpret the seismic data. Thus, the interpretation should be done by an automated expert system to facilitate efficient engineering decision making. To setup such an interpretation system, a self-learning algorithm has been applied to the available seismic data from the Faido Adit and the Glendoe Tunnel.

For the evaluation of the seismic data in regard to the geotechnical rock-mass behavior, two widely used rock-mass classification systems, the Rock Mass Rating and the Rock-Quality Designation, are used. These rock-mass classification systems have been developed heuristically during practical geotechnical applications over the past few decades for a comprehensive evaluation of the rock-mass behavior.

During tunnel excavation by tunnel-boring machines, as in the Glendoe Tunnel, a wide range of tunnel-driving parameters is automatically acquired, such as the thrust force, the penetration rate, the cutter-head torque and the cutter-head speed. Unlike the Glendoe Tunnel, information on the host rock is often not available from direct mapping at most tunnel construction sites, where tunnel-boring machines (TBM) are used. This results from the increasing use of segmental lining and closed-mode excavation. At these construction sites, the information about changes in rock conditions is usually acquired by estimating changes in tunnel-driving parameters (Exadaktylos et al., 2008; Fukui and Okubo, 2006; Kim et al., 2008; Thuro and Spaun, 1997; Mito et al., 2003; Poisel et al., 1999b; Sapigni et al., 2002; Schlicke et al., 2005; Thuro and Brodbeck, 1998; Müller, 2007), though the correlation between geological and tunnel-driving parameters is a field of ongoing research. To account for this development, and because a direct comparison between geotechnically important geological features and tunnel-driving data is possible for the Glendoe Tunnel, tunnel-driving parameters are incorporated in the automated rock-mass classification of this data set.

1.1 Motivation

The classification of rocks in geoenvironmental applications is the basis for safe underground construction work (e.g., tunnel construction) because the reinforcement is designed according to the geotechnical specifics of the rock mass. Seismic properties and tunnel-driving

parameters reveal information on the quality of a rock mass in terms of a particular engineering purpose, such as tunnel construction. The dependencies of seismic or tunnel-driving properties on single rock-mass properties and also on the engineering rock-mass quality has been investigated in many research projects; however, in real-world applications there is a high expected noise level and the dependencies may superimpose on each other in unknown ways. Therefore, stochastic ascertainability becomes difficult for the available parameter sets and uncertainty occurs in the parameter interaction patterns. This dynamic system of inter-dependencies among different rock-mass properties, seismic velocities and tunnel-driving data may be best captured and interpreted using a computer based self-learning algorithm. One of the most promising families of algorithms for the application to real data sets is that of the support vector machines (Vapnik, 1998), which present a series of useful features for pattern analysis in data sets. They have been successfully applied to bioinformatics (Mohr et al., 2008), text processing (Joachims, 1998), image processing for rock-fracture tracing (Wang and Liao, 2007), time series analysis (Rüping, 2001) and environmental applications (Kanevski et al., 2009; Welle, 2009) or remote sensing (Ge et al., 2008), and geohazard analysis such as debris flows (Lifeng and Youshu, 2006). Nevertheless, the use of SVMs in geosciences is still minor.

1.2 Aim

The study presented here focuses on the development of an automated expert system for a systematic and efficient rock-mass classification that is able to deliver results synchronously to the excavation process and leads to enhanced safety and more cost-efficiency during hard rock tunnel excavations. To this end, a SVM was constructed and applied to all available data, which include either seismic data from the Faido Adit survey or seismic and tunnel-driving data from the Glendoe Tunnel survey. This work forms the basis for an expert system that can be integrated into a seismic-while-drilling system (e.g., ISIS) to realize a comprehensive method of seismic prediction.

1.3 Selection of a Self-Learning Algorithm

The development of a rock-mass classification system that incorporates seismic and tunnel-driving data to determine the rock-mass quality along a tunnel, synchronous with the excavation process, requires a high level of automation, both for data processing and interpretation. The latter part, the interpretation, can be carried out by computer-based self-learning algorithms. In this chapter the basic principles and ideas regarding different self-learning algorithms are pointed out.

Self-learning algorithms discover underlying patterns in data sets. For example, a rock, such as a granite, consists of defined percentages of quartz, feldspar and mica; however, granites from various outcrops can be quite different. The definition of a granite and the separation from other rock types is possible because a rule base has been established by mineralogists, who defined specific rock types based on their mineralogical content. These rules have been deduced from observations of mineralogical rock characteristics at many outcrops over many years. This process is simply the discovery of patterns that exist in a huge set of data. The recognition of certain patterns or principles that relate to the basic similarities of a group or class is called knowledge discovery (Fayyad et al., 1996). The process of recognizing underlying unknown probability distributions (patterns) in data by use of computer-based algorithms, is called pattern recognition. Only when the pattern that defines a group is known, the prediction of unknown cases become possible (Bishop, 2006; Nauck et al., 1994; Berthold and Hand, 2007). This is exactly the same process as that used by a geologist to recognize and identify a granite at a new outcrop where the geologist uses the underlying rules of mineralogically based rock identification. In the case of computer-based pattern recognition algorithms, a model is created where the rules are stored, after generalization of the rules is completed. Applying this model afterwards to new and unknown data sets allows the prediction of rock types, or in case of this study, rock-mass classes.

Data mining is the part of the knowledge discovery process where modeling, analyzing and discovery methods are applied. Because the user needs some theoretical considerations in order to decide on the best method to be used for a specific task and the planning and development of the consecutive processing steps the attribute "intelligent" often precedes the term data mining. Intelligent data mining is also closely related to machine learning. The two are generic terms for the development of algorithms for pattern recognition (Bishop, 2006); however, machine learning differs from data mining as machine learning is not necessarily concerned with finding *new* patterns in data. The terms are often used synonymously in literature though, as many of the algorithms can be used for both purposes.

The field of intelligent data mining includes methods like artificial neural networks (ANNs), support vector machines (SVMs), decision or regression tree analysis, Bayes-classifiers, probabilistic networks, neuro-fuzzy-systems, κ -nearest neighbor, hierarchical or probabilistic clustering and fuzzy logic, as well as classical statistics (Fayyad et al., 1996; Berthold and Hand, 2007). Several of these approaches were examined during this study to determine the algorithm that was most suitable for the given task of rock-mass classification from seismic wave velocities and tunnel-driving data. Below only SVMs, ANNs, and neuro-fuzzy systems are discussed; going into detail of all the aforementioned methods is beyond the scope of this work.

There is a large variety of applications of ANN and neuro-fuzzy system to geotechnical tasks (e.g., Alimoradi et al., 2008; Aminzadeh and de Groot, 2006; Cherkassky, 2006; Gokceoglu et al., 2004; Shirasagi et al., 2001; Shahin et al., 2009) and, more specifically, geoscientific questions in tunneling, such as the prediction of soil settlements (Shi et al., 1998; Nellessen, 2005), evaluation and interpretation of displacement monitoring (Großbauer, 2009), tunnel-boring machine performance (Bernardos and Kaliampakos, 2004) or geological/geotechnical risks determined from tunnel-driving data (Grima, 2000; Mitterlechner et al., 2007; Zettler et al., 1996) in comparison to the range in applications of SVMs that are discussed in Section 1.8.

The rock mass and its interaction with seismic and tunnel-driving data is highly complex (Sec. 1.6.1). It is obvious that, to capture such a complex system fully, a large data set is needed; however, the data sets available from this study are relatively small, such that it was necessary to select and use an algorithm for pattern-recognition that can best deal with small sample densities in the presented rock-mass classes. SVMs give better results for small training data sets, even though the performance of an ANN may approximate the SVM results, when the size of the data set increases (Vanajakshi and Rilett, 2004). Training data denominated the data samples that are presented to the algorithm for "training" or "learning", that is the discovery of unknown underlying patterns in data. After training and storage of the rules, the created model is usually "tested" on a test data set to validate the success of rule generalization. The test data set excludes data samples that have been used during training.

It is of major importance for the predictive performance of a self-learning algorithm that it generalizes well. If the used algorithm fits the training data strongly, a so-called over-fitting takes place. Conversely, if the algorithm creates a model too simple for the data, under-fitting occurs (Bishop, 2006). SVMs are very resistant to over-fitting, especially in regimes where other methods are affected by the "curse of dimensionality" (Schölkopf, 1997). The latter is the exponential increase in volume associated with adding extra dimensions to a (mathematical) space. Without going into too much detail, the generalization corresponds

to the optimum balance between over- and under-fitting of the model to the training data; however, local minima in the error function of the model occur and the generalization error is subsequently not a simple function. While the global minimum is the smallest value of the error function for any weight vector, other (local) minima correspond to higher values of the error function. The main advantage of SVMs over ANNs is that the learning process always converges to the global minimum, while the learning process of ANNs often stops in a local minimum. Even more disadvantageous for the usage of ANNs is that it is not possible to reconstruct if the learning process stops at some local minimum or else if the data set does not contain enough information to generalize underlying rules in the data sufficiently. The learning process of ANNs is often referred to as "black box" behavior because the intermediate steps that lead to the output of ANNs are not fully traceable by the user; however, there are approaches, especially in neuro-fuzzy modeling, that overcome this restriction (Nauck et al., 1994; Nauck and Kruse, 1997). Depending on the type of neuro-fuzzy system used, the comprehensibility of the result can be enhanced and the strongest draw-backs of fuzzy systems can be solved, which is that a comprehensive rule base needs to be defined by the user before application. Such a rule base is large and unmanageable for a highly complex problem setting, as is addressed in this study. Fuzzy systems have the advantage that they are able to deal well with neighboring classes, such as the neighboring rock-mass classes that define a rock mass to be either "excellent" or "very good" and have been applied in various cases in geoen지니어ing (Fairhurst and Lin, 1985; Demicco and Klir, 2004; Großauer, 2009; Klose, 2002; Zettler et al., 1996; Poisel et al., 1999a).

Another disadvantage of ANNs or neuro-fuzzy system is the lack of a theoretical background to determine the optimal network size and structure. The ANN structure has to be determined by trial and error so that the performance of an ANN or neuro-fuzzy system also strongly depends on the prior knowledge of the user regarding the ANN behavior. In comparison to the user-defined and often complex structures of ANNs or neuro-fuzzy systems, SVMs constitute a straight forward and mathematically fully described approach (cf. Sec. 1.8).

It is of great importance that a model once created can be updated during later applications, when new data has been collected and can be presented to the algorithm. For an ANN, the optimal network structure can change if the model is updated using new data sets. In this case a specialist is needed to determine the best network structure so that the ANN performance can reach its optimum. The work flow and model construction process for the SVM stays the same, no matter how many data sets are presented. Additionally, most data points from the first learning process can be disregarded for SVM training, as only those data points that define the class boundaries need to be stored. ANNs, on the other

hand, require all the presented data points every time they are trained, which may slow down the process over time.

SVMs were selected and used for the task of rock-mass classification in this study because of:

1. their straight forward nature,
2. the applicability to small data sets,
3. the security at which SVMs converge to the global optimum,
4. the robustness against overfitting and
5. the advantages during updating.

1.4 Geological Rock-Mass Properties

In order to apply the notion of knowledge discovery to the task of geotechnically describing the rock mass with seismic and tunnel-boring machine (TBM) parameters, it must first be determined which kind of output from the automated rock-mass classification system will shed most light on the rock-mass behavior. As single parameters, like, e.g., the uniaxial compressive strength σ_c , do not describe the rock-mass behavior fully, a variety of rock-mass classification systems has been developed heuristically during practical geotechnical applications in the past few decades. Singh and Goel (1999) give an overview on the most important classification systems that differ in the number and kind of rock-mass characteristics they incorporate. The classification systems selected for this study are the Rock Mass Rating (RMR) system and the Rock Quality Designation (RQD) index because for these classification schemes all necessary input parameters were continuously acquired at both test sites and both, RMR and RQD, belong to the best known and most widely applied rock-mass classification systems worldwide. By using the RMR and the RQD, this study also compares the automated classification results of the relatively simple RQD that is closely related to the frequency of discontinuities, and the more sophisticated RMR that incorporates a larger number of parameters.

In engineering geology, the rock mass must be visualized as an assemblage of intact rock blocks separated by different types and sets of discontinuities. Thus, the characteristics of the intact rock mass as well as the discontinuities must be considered. The term discontinuities is a generic term for all kinds of planar structures inside a rock mass. In this work, the subordinate term "joint" describes a discontinuity in the rock that is either of synsedimentary or tectonic origin but did not undergo lateral or vertical movement. Often, joints occur in so-called joint sets that are composed of several joints of the same spatial orientation and similar spacing. The discontinuities where lateral or vertical movement has taken place are denominated as faults. Other discontinuities are bedding planes in sediments, or schistosity planes in metamorphic rocks that develop because of parallel alignment of slaty minerals, e.g., mica. In literature, the term fractures is often used synonymously for either discontinuities or joints. Here, fracturing will refer to only anthropogenically induced rock breakage that may occur during laboratory testing or (tunnel) excavation.

For engineering purposes, the rock mass can never be fully described by only one parameter. It should be noted that the importance of the properties of the intact rock mass that determine rock-mass stability will generally be overshadowed by the discontinuity properties, though in rocks with wide discontinuity spacing, or in weak and altered rocks, the influence of the intact rock mass prevails (Bieniawski, 1989). The discontinuity network controls

(McCann et al., 1990):

1. the rock-mass deformability, strength and permeability, depending on the spacing of the discontinuities and their aperture and the degree of interconnection, etc.
2. the rock-mass anisotropy, depending on the geometry of the discontinuity sets.

Hence, all rock-mass properties are highly stress dependent because with higher stresses the discontinuities become narrower or closed and the influence of the discontinuity network on, e.g., the water content or the seismic velocities, decreases (cf. Sec. 1.6.1). A thorough discussion of field and laboratory test methods for the description of the intact rock mass and the discontinuity network can be found in the ISRM suggested methods (Ulusay and Hudson, 2007).

1.4.1 Calculation of RMR and RQD

The present study deals with data sets obtained from two different test sites in hard rock environments. For the classification of the single parameters, the Rock Mass Rating (RMR) system was used. The RMR, based on field studies, was first introduced by Bieniawski (1973) and has been enhanced several times since, most recently by Bieniawski (1989). Though this study uses the RMR classification system, other rock-mass classification systems like the Q-factor (Barton et al., 1974) could be integrated into the system as well. The RMR is calculated from the following geological/geotechnical parameters according to Bieniawski (1989):

- Uniaxial compressive strength σ_c ,
- Discontinuity spacing D_s ,
- Rock Quality Designation index (RQD),
- Condition of discontinuities C_d including:
 - roughness r ,
 - aperture e ,
 - infilling f ,
 - weathering W ,
 - persistence p ,
- Water inflow Q ,
- Correction factors for the purpose of engineering (tunneling) CF_{ep} and for the orientation of discontinuities CF_{od} with reference to the tunnel direction.

The classification is based on a rating of each single parameter. The range of one input parameter is assigned to a rating value (R_x), e.g., a rating value $R_{\sigma_c} = 15$ is assigned to a homogeneous unit of rock mass with an uniaxial compressive strength σ_c of $> 250\text{MPa}$. After assigning rating values to all parameters, the RMR is simply calculated by summing up the rating values R_x for each parameter for a specific rock mass unit:

$$RMR = R_{\sigma_c} + R_{RQD} + R_{J_s} + R_{C_d} + R_Q + R_{CF_{ep}} + R_{CF_{od}} \quad (1.4.1)$$

By assigning one rating value R_x to a range of neighboring values at a specific tunnel location, the geological conditions are obviously simplified but sufficiently well described for rock engineering purposes. Moreover, a variety of parameter combinations can lead to the same RMR class. A rock mass, e.g., with overall slightly smaller σ_c values but also a lower discontinuity frequency may lead to the same RMR class as a rock with higher σ_c values and higher discontinuity frequency.

The strength of the rock mass is included in most classification systems, including the RMR, by which the strength limit of the rock is considered. In both the Glendoe Tunnel and Faido Adit, σ_c was determined for each rock type. The test site at the Faido Adit, presented in Chapter 2, contains two different gneiss varieties with varying textures (e.g. augen-structure or lamination). The differences in texture leads to strong scattering in the σ_c values for each gneiss variety. The average σ_c values at a given location l were thus determined by calculating the harmonic mean of the measured σ_c values of each gneiss texture l ($l = 1, 2, \dots, n$) and its percentage of occurrence α_l at a given tunnel position (Klose, 2004):

$$\sigma_c = \frac{\sum_{l=1}^n \alpha_l \sigma_l}{\sum_{l=1}^n \alpha_l}. \quad (1.4.2)$$

In this way, the derived σ_c values of the gneiss varieties are only approximations. In the Faido case, the σ_c values differ strongly enough to distinguish between the two gneisses.

The degree of jointing, described by the total discontinuity spacing s_t , strongly influences the seismic velocities (Barton, 2007; Stacey, 1974 and 1976) and is an important parameter for rock stability as has been outlined above and discussed by Priest and Hudson (1976), Palmström (1982) and Priest (1993). Additionally, a steady increase in jointing along the tunnel profile may suggest an approaching fault zone. In a fault zone, the discontinuity frequency increases irregularly from the boundary in direction of the fault core. In general, the wider the fault core, the wider the disturbed zone will be (Giese et al., 2005). These brittle fault structures are critical for water transport within rock masses and hence for tunnel stability. The mean discontinuity spacing s_k of each discontinuity set $k = 1, \dots, l$ is determined along a given interval L along the profile and is used to calculate the total

Rating Value [%]	Quality Designation
90-100	Excellent
75-90	Good
50-75	Fair
25-50	Poor
<25	Very Poor

Table 1.1: Qualitative rating of the RQD into classes from rock mass regarded to be of “very poor” to “excellent” quality (Deere and Deere, 1988; Bieniawski, 1989).

discontinuity spacing s_t (Priest, 1993) as follows:

$$s_t = \frac{1}{\sum_{k=1}^l \frac{1}{s_k}}, \quad (1.4.3)$$

where $\frac{1}{s_k}$ is the mean frequency of a specific discontinuity set. Single discontinuities like, e.g., faults, are incorporated into the calculation by including additional discontinuity sets k_x with a spacing of $s_{k_x} = 1$. In this work the influence of the schistosity was not regarded because of the availability of data.

The RQD is the second most commonly used system in rock engineering and is often used as a fast and easy way to assess rock mass and drill-core quality. The RQD (cf. Sec. 1.4) does not fully describe the rock-mass quality (Barton, 2007) but provides a good estimate of the rock-mass behavior in heavily jointed rock masses, considering that it is a single parameter. Because the RQD and the seismic velocities are well known to show strong correlations (cf. Sec. 1.6.1), the RQD is used in this work as a single output parameter but is also included into the RMR calculation scheme. The RQD was first introduced by Deere et al. (1967).

$$RQD = \frac{\sum_{i=1}^n \bar{x}_{ti}}{L} 100\%, \quad (1.4.4)$$

where x_{ti} is the length of the i th piece of core that exceeds the threshold value $t \geq 0.1m$ and L is the length of the sampling line or considered interval. A summary of applications is given in Deere and Deere (1988). As no direct cores were available for the length of the test sites in this study, the RQD was determined indirectly. Priest and Hudson (1976) introduced the following equation for the theoretical RQD (TRQD):

$$TRQD = 100e^{-\lambda t} (1 + \lambda t), \quad (1.4.5)$$

where λ is the mean discontinuity frequency, linking the RQD to the total discontinuity spacing s_t and t is a threshold value (cf. Equation 1.4.4).

Apart from the overall rock strength and the mere presence or absence of discontinuities, another factor strongly affects the geotechnical rock-mass performance. As has been discussed above, joint conditions influence the rock-mass deformability, strength and permeability. Joint conditions are described by the parameters roughness r , aperture e , infilling (gouge) f , weathering W and persistence p .

The roughness r describes the nature of the asperities on the discontinuity surface and, depending on the aperture e , controls to which degree the opposite discontinuity surfaces can interlock. The interlocking has a great impact on potential shear movement and also defines the extent to which water can flow through the discontinuities. Using the classification scheme of Bieniawski (1989), five classes can be distinguished for the roughness (“very rough”, “rough”, “slightly rough”, “smooth” and “slickensided”) and also 5 classes for the aperture (“none”, < 0.1 mm, $0.1-1$ mm, $1-5$ mm and > 5 mm). The infilling f has a two-fold influence:

1. depending on its thickness, the infilling f prevents the interlocking of the discontinuity asperities described by the roughness r , and
2. the properties of the infilling (shear strength, permeability and deformational character) can differ strongly from those of the intact rock mass, e.g., shear movement in hard rock often occurs preferably on discontinuity planes with soft gouge infilling (Bieniawski, 1984).

Generally, during the field investigations the infilling was distinguished as either: “no infilling”, “hard infilling” or “soft infilling”.

At both investigation sites, the rock mass was freshly excavated and had not been exposed to weathering effects. The degree of weathering was therefore set to class “unweathered” throughout and will not be further discussed here.

Another parameter influencing the discontinuity condition is the persistence p of a discontinuity. A discontinuity set with high persistence p (i.e. with a trace length of hundreds of meters) affects the behavior of the rock mass more strongly than non-persistent discontinuity sets (i.e. on a scale of a meter to a few meters). Nonetheless, persistence was not sufficiently well recorded during the field studies and could not be regarded in this work.

In hard rock, the ground-water conditions are dominated by a discontinuity network; however, the parameter water inflow Q describes only the inflow into the tunnel, not the degree of saturation of the rock mass. Even if the water inflow is described as very low, the rock can be totally saturated a few meters into the rock from the tunnel surface (Marshall et al., 1999). Water inbreaks into tunnels can be caused, for example, by drilling through a water-bearing fault zone under pressure, which can lead to great risk for the safety

Rating Value	Quality Designation	Support
81-100	Very Good Rock	None
61-80	Good Rock	Locally
41-60	Fair Rock	Systematic, wide grid
21-40	Poor Rock	Systematic, close grid
<20	Very Poor Rock	Systematic, very close grid

Table 1.2: Rating of RMR classes and short description of the corresponding intensity of tunnel support.

of humans and the success of the whole project. The water inflow is categorized after Bieniawski (1989) as “dry”, “damp”, “wet”, “dripping” or “flowing”.

A structure (e.g., a fault zone) poses more danger to the tunnel if the structure is nearly parallel, or at a very shallow angle, to the tunnel axis. Structural reinforcement along the outface of the tunnel is very difficult to establish. The same holds true for structures that dip against the tunnel-driving direction. During tunneling, e.g., a clay bed that dips into the tunnel-driving direction may lead to the collapse of the head face because reinforcement cannot be applied fast enough to counteract the building-up pressure. Subsequently, the correction factors that account for:

- (a) the kind of underground construction to be built and
- (b) the direction of tunneling with respect to the main dip/dip direction of the discontinuities have been incorporated into the RMR (Bieniawski, 1973, 1984, 1989).

Hence, the RMR is not only dependent on geological characteristics but also on the engineering purpose - in contrast to the RQD.

For the RMR, only the “worst case” discontinuity conditions at a given location are taken into account. This is necessary, as different discontinuities can reveal different values or categories at the same location. For example, a discontinuity set d_A might have a rough surface, while the discontinuity set d_B has a slickensided surface at a given location l , which contains both d_A and d_B . In this case, the more unfavorable value “slickensided” is assigned to the given location l (Bieniawski, 1989; Barton et al., 1974). This also holds true for the correction factor of the discontinuity orientation. Although, the rock-mass condition is further simplified, the method is, nonetheless, justified for geotechnical applications, as rock-mass quality is not overestimated and construction safety is put to the fore. From a scientific point of view, this might be regarded as problematic, because the influence of some geotechnical parameters on the overall rock-mass behavior is determined based on empiricism only. At the same time, other parameters that do not fit into the constructed classification scheme are not taken into account. As an example for the RMR, e.g., the

block geometry might be mentioned here (Kulatilake et al., 2000, 2003). Nonetheless, the method has shown to be of high practical importance. As the aim of the presented study is to provide geoengineers with an easy to handle instruction model that can be integrated into the daily work flow, the use of the RMR is justified as much as the use of the RQD.

1.5 Tunnel-Driving Data

The use of tunnel-boring machines (TBM) for tunnel excavation has become the most common tunneling method in the past years, because TBMs allow for cost-effective tunnel constructions, especially in rocks with low stability and geologically and hydro-geologically difficult environments, such as those with shallow overburden, high water pressure, high permeability or low load-bearing capacity. During the tunneling process a huge variety of tunnel-driving parameters pertinent to the excavation process are continuously collected. Some of these machine parameters, such as the penetration rate, the thrust force and the cutter head torque, contain information on the interaction between the rock mass and the machine (Poisel et al., 1999b,a; Nellessen, 2005). Subsequently, the data has been used as a measure for the determination of rock-mass classes (e.g., Poisel et al., 1999a) or drilling classes with various geostatistical approaches (e.g., Aoki et al., 2007; Shirasagi et al., 2001; Fukui and Okubo, 2006). During the field work presented in this study, tunnel-driving parameters were only obtained during the Glendoe survey, as this tunnel was excavated by a TBM, whereas the Faido Adit was excavated by drill-and-blast method. The tunnel in Glendoe was excavated by an open gripper-TBM, as the lithology along this tunnel consisted of hard metamorphites. In such an open excavation, the rock mass is still directly accessible. Hence, a detailed mapping of the rock-mass characteristics that form the basis for the rock-mass classification using the RQD or RMR is available in the Glendoe Tunnel. The geological data acquisition becomes more difficult in so-called closed-mode excavations, where segmental lining covers the entire rock behind the shield area. Hence, the utilization of machine parameters for the assessment of the rock mass becomes even more important. The Glendoe Tunnel data set offers a direct comparison between high-resolution geological data and TBM parameters, which is a strong advantage of this data set. Further details on different types of TBMs and their respective fields of application are given by Wittke et al. (2007).

1.5.1 Operating Mode of an Open Gripper Tunnel-Boring Machine

In order to elucidate the understanding of the machine parameters and their interaction with the rock, a short introduction on the working principle of an open gripper-TBM is given. The cutter head is driven by hydraulic or electric motors and is mounted on the main beam (Fig. 1.1). To loosen the rock at the tunnel face, the cutter head is rotated and pressed against the rock by means of the thrust compactor. Thereby, the chisels that are situated on the cutter head pass over the tunnel face in concentric circles. A dynamic cycle develops in which the chisels first translate percussive –compressive and tensile– forces to

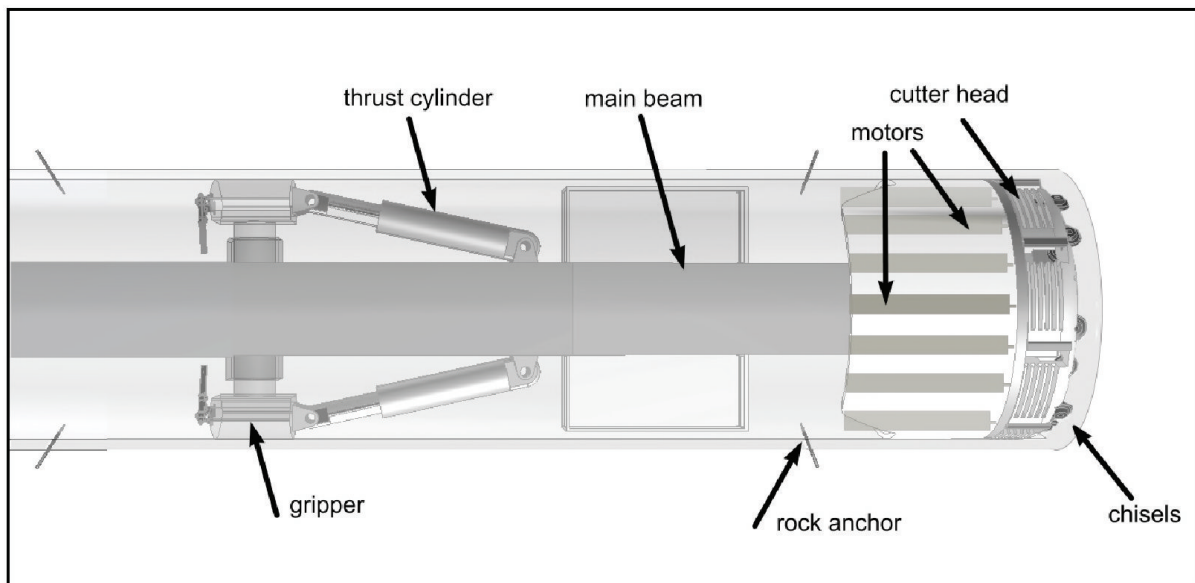


Figure 1.1: Schematic illustration of the main components on the open single-gripper tunnel-boring machine at the Glendoe construction site (top view, modified after pers. communication Well, 2010). The motors that are powering the thrust cylinders are situated right behind the cutter head. Those are connected to the grippers on both tunnel sides. The grippers act as an abutment so that the tunnel machine has enough footing to press the cutter head against the tunnel face .

the rock, followed by a phase in which shear forces dominate. During this dynamic cycle radial cracks occur and grow until small rock fragments are chipped off the rock (Thuro and Spaun, 1997). For achieving a sufficiently high contact pressure, the machine needs to be propped up against lateral bracing plates, the so-called grippers (Fig. 1.1). Those are pressed hydraulically sideways against the tunnel wall. This way, the machine is braced in the tunnel and has sufficient footing to serve as an abutment for the thrust force (Wittke et al., 2007). The thrust cylinders, which are located between the gripper unit and the cutter head, push the cutter head against the tunnel face while the machine is sliding on an invert shield or sliding shoe (Girmscheid, 2008; Wittke et al., 2007).

In the optimal case, the machine should be driven to its maximum electric capacity. To this end, the desired speed of forward progression (the advance speed) and the speed of the cutter-head rotation (the cutter-head speed) are estimated by the TBM-driver, who manually controls the advance speed. The advance speed depends on the move-out speed of the thrust compacter and is subsequently controlled by the thrust force. Apart from this, the cutter-head torque is altered by the machine operator in the way that the cutter-head speed stays constant at its predefined value. Thus, the values of the single thrust cylinders (thrust-force control) and the drivetrains (cutter-head torque control) are altered in the programmable logic controller, until the desired advance- and cutter-head

speeds are achieved (Girmscheid, 2008). This work flow also shows that the characteristics of driver operation influence the performance of the TBM.

The correlation of tunnel-driving parameters and geological conditions strongly depends on the technical layout of the TBM. This is because the maximum electric capacity of a TBM is determined by the technical potential of the machine and the prevailing geological boundary conditions, though economic considerations could also be an influencing factor (Schlicke et al., 2005).

Normally, all the relevant data produced during an excavation project are recorded and stored; however, the varying technical layout of the different types of TBMs, like shielded or open gripper machines, leads to differences in the amount and kind of parameters stored. As the TBM layout usually does not change during a single project, the main influencing factor for changes of the tunnel-driving parameters is linked to the rock-mass behavior, though results from one rock type to the next or from one project to the next should not be blindly transferred (Ribacchi and Fazio, 2005).

On most excavation sites, operations are electrically or electric-hydraulically controlled and the tunnel-driving data is collected automatically in this framework. Therefore, the acquired data can be processed digitally. The record interval varies between 0.1 to 1 Hz with an average of 200 to 400 different parameters, depending on the excavation type, thus allowing between 1.7 and 35 million data points, so called momentary values, to be collected in one day (Nellessen, 2005). Nevertheless, the resulting large data set is not automatically evaluated in a systematic way.

For the tunnel-driving data to be incorporated into the data base for a support vector machine or other pattern recognition systems, the huge amount of data requires a target-oriented limitation on the relevant parameters. Data mining methods (Bishop, 2006) could be carried out to filter significant parameters from the data set, though the results would need to be thoroughly reviewed. In the presented study, parameter selection was restricted to those that have a direct or indirect link to rock quality and have therefore been used in previous studies (e.g., Schlicke et al., 2005; Poisel et al., 1999b). Moreover, the same parameters are collected regularly at each construction site, so that the results can be generalized and used at other test sites.

1.6 Relationships between Rock Quality, Seismic Velocities and Tunnel-Driving Parameters

Many research projects have been conducted to shed light on the rock-mass behavior in terms of practical geotechnical applications. In this Chapter the focus lies on the rock-mass behavior of unweathered hard rock with low matrix porosity, according to the rocks encountered at both test sites.

1.6.1 Seismic Velocities and Rock-Mass Behavior

In most cases, a rock mass is a complex and highly heterogeneous body that cannot be fully described by only laboratory tests and local rock profiles. Information about a rock mass can be increased by using geophysical techniques, such as seismic profiling, that provide an indirect assessment of the engineering rock properties. Data collected during in-situ seismic measurements are noisy and non-linearly related to the complex system of geologic rock mass properties, leading to a highly complex interaction pattern between the single geologic and seismic parameters. A thorough analysis of the seismic compressional- and shear-wave velocities V_p and V_s from seismic refraction measurements for shallow depths on various unweathered and jointed igneous and metamorphic rocks (among others quartzites and gneisses) was done by Sjøgren et al. (1979) and Sjøgren (1984). Apart from inherent rock properties such as the mineral composition, V_p is mainly influenced by the following:

- stress,
- degree of jointing,
- presence of open discontinuities or discontinuities with infilling,
- ground water condition (Sjøgren et al., 1979; McCann et al., 1990).

According to McCann et al. (1990), the correlation between V_p and σ_c is non-linear and can be expressed approximately by a power function of the form $y = ax^b$ ($r = 0.88$). However, broad scatter in the results for individual rock types, especially for rocks with low rock strength, have been observed. Although McCann et al. (1990) showed that precise uniaxial compressive strength σ_c values cannot be predicted from V_p , rock types may be classified qualitatively (e.g., weak to very weak or strong to very strong rock).

The RQD index was introduced as a measure for the length of intact rock pieces in a core (Eq. 1.4.4), meaning that the RQD value decreases with increasing degree of jointing. Hence, V_p not only decreases with an increasing degree of jointing (Sjøgren et al., 1979;

Sjøgren, 1984) but, consequently, also with decreasing RMR or RQD values. Following an equation set up by Deere et al. (1967), V_p is correlated with the RQD factor by:

$$\left(\frac{V_{pF}}{V_{pL}}\right)^2 \approx RQD, \quad (1.6.1)$$

where V_{pF} is influenced by natural jointing, and V_{pL} is the sonic velocity in the intact rock mass. Both velocities are measured in the same frequency band; however, no specification on the exact frequency range or sampling method is mentioned (Deere et al., 1967). Moreover, the fracture network is not the only factor influencing V_{pF} (e.g. water saturation of the rock) so that the relationship in Equation 1.6.1 can only be an approximation (Deere et al., 1967). Drawing relationships between laboratory and field measurements should also be done with care, as there are several other factors that influence the resulting values of V_{pL} (Rummel and van Heerden, 1978), such as:

- laboratory test method,
- dimension and geometry of the specimen,
- recovery process of the specimen (e.g. blasting, drilling),
- sample preparation,
- applied stress field during testing. A low stress field leads to the opening of micro structures that reduce the measured velocities.

Sjøgren et al. (1979) stated that the influence of the jointing of the rock mass on V_p decreases with overall decreasing V_p , which implies weaker correlations for sedimentary or highly weathered rock; however the discontinuity frequency and consequently the RQD can be predicted based on seismic measurements. Unusually high matrix-porosity or weathering in metamorphic rocks with constant discontinuity frequency will cause a decrease in seismic velocity (Sjøgren, 1984).

The non-linear relationship between increasing depth or horizontal stress and the closure of open discontinuities leads to increased seismic velocities at depth (Bandis et al., 1983) and is thus often called "acoustic closure". Therefore, both V_p and V_s values in a rock with several discontinuity sets are likely to show stress sensitivity with greater depth or stress level (Barton, 2007; Sjøgren et al., 1979; Stacey, 1976). Thus, V_p increases with a simultaneous increase in hardness, RQD and density (Miranda and Mello-Mendes, 1983).

In accordance with these findings, Tanimoto and Ikeda (1983) state that below stress levels of 3 MPa, V_p drops rapidly, but that it is approximately proportional to the normal stress applied to simulated fractures over a range of 3 MPa to 20 MPa. In contrast, (Stacey, 1976) argued that the influence of jointing disappears for stresses > 2 MPa - stresses

exerted on low overburdens and dry rock conditions. Also the influence of jointing on V_p under wet conditions and with clay infilling was negligible in the lab results of this study. However, Stacey (1976) carried out ultrasonic laboratory tests only on marble specimen of 0,46 m lengths and 5 cm square cross-sections with artificially induced jointing. Tanimoto and Ikeda (1983) on the other hand used various hard rocks of variously sized specimen for their laboratory testings. Seismic waves of constantly 400 Hz were generated by piezoelectric transducers that were placed perpendicular to the artificially induced jointing on both sides of the specimen.

The discontinuity conditions (aperture e , roughness r , and infilling f) influence the normal stiffness of discontinuities and, subsequently, the acoustic closure non-linearly (Bandis et al., 1983); however, the degree to which the infilling of discontinuities and their water content influence the closure depends strongly on the aperture width (Stacey, 1976). Tanimoto and Ikeda (1983) found that the discontinuity frequency [$\frac{fractures}{m}$] has no influence on V_p for apertures below $\sim 40 \mu m$, whereas large apertures create large changes in V_p . High roughness of the discontinuity surface lessens the influence of present jointing on the seismic velocities, as the opposing discontinuity surfaces interlock even at higher apertures. Results from ultrasonic measurements (Stacey, 1976) showed that at low stresses this effect takes place even for discontinuity apertures of less than $10 \mu m$; however, it should be taken into account that the acoustic coupling in nature is not as complete as in laboratory tests due to different orientations of discontinuities, mineral coatings and infillings, weathering, and near-surface stresses (Barton, 2007). Won and Raper (1997) found that V_s is influenced by the opening of microcracking. The same effect also lead to an increase in the $\frac{V_p}{V_s}$ ratio in their study. A high sensitivity of V_s to gouge thickness has been shown by Fratta and Santamarina (2002). V_s decreases and the damping ratio increases with increasing gouge thickness. When the joints are filled with clay, the S-wave propagation is especially slowed down. On the other hand V_s increases and the damping ratio decreases with an increase in normal stress. (Stacey, 1976) concluded that the shear-wave parameters are generally more sensitive to rock mass quality than V_p .

The water content of a rock is dependent on its porosity and permeability; the discontinuity network within a rock is the main pathway for the water flow in low porosity hard-rock environments. V_p decreases more strongly than V_s with decreasing water saturation. (Giese et al., 2005) states that this effect is caused by the higher impact of the water saturation on the bulk modulus k with respect to the shear modulus μ . V_p reacts faster to changes in the water saturation as the bulk modulus k is affected by the water saturation. Thus, V_s is assumed to be a better indicator of changes in the lithology or the discontinuity density as it is transmitted solely over the matrix and subsequently does not reflect changes in the pore fluids or gases.

McCann et al. (1990) pointed out that the dynamic moduli can be derived from V_p and V_s by empirical derivations but that the indirect assessment of the rock condition is where seismic measurements make their strongest contribution. In the previous sections, the relationships between the seismic velocities and geological features have been discussed. Furthermore, the calculation of the RMR factor from the discontinuity attributes and more general factors such as the uniaxial compressive strength σ_c or the general dip direction with respect to the tunnel direction has been shown in Section 1.4. El-Naqa (1996) stated that it is more useful to correlate the seismic velocity to a geomechanical classification system, e.g., the RMR, as such a system considers several features that affect the geomechanical behavior of the rock mass, such as the discontinuity characteristics and frequency. Some correlations done by Sjøgren et al. (1979) and El-Naqa (1996) are listed in Table 1.2. Attempts to correlate the seismic velocities to rock-mass quality, expressed in rock-mass classes, have been done by, e.g., Barton (2007) for the Q-system. Various attempts to correlate the RMR classes with the Q-system have been summarized in Goel et al. (1996).

Very Poor Poor Fair Good Excell											Diagnostic Description
0	10	20	30	40	50	60	70	80	90	100	RQD
		~20		~14		10.2	6.7	4.4	3.4		Discontinuities per meter
		~5		~7		~10	~15	~23	~29		Mean Core Length [cm]
		30	35	40	45	50	55				V_p , x100 [m/s]
		18	22.7	30.3	39.7	51.3	63.5				E_{dyn} [GPa]
		17.8	22.2	27.1	33.7	41.2	50.7				k [GPa]
		6.5	8.7	11.5	15.2	19.8	24.7				μ [GPa]
0	20	40	60	80	100						RMR

Figure 1.2: Mean values of physical and dynamic properties of hard, unweathered igneous and metamorphic rocks deduced from shallow refraction seismic measurements. E_{dyn} is the dynamic elastic rock-mass modulus, k is the bulk modulus and μ the shear modulus. A rough correlation of RMR, discontinuity frequency and RQD with seismic velocities and dynamic rock-mass moduli is possible; however, the influence of increasing overburden must be considered. The compilation is based on results from Sjøgren et al. (1979) and El-Naqa (1996).

McCann et al. (1990) discussed the results from a geological and geotechnical survey carried out in phyllitic rocks from the Dalradian Supergroup, which were also excavated in the power tunnel of the Glendoe Hydro Electric Power Plan but do not crop out in the surveyed area (Fig. 2.4). A rock-mass assessment based on the RMR classes was done, although important factors such as potential water inflow or the orientation of structures with respect to the tunnel alignment were not collected (McCann et al., 1990). The results showed that, on the basis of a correlation between RMR values and seismic velocity-measurements, an extrapolation of the rock quality between several boreholes was feasible.

The only significant anomaly in the study of McCann et al. (1990) resulted from the presence of weak phyllites. For these rocks, the σ_c values were strongly reduced, which led to a low RMR class and low seismic velocities in spite of high RQD values. El-Naqa (1996) observed strong correlations between seismic velocities and RMR or RQD for rock mass classes better than "poor", but strong variations were also found in the classification results for RMR and RQD if extremely weak shales and marly limestones were present. El-Naqa (1996) interpreted the reduced rock-mass class to be caused by an increased discontinuity frequency resulting from the impact of the drilling process on the weak rocks.

Two equations describing the reciprocal behavior between seismic velocities, Young's modulus E_{dyn} and the RQD and RMR have been established by El-Naqa (1996). V_p , the in-situ bulk density ρ_b and the Poisson's ratio ν were used to calculate the Young's modulus E_{dyn} , as described by McDowell (1990):

$$E_{dyn} = V_p^2 \times \rho_b \left[\frac{(1 + \nu)(1 - 2\nu)}{(1 - \nu)} \right]. \quad (1.6.2)$$

The Poisson's ratio ν can be calculated from V_p and V_s using the following equation:

$$\nu = \frac{\left(\frac{1}{2}V_p^2 - V_s^2\right)}{\left(V_p^2 - V_s^2\right)} \quad (1.6.3)$$

Then, the RMR and RQD values were correlated with the Young's modulus E_{dyn} using the following best-fit relationships:

$$E_{dyn}(GPa) = 0.00039 \times RQD^{2.54} \quad (R = 0.78). \quad (1.6.4)$$

$$E_{dyn}(GPa) = 2.3 RMR - 109.0 \quad (R = 0.87), \quad (1.6.5)$$

From Table 1.2 and the Equations 1.6.2 to 1.6.4, it becomes clear that the RMR rating system and the RQD are related to the dynamic Young's modulus of the rock mass and thus also to the seismic velocities.

1.6.2 Tunnel-Driving Parameters and Rock-Mass Behavior

Several studies have been performed to determine the relationship between parameters obtained from the TBM advance and the rock-mass behavior. According to (Sapigni et al., 2002; Poisel et al., 1999b), the best performance of a TBM is recorded in fair to good rock (40-70 RMR), though more geomechanical problems in TBM excavations may arise for very low or very high rock strength (Ribacchi and Fazio, 2005). The rock strength is not equal to the rock-mass quality but is an important factor for the estimation of the latter, expressed in RMR values (very good rock quality > 80 RMR, cf. Tab. 1.2). In rocks with high strength and wide discontinuity spacing, adequate penetration rates cannot be achieved (Ribacchi and Fazio, 2005). Sapigni et al. (2002) describes reduced advance rates for high rock quality to be a consequence of reduced capability of cutter indentation and chips formation. With a simultaneous increase in hardness, RQD, density and V_p increases, while the drilling rate decreases strongly (Miranda and Mello-Mendes, 1983). Even though low V_p may indicate lower rock mass quality, correlations should be treated with care because of the influence of, e.g., horizontal stress or depth as described in Section 1.6.1.

For very low rock strength, the performance of the TBM is reduced by poor stability at the head face behind the shield (Ribacchi and Fazio, 2005). The thrust force is decreased to avoid interlocking of the cutter head for low rock mass quality (< 30 RMR), for example, rocks that are categorized as "soft" to "very soft", such as schists and phyllites. Because of the thrust reduction the performance decreases (Sapigni et al., 2002). Though Poisel et al. (1999b) describes that low contact pressure caused low torque values for the Vereina Tunnel, he also states that experienced tunnel-boring machine operator reported that on very soft rock with low contact pressure, high torque values are caused by the elasticity of the rock and the depth of penetration. The interaction patterns of rock-mass behavior and technical parameters are thus not linear and partly ambiguous and still a field of ongoing research.

1.7 Seismic Systems in Tunneling

In general, the seismic systems available for commercial use in tunneling generate seismic body waves (compressional (P-) and/or shear (S-) waves) near the tunnel wall or directly at the tunnel face. Typical sources are explosive charges in bore holes around the tunnel perimeter (Dickmann, 2008), vibrators integrated in the TBM cutter head (Kneib et al., 2000; Bruns et al., 2008), or noise from the rotating cutter head of the TBM itself (Petronio and Poletto, 2002; Brückel et al., 2008). The waves are reflected or backscattered by heterogeneities in the rock mass and the reflections are observed by seismic receivers, also called receivers, placed around the tunnel or at the tunnel face. The receivers can be integrated into the TBM cutter head (Kneib et al., 2000) or the tips of rock anchors (Lüth et al., 2008a), where they can detect the full seismic wave field. The spatial distribution of heterogeneities is then examined by e.g. True Reflection Tomography (Otto et al., 2002) or migration (Kneib et al., 2000; Dickmann, 2008). In general, the uniqueness and reliability of the solution depends on multiple coverage of subsurface points and the degree of subsurface illumination that is achieved by using large apertures. Unfortunately, neither of these two prerequisites is available in typical tunnel construction sites, where the source and receiver spread is restricted to the one-dimensional shape of the excavated structure and the number of boreholes for the receivers is limited. Furthermore, the current seismic systems suitable for underground use are normally restricted to either hard or soft rock.

In order to overcome these limitations, the Integrated Seismic Imaging System (ISIS) has been developed (Borm et al., 2003). ISIS shows a modular hardware design including different seismic sources and anchorings for the receivers. Moreover, the system does not use explosives so that the measurements have got a very low impact on the tunnel surroundings. Thus, the system can be used with a large variety of tunnel construction and support methods (Rechlin et al., 2009) and measure continuously during the entire constructional phase. The ISIS hardware components are currently being implemented for routine applications during the excavation (Lüth et al., 2008a,b; Giese et al., 2005, 2006). Further research is focused on modeling and processing of data acquired under such conditions, as well as on their integrative interpretation and new hardware development (Lüth et al., 2009). ISIS was used for the data acquisition of this study.

The Integrated Seismic Imaging System (ISIS)

ISIS includes a non-intrusive seismic acquisition system as well as processing and imaging tools installed several meters behind the tunnel face and thus does not interfere with the tunnel construction work. The system may be used for the exploration of the tunnel

near field (Klose et al., 2007; Giese et al., 2006; Borm et al., 2003) or for the detection of geological structures ahead of the tunnel face with distances up to 200 m (Rechlin et al., 2009; Lüth et al., 2008c). ISIS consists of four components:

- **Sources:** The seismic sources used during the field studies presented are pneumatic impact hammers (Borm et al., 2003 and 2000). In order to generate an impact, the 5 kg moving mass of a pneumatic cylinder is accelerated onto a shock plate driven by compressed air. Prior to the impact, the hammer is prestressed towards the rock with a force equivalent of 200 kg. The prestress guarantees an optimum coupling between the hammer and the rock. A programmable steering unit controls the impacts with a maximum trigger error of < 0.1 ms and a repetition rate of 5 s. The resulting impulse signals, with frequencies up to 2 kHz and a center frequency of about 800 Hz allow for an exploration range of up to 200 m in hard rock surroundings. In order to accommodate a range of conditions, the pneumatic hammers can be integrated into tunnel boring machines or be operated independently.
- **Receivers:** The full seismic wave field is recorded by 3-component receivers which are mounted on the tunnel walls, and vary in position according to the excavation type. In an open excavation process, the receivers are installed at the tip of reinforced polymer rock anchors, mounted in three orthogonal directions. The anchors are cemented in bore holes in the tunnel walls with two-component epoxy glue, which strongly binds the receivers to the surrounding rock and thus ensures high acoustic coupling (Borm et al., 2003). In tunnels constructed with segmental lining, the receivers are screwed into pre-existing threads in the segments (Rechlin et al., 2009). When properly orientated, the receiver rods form a radial or axial receivers array close to the tunnel face. The full seismic wave field with signals up to 3 kHz are recorded. Laboratory studies show a statistical error in the amplitude response of the receivers of $< 5\%$.
- **Data acquisition system:** The data acquisition unit used during the seismic surveys in the Faido Adit and the Glendoe Tunnel was the "SUMMIT Compact" by Deutsche Montan Technologie GmbH (DMT).
- **Software:** The software of ISIS includes modules for data acquisition, processing and imaging in 3D as well as imaging of geological and geotechnical features (Giese and Lüth, 2008). (Bohlen et al., 2007) developed the model of Rayleigh-to-shear wave conversion at the tunnel face. By using this model a high-resolution exploration ahead of the tunnel face became possible.

The seismic surveys in the Faido Adit and the Glendoe Tunnel were both carried out using the seismic acquisition and interpretation tools of ISIS. Due to the different excavation

modi, the measurement geometry has been adapted to the conditions on the respective tunnel construction sites as outlined in Section 2.2.

1.8 Basic Concept of Support Vector Machines

One promising methods of pattern recognition for the application to real and complex data sets are the support vector machines (SVMs). SVMs are part of the kernel methods and are based on the statistical learning theory (Vapnik, 1998). Details on the statistical learning theory and the general concept of support vector machines (SVMs) are given in Schölkopf (1997) and Burges (1998). SVMs map data non-linearly to a high-dimensional feature space. In this feature space a linear decision surface is constructed that separates the data into classes. To construct the decision surface, a margin along the decision surface is introduced and maximized between the classes in question. The intuitive idea behind this approach is that a decision surface with a large margin is more resistant to noise and that by maximizing the margin the solution becomes unique, ensuring high generalization ability of the learning machine (Bishop, 2006).

In this chapter the construction of a SVM for multi-class classification is reviewed step-by-step. First, the simplest classification problem is regarded where two classes are separable by a linear decision surface (linear separator) with no misclassification. As real data are rarely linearly separable, the approach will be generalized to linear classifiers that allow for training errors (soft margin classifiers) (Cortes and Vapnik, 1995). The last step is the introduction of the kernel trick to avoid the soft margin classifier and realize a nonlinear classifier, which is called support vector machine. Based on the principles outlined in this chapter, a SVM for the specific task of rock-mass classification based on seismic and tunnel-driving data is developed in Chapter 4.

Linear Classifiers

The SVM is a supervised learning technique that was originally developed for solving binary classification problems (with classes 1 and -1). The simplest case of classification is the linearly separable case without misclassification. The aim is to find the optimal decision surface that acts as the linear decision function with a maximum distance (margin) to the nearest example vectors of the respective classes. In 2D the optimal decision surface is a straight line, in 3D it is a plane, and in higher dimensions it is a hyperplane. The training data set (X) , of vectors x and labels y are members of the feature space \mathbb{R}^N of the corresponding classification:

$$(X) = (y_1, x_1), \dots, (y_l, x_l), \quad y_i \in \{-1, 1\}. \quad (1.8.1)$$

The aim is to partition the feature space \mathbb{R}^N so that the classes are optimally separated. The

label vector y contains the information as to which class an observational point is assigned, while the vector x_i of observation i is the sum of all measured feature characteristics at this point and is called a feature vector. All feature vectors x_i in a training data set (X) build the feature matrix. In the area of application discussed here, an observational point would be any point along the surveyed tunnel section. At each observational point the geological characteristics are determined and the RMR and RQD are calculated (cf. Sec.1.4). Either the RMR or the RQD shall be predicted and thus constitute the output vector or label vector y . The single RQD or RMR values are thus denominated labels. A feature is then a single parameter, e.g. the P-wave velocity, at a specific tunnel location. The values of all seismic and machine parameters at a specific tunnel location constitute the feature vector x_i . Subsequently, the feature matrix includes the whole data set of seismic velocities and the tunnel-driving parameters along the entire survey (cf. Fig. 4.2).

There are many possible decision surfaces separating the data (Fig. 1.3 a) but only one that optimally separates the training points by keeping the maximal distance (maximum margin) possible to all training points (Fig. 1.3 b). This unique decision surface, also called the optimal hyperplane, is defined as:

$$H = \{x | \vec{w} \cdot \vec{x}_i + b = 0\}, \quad (1.8.2)$$

where w is the normal vector on the decision surface and b is the offset. In the simple linearly separable case, there are no data points lying inside the margin. However, data points that theoretically lie on the hyperplane satisfy:

$$\vec{w} \cdot \vec{x}_i + b = 0. \quad (1.8.3)$$

To find the optimal separating decision surface (or hyperplane in the usual case), it is assumed that there exist training points (x_i, y_i) for which the following constraints hold true:

$$\vec{w} \cdot \vec{x}_i + b \geq +1, \text{ if } y_i = +1 \text{ and} \quad (1.8.4)$$

$$\vec{w} \cdot \vec{x}_i + b \leq -1, \text{ if } y_i = -1. \quad (1.8.5)$$

The feature vectors (data points) that satisfy these constraints are closest to the class boundaries and are called support vectors, as the removal of one of these data points would influence the orientation in space of the optimal hyperplane.

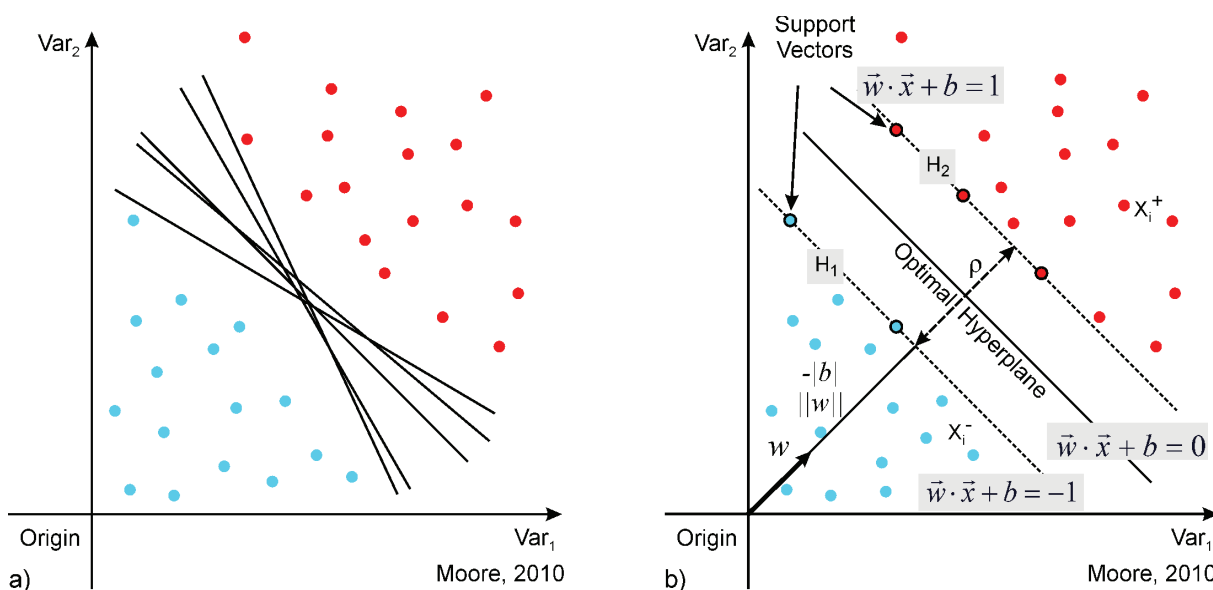


Figure 1.3: By calculating the margin between the samples of two classes in a 2D decision space that exhibits maximal distance to both of these classes, the position of the optimally separating decision surface is determined. The optimal separating hyperplane is the one that separates the data with the maximal margin possible. (a) There are many decision surfaces that are separating the Classes blue and red (source: Moore, <http://www.cs.cmu.edu/afs/cs/Web/People/awm/tutorials/svm15.pdf>). (b) By using the training examples closest to the opposing class, the class boundaries are found (source: merged Figure based on Kanevski et al., 2009 and Burges, 1998). The maximal distance between the classes (maximal margin) and the optimal separating hyperplane can then be identified because the maximal margin ρ is defined as the shortest distance from the decision surface to the closest positive or negative training points. Those training points are called support vectors.

As seen in Figure 1.3, a hyperplane H_1 can be visualized that runs through all feature vectors satisfying Equation 1.8.4 and a hyperplane H_2 for all points satisfying Equation 1.8.5. In Figure 1.3 b these hyperplanes correspond to the dashed lines. From the Equations 1.8.3, 1.8.4 and 1.8.5 it follows that the optimal hyperplane is scaled with respect to the support vectors.

Note that H_1 and H_2 are parallel to each other as they have the same normal vector so that the maximal margin ρ is defined as the shortest distance between H_1 and H_2 at each point along the surfaces. The two equalities in the Equations 1.8.4 and 1.8.5 can be combined into one set of inequalities:

$$y_i(\vec{w} \cdot \vec{x}_i + b) - 1 \geq 0 \forall i. \quad (1.8.6)$$

Finding the optimal hyperplane is an optimization problem. To solve this optimization problem the length of w is minimized so that the maximal margin ρ is maximized, while

respecting the constraints in Equation 1.8.6. If $\|w\|$ were 1, then the left hand side of Equation 1.8.6 would equal the distance of x_i to the hyperplane. Thus, w has to be divided by $\|w\|$ to transform w into the distance. Considering two points x_1 and x_2 , with x_1 satisfying Equation 1.8.4 and x_2 satisfying Equation 1.8.5 and projecting them onto the hyperplane normal vector $\frac{w}{\|w\|}$, the margin that is measured perpendicularly to the hyperplane, equals $\frac{2}{\|w\|}$ (Schölkopf and Smola, 2002).

Soft Margin Classifiers

The optimization problem of finding the optimal hyperplane can be solved in the Lagrangian formulation. In this form, the handling of the optimization problem is simplified as the training data will only appear in the form of dot products between vectors. This allows for the generalization of the procedure in the non-linear case. Lagrange multipliers α_i , ($i = 1, \dots, l$) are introduced for each of the inequality constraints. The Lagrangian L_P has to be minimized with respect to w and b and maximized with respect to α_i :

$$L_P = \frac{1}{2} \|w\|^2 - \sum_{i=1}^L \alpha_i y_i (\vec{w} \cdot \vec{x}_i + b) + \sum_{i=1}^L \alpha_i \quad (1.8.7)$$

subject to:

$$\alpha_i \geq 0, \quad i = 1, \dots, L.$$

Equation 1.8.7 describes a convex quadratic programming problem, since the objective function is itself convex, and those points satisfying the constraints also form a convex set. The dual formulation L_D of the problem is obtained after minimizing w and b and maximizing α_i . The values are inserted into $L(w, b, a)$ and the latter is converted to:

$$L_D = \sum_{i=1}^L \alpha_i - \frac{1}{2} \sum_{i=1}^L \sum_{j=1}^L \alpha_i \alpha_j y_i y_j x_i \cdot x_j, \quad (1.8.8)$$

subject to:

$$a_i \geq 0 \text{ and } \sum_{i=1}^L \alpha_i y_i = 0. \quad (1.8.9)$$

By solving the dual problem, the values of a_i , that maximize L_D are attained, and the normal vector can be calculated with $w = \sum_{i=1}^L \alpha_i y_i x_i$, where the decision surface with maximum margin follows from the latter. The decision function for the decision surface

thus is:

$$f(x) = \sum_{i=1}^L y_i a_i x_i \cdot x + b. \quad (1.8.10)$$

From the above Equations it follows that if $\alpha_i = 0$, then $y_i(\vec{w} \cdot \vec{x}_i + b) \geq 1$, and for $\alpha_i > 0$, the equality holds: $y_i(\vec{w} \cdot \vec{x}_i + b) = 1$. The support vectors subsequently correspond to $\alpha_i > 0$ and satisfy $f(x, \{w, b\}) = +1$.

As in nature the data is usually not separable without errors. The techniques developed need to be extended for non-separable data sets by introducing so called slack variables $\xi_i \geq 0$ to the constraints (Cortes and Vapnik, 1995). To solve a linear but non-separable classification problem, errors are admitted (Fig. 1.4).

The boundary conditions in the Equations 1.8.5 and 1.8.4 need then to be adjusted:

$$\begin{aligned} \vec{w} \cdot \vec{x}_i + b &\geq +1 - \xi_i \text{ for } y_i = +1 \text{ or} \\ \vec{w} \cdot \vec{x}_i + b &\leq -1 - \xi_i \text{ for } y_i = -1, \end{aligned} \quad (1.8.11)$$

subject to the constraint:

$$\xi_i \geq 0 \forall_i.$$

The overall sum of slack variables ξ_i limits the amount of training error and is integrated into the optimization problem by the penalty parameter $C > 0$. The parameter C regulates the impact of the training errors on the Equation 1.8.11. With increasing values of C , the tolerance against training errors decreases and the margin around the separating hyperplane also decreases. Thus, by changing the parameter C , the margin can be changed and the tolerance to error can thus either be increased or decreased. Such a classifier is called a soft margin classifier.

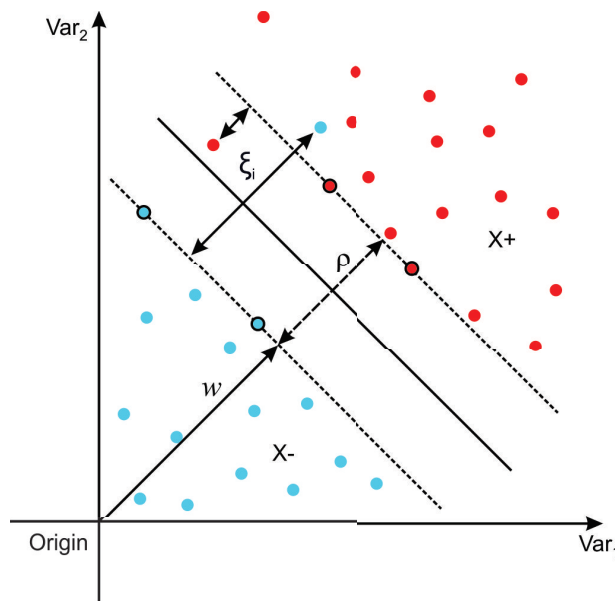


Figure 1.4: The introduction of slack variables ξ_i allows training points to lie inside the margin or even on the wrong side of the decision hyperplane, as data is often noisy and contains outliers (source: Kanevski et al., 2009). The number of such cases can be regulated by the penalty parameter C .

From Soft Margin Classifiers to Support Vector Machines: The Kernel-Trick

The aim of a SVM is to map the training data into a higher-dimensional feature space by using a mapping function Φ . In the feature space a separating hyperplane with a maximal margin ρ can be constructed, using a kernel function that needs to fulfill the Mercer theorem (Vapnik, 1998). In the input space, the separating hyperplane and margin would correspond to a nonlinear decision function (Fig. 1.5). This procedure is called the kernel-trick and is applicable because the Lagrangian formulation has been previously introduced so that the training data appears only in the form of dot products in Equations 1.8.8 to 1.8.10.

Given a kernel function K , with:

$$K(x, y) = \langle \phi(x), \phi(y) \rangle, \tag{1.8.12}$$

only the kernel function is needed in the training algorithm and the mapping function Φ does not need to be known explicitly. The procedure saves computing time, especially in very high-dimensional feature spaces. Still, all considerations of the previous sections hold true as the separation is still done linearly but in a different space. For every function

$K(x, x')$ that satisfies the theorem there exists a feature space where the function acts as a dot product. This way the following decision function for an optimal hyperplane for non-linear classification problems ensures as follows:

$$f(x) = \text{sign}\left(\sum_{i=1}^{L_s} a_i y_i K(s_i, x) + b\right), \quad (1.8.13)$$

with s_i being the support vectors. The advantage of using the kernel trick is that only the kernel function, rather than the scalar product, needs to be calculated. The most widely used kernel functions are the polynomial and the Gaussian radial basis function (RBF) (Vapnik, 1998). The kernelized version of a soft margin classifier is called a support vector machine (SVM).

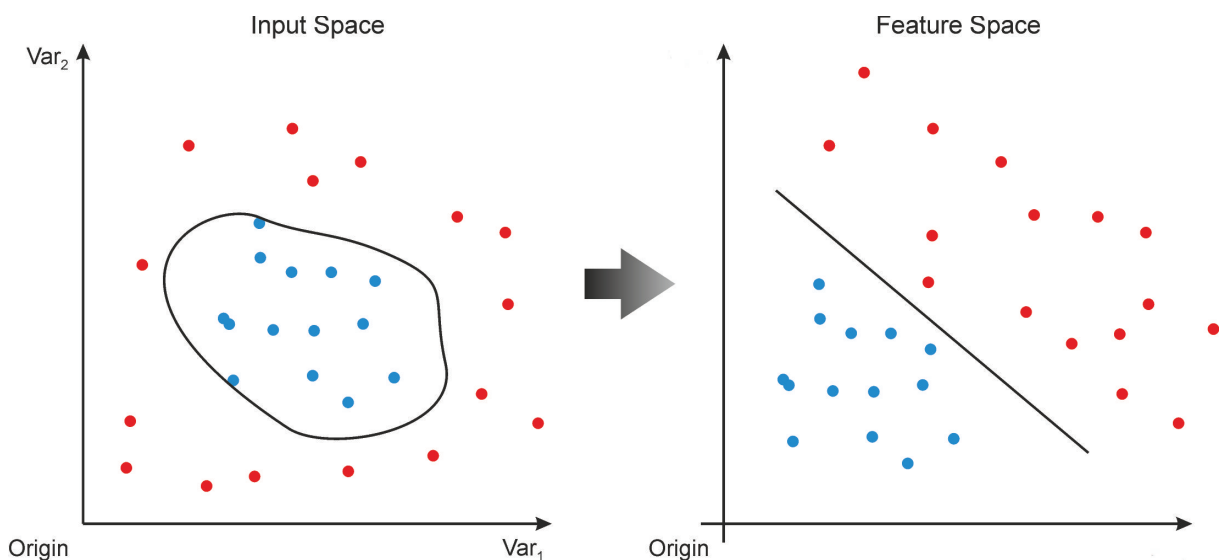


Figure 1.5: The training data is mapped into a higher-dimensional feature space by using a mapping function Φ (source: Schölkopf and Smola, 2002). In this feature space, a separating hyperplane with a maximal margin ρ can be constructed. The class separation would necessitate a nonlinear decision boundary in the input space (left hand side) but in the higher dimension, the data are separated by a linear hyperplane (right hand side).

Applications of SVMs

SVMs play an important role in machine learning since they are one of the few theoretically well-founded methods that show promising performance on real-life data (Schölkopf and Smola, 2002). The field of applications for SVMs includes various implementations in bioinformatics (Mohr et al., 2008), text processing (Joachims, 1998), image processing applied to rock-fracture tracing (Wang and Liao, 2007), time series analysis (Rüping, 2001) and environmental applications (Kanevski et al., 2009; Welle, 2009) or remote sensing (Ge

et al., 2008), while Vanajakshi and Rilett (2004) compared the performance of artificial neural networks and SVMs for the prediction of traffic speed. In the field of geoenvironment, SVMs have been applied to, e.g., assessing debris flow hazard (Lifeng and Youshu, 2006) and landslide susceptibility mapping (Yao et al., 2008).

2 Field Investigations

Two different data sets, created from surveys taken at hard rock tunnel sites, are employed as a base for the development of an automated rock-mass classification. The first survey took place in the Faido Adit, which is part of the Multifunctional Station Faido (MFS) of the Gotthard Base Tunnel (GBT) in southern Switzerland (Amberg, 2006). Both the Leventina gneiss and the Lucomagno gneiss, which both belong to the Penninic Gneiss Zone, are exposed in the adit. The second data set was acquired in metamorphic quartz schists and quartz-mica schists during the construction work for the Glendoe Hydro Electric Power Plant in Scotland.

In this chapter, the general geological settings of both surveys are presented. The techniques that were applied for acquiring geological data are discussed and the geological data along the Faido Adit and the Glendoe Tunnel surveys are described. Then, the set-up for the seismic data acquisition is highlighted, and the data from the seismic surveys are presented for the Faido Adit and Glendoe Tunnel surveys. The chapter concludes with the description of the tunnel-driving parameters acquisition for the Glendoe Tunnel survey.

2.1 Geological Setting

2.1.1 The Faido Adit

Seven seismic profiles were measured by a team from the GFZ German Research Centre for Geosciences between September 2000 and June 2001 in the Faido Adit, which is an escape and rescue adit of the Gotthard Base Tunnel. The breakthrough of the GBT took place in October 2010 and its approval for the use of public transportation shall take place in 2017. From that time onwards the GBT will constitute an important link in the Trans-European Transport Network (TEN-T).

With a length of 2600 m and a radius of 5 m, the Faido Adit was excavated by drill-and-blast method. The lithology exposed along the Faido Adit is separated into two units: the Leventina Gneiss (LeG) and the Lucomagno (LuG) Gneiss. These gneisses comprise the Penninic Gneiss zone and separate it into two parts - the southern (LeG) and the northern (LuG) sections. While the LeG constitutes a nappe made up of orthogneisses, the LuG has a mixed lithology with ortho- and paragneisses of slightly varying mineralogical

composition. The LeG/LuG boundary is complex and overprinted by isoclinal folds (Etter, 1999; Pettke and Klaper, 1992; Casaopra, 1939). In Figure 2.1 the regional geological setting and a strongly simplified geological cross section along the Faido Adit and GBT are depicted. The Leventina-Lucomagno boundary is visible in the adit between tunnel meter 1880 and 2180 (Fig. 2.2 f). Both the LeG and LuG gneisses are composed of multiple deformed and metamorphically overprinted rocks of mainly granitic origin. The LeG and LuG exhibit various fabrics from laminated, augen-structured to porphyric or schistic.

In both gneiss varieties, parallel mica minerals and aligned quartz and feldspar minerals (Casaopra, 1939) characterize the well developed schistosity. In the LeG, the older schistosity *ss1* that generally dips 10-30° N, is overprinted and folded irregularly by schistosity *ss2* that developed during the Alpine orogenesis. The *ss1* is not visible at a macro scale in the Faido Adit and therefore not included in this work as micro-structures are not incorporated into the RQD or RMR classification schemes; however, their influence on the seismic velocities is acknowledged. From an average dip of 10-30° S in the LeG, the *ss2*-schistosity steepens to almost a 90° dip at the Leventina/Lucomagno nappe-boundary and stays at a dip angle of 70 to 90° S in the LuG.

Rock-Mass Properties along the Faido Survey

The geological data in both surveys was semi-quantitatively acquired from a strictly geoengineering point of view during the excavation process. The usual way of mapping rock-mass characteristics, referred to as geologic features in the following chapters that are concerned with SVMs, is to determine homogeneous areas for each geologic feature along the tunnel profile. That means, the surveyed tunnel section is separated into areas of constant values for a specific feature characteristic, e.g., areas of constant σ_c values. As the determined value holds true for each point inside the homogeneous area, the geological feature is regarded to be continuously logged along the profile (Bieniawski, 1973). Therefore, even if the, e.g., σ_c values are only determined when variations in the lithology occur, the data can be used jointly afterwards with a constant grid-size sampling of seismic velocities (cf. Sec. 2.2.1 and Sec. 2.2.2).

In the Faido Adit, measurements were restricted to the left (in the advance direction) or NW tunnel side along seven seismic profiles, each of ~70-meter length. The geological data mapped along the curved tunnel perimeter are projected onto a two-dimensional plane, called an unrolled geological cross section (Fig. 2.2). Four major faulted and fractured zones that are encountered along the surveyed sections are depicted in Figure 2.3. A fault zone occurs between 960-980 m but continues outside the survey for several meters (Fig. 2.2 a) and a gentle dipping mylonitic shear zone is visible between 1170 to 1200 m (Fig.

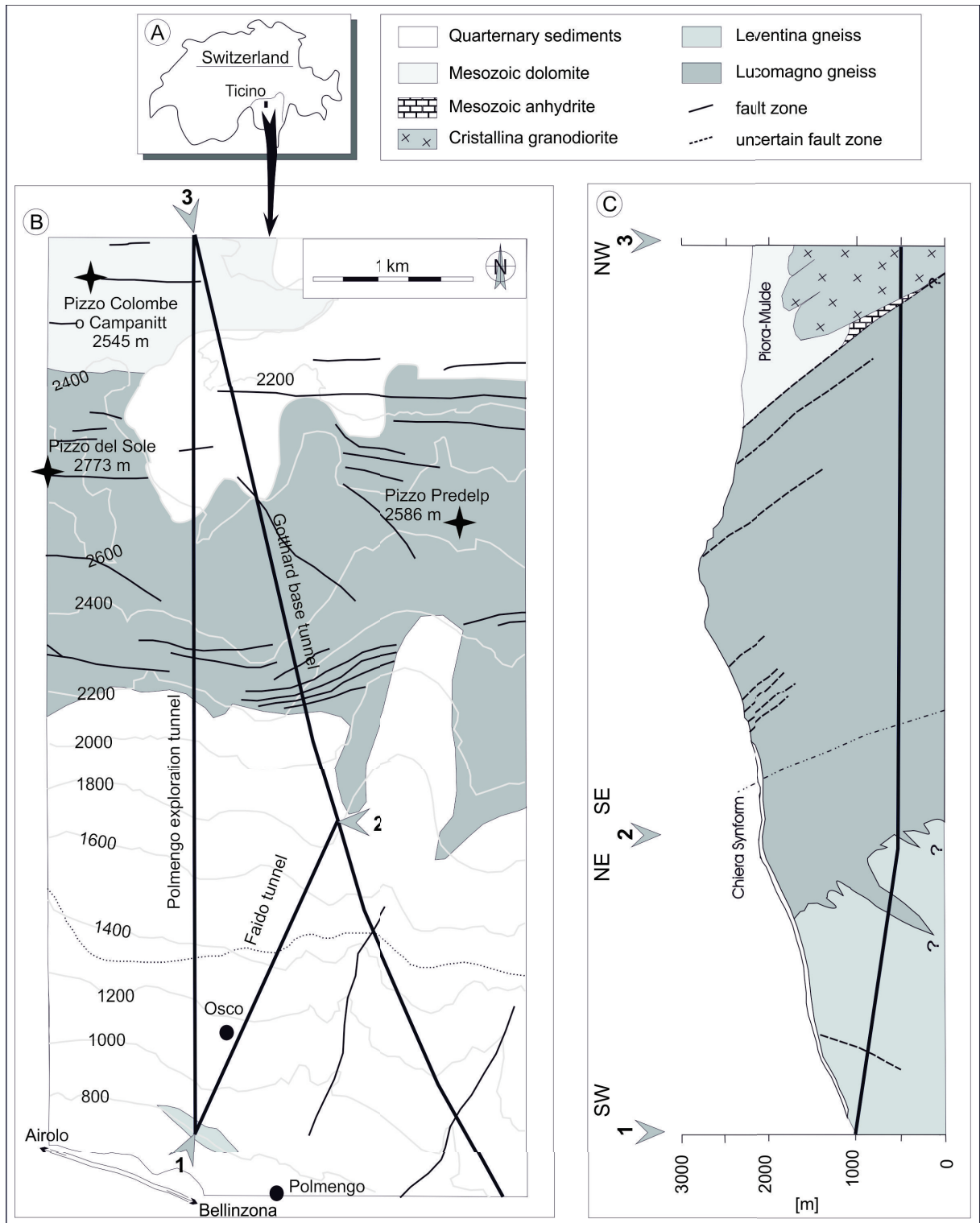


Figure 2.1: Overview of the geographic position and geological setting of the Faido Adit in southern Switzerland (modified after Klose, 2004). A) location of the construction site. B) simplified geological map and C) sketch of the geological cross section along the Faido Adit 12 and part of the Gotthard base tunnel 23 .

2.2 b). This shear zone is important to tunnel constructions because it runs parallel to the tunnel axis so that the impact of the structure on the tunnel support design is significant, because a stronger reinforcement is required along the whole structure. A densely fractured zone occurs around 2200 m (Fig. 2.2 f) and a smaller, 30-cm thick cataclastite is found at tunnel meter 2410 in Figure 2.2 g.

The σ_c values were quantitatively measured perpendicular to the schistosity for both the Leventina gneiss (LeG) and Lucomagno gneiss (LuG). The relationships between the uniaxial compressive strength σ_c and the gneiss varieties were determined by Schneider (1997) during the excavation of the Polmengo Adit, which also belongs to the tunnel construction work for the GBT. The σ_c values, for both the LeG and LuG, at a given tunnel location were determined by averaging the σ_c values of the gneiss fabrics (Eq. 1.4.2 and Klose, 2004). The averaged results of σ_c values along the adit are depicted in Figure 2.3. The gneiss varieties and the water inflow Q were determined from tunnel-face maps. For a more detailed description and listing of the average σ_c values, refer to Klose (2004), who investigated the relationships between single geological features and seismic parameters in the Faido Adit with self-organizing maps, a special type of ANNs.

The discontinuity properties, such as the discontinuity spacing and orientation, are semi-quantitatively measured along the seismic profiles (Klose, 2004). The infilling f was classified as either "none" or "hard infilling" (cf. Chap. 1.4), while the aperture e varied from 1 to 3 mm, and also only two roughness r classes ("very rough" and "rough") were determined (the survey areas are marked light gray in Fig. 2.3). The water inflow Q , outlined in the tunnel-face map descriptions, was characterized by Klose (2004) as mostly "dry" and partially as "dripping".

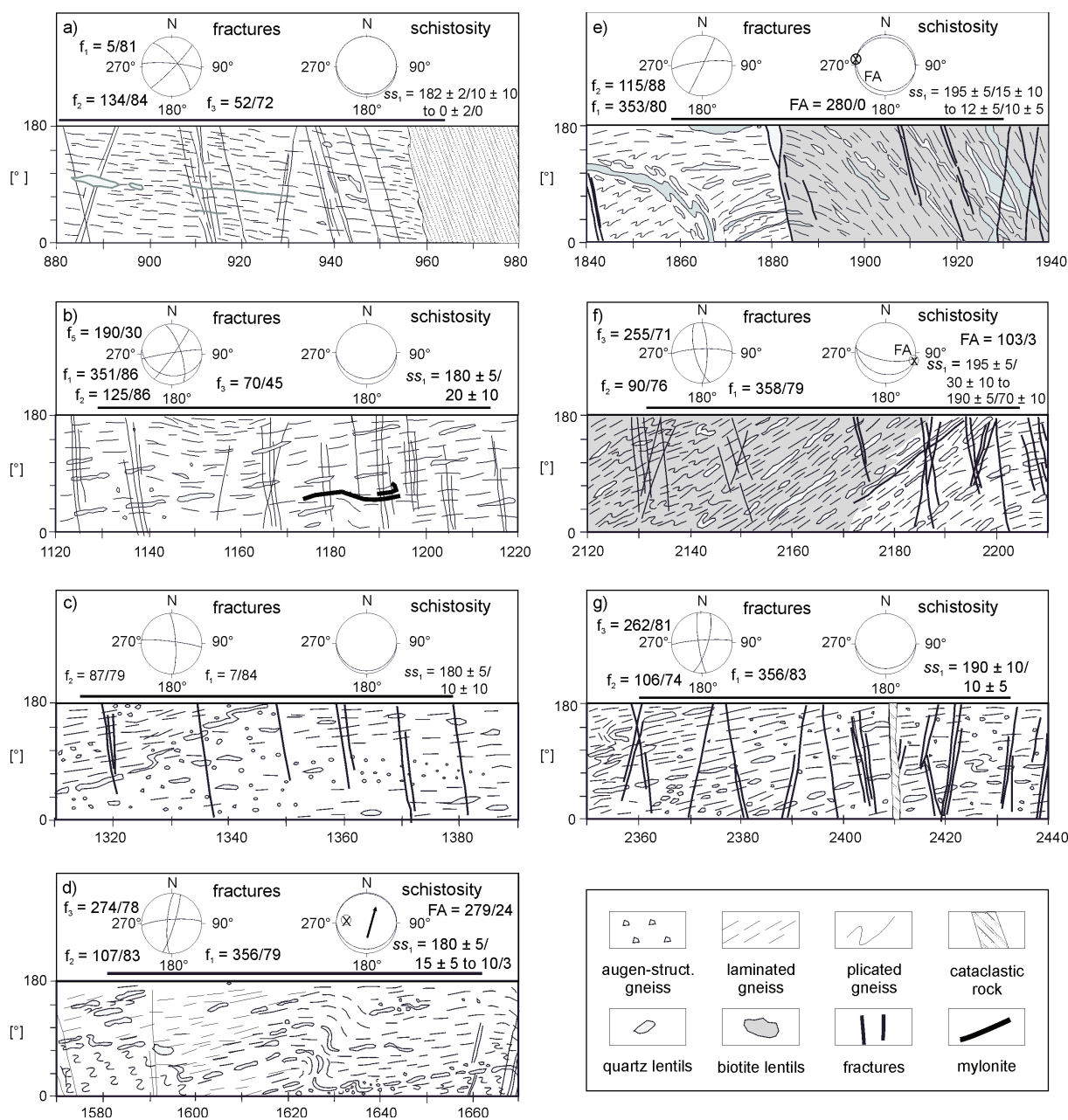


Figure 2.2: Unrolled geological cross sections (exaggeration 5:1) along the seismically surveyed NW tunnel wall of the Faido Adit between tunnel meter 880 m and 2240 m (modified after Klose, 2004): (a) a cataclastic fault zone crops out between 960 m to the end of the profile at 980 m but continues outside the survey, (b) a mylonitic shear-band occurs between 1170 and 1200 m. In (d) irregular small scale folding is apparent between 1858 m and 1920 m while in (f) a larger fold structure is sketched between 1582 and 1663 m. The LuG crops out only in cross sections (e) and (f) (shaded dark gray) between tunnel meter 1880 m and 2190 m. The rock in (e) is folded as general orientation of fractures and schistosity are depicted in the stereographic plots above the corresponding cross section. The black bars on top of the cross sections mark the start and end of the seismic survey layout.

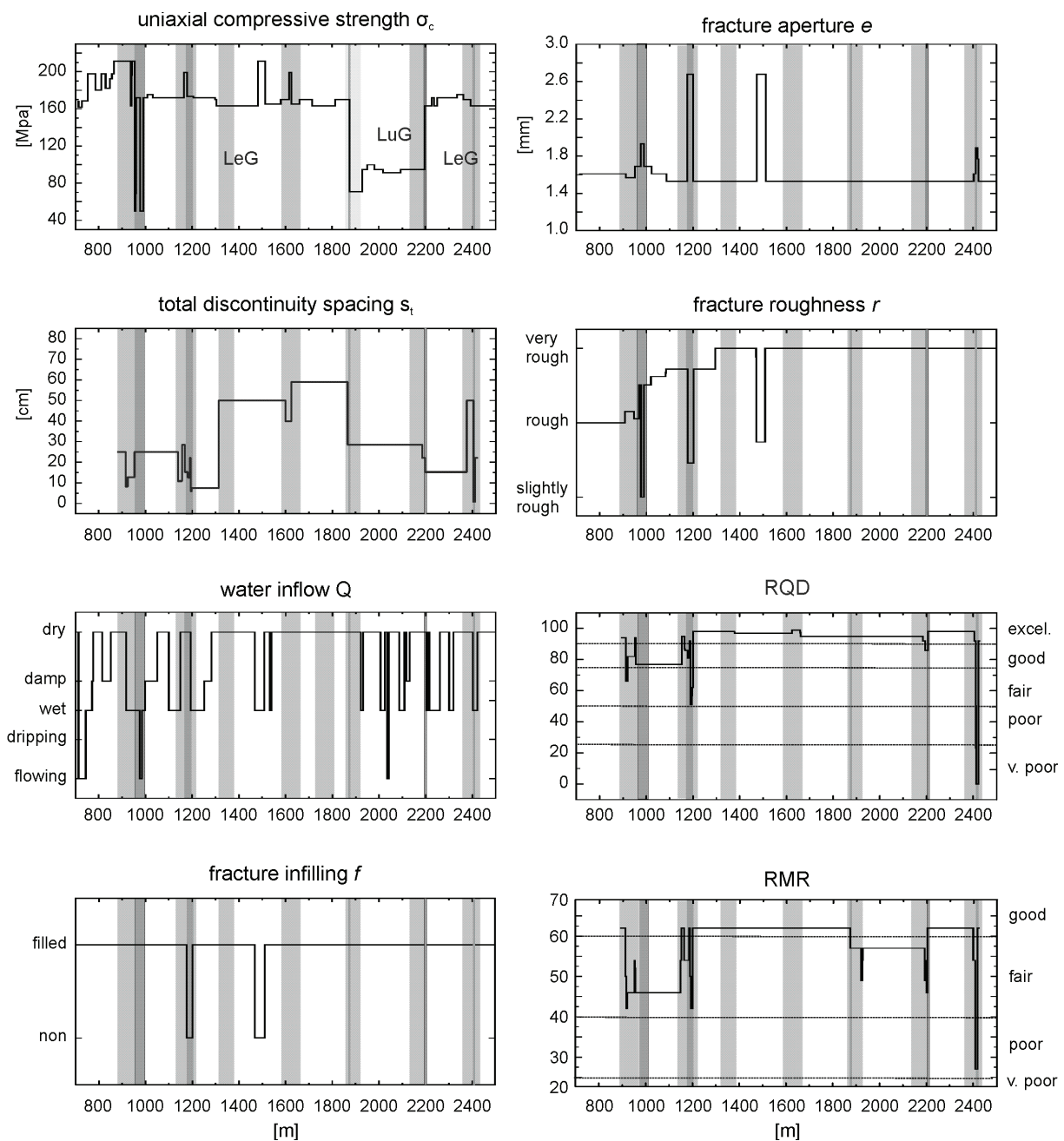


Figure 2.3: Rock-mass properties (σ , s_t , Q , f , e , r , $TRQD$, RMR) along the Faïdo Adit (modified after Klose, 2004). Tunnel sections, where seismic surveys took place are highlighted light gray. Darker gray bars mark geotechnically interesting geological events. At 960-1005 m and 2410 m a cataclastite is visible, a mylonitic shear band occurs at 1170-1200 m, the LeG/LuG boundary crops out at 1880 m and at 2200 m. At 2200 m a densely fractured zones has been mapped.

In general, the rock along the surveyed sections of the Faïdo Adit show geotechnically homogeneous behavior, so that the major discrepancies in rock-mass characteristics are expected in the densely fractured or faulted areas. The cataclastite at 960-1005 m is defined by extremely low σ_c , but has a less marked reduction in s_t values, resulting in relatively

high TRQD-values. Moreover, a higher water inflow Q was determined. At tunnel meter 2410 m, a thin but densely fractured cataclastic zone crops out that is reflected in the very low TRQD and s_t values. The σ_c values of the LuG are low compared to those of the LeG, but the other features do not show significant changes where the LuG crops out. Thus, the reduction of RMR-values is not very distinctive. On the other hand, the mylonitic shear band does not influence the uniaxial compressive strength σ_c , but at this point the increased fracture aperture e , combined with a decrease in fracture roughness r and no discontinuity infilling f , leads to geotechnically unfavorable rock conditions. The RMR-values are thus relatively low at this tunnel location.

The main orientation of each discontinuity family is depicted in stereographic equal area plots above the corresponding cross section in Figure 2.2. As outlined in Klose (2004), the three main joint sets (j_1, j_2, j_3) show the following orientations:

Joint Set	Dip Direction	Dip Angle
	[°]	[°]
j_1	356	84
j_2	125	80
j_3	90	79

Table 2.1: Orientation of the three major joint sets occurring in the Leventina and Lucomagno gneisses along the Faido Adit.

2.1.2 Geological Setting of the Glendoe Tunnel

In 2007, seismic measurements were carried out in the headrace tunnel of the Glendoe Hydro Electric Power Plant along a 300-m long profile in a cooperation between the GFZ German Research Center for Geosciences and Herrenknecht AG. Along the seismic profile, geotechnically relevant geological parameters and tunnel-driving parameters from the excavating open gripper tunnel-boring machine were collected. The power plant is situated at the southeastern lakefront of Loch Ness near Fort Augustus in the Inverness-shire (Scottish Highlands/UK) and has a capacity of 100 MW. The headrace tunnel –the lower part of the main tunnel–, is 8.1 km long and 4.8 m wide. The power plant started producing electricity in December 2008 but was forced to close temporarily in July 2009 because of a rockfall near the top of the main tunnel, which connects the water reservoir and Loch Ness with an altitude difference of 600 m. At the present time, the power station remains unoperational.

The tunnel-construction site is situated to the southeast of the Great Glen Fault that crosses Loch Ness and constitutes the border between the Neoproterozoic Moine and

Dalradian Supergroup (Dempster et al., 2002). The SE-NW striking headrace tunnel, in which the survey took place, is built into the regionally metamorphosed strata of the Dalradian metasediments (Fig. 2.4). The rocks along the tunnel profile are dominated by interbedded sequences of quartz-mica schists, micaceous quartz schists and quartz schists (Jacobs, 2004; SSE, 2004a). Metapelites and Metapsammites of amphibolitic facies are interbedded at a scale of 5-20 cm, so individual rock types cannot be mapped (May and Highton, 1997). As a result of three separate tectonic events that occurred during the Caledonian Orogenesis (Johnson et al., 1979; Jacobs, 2004), the strata along the tunnel alignment is occupied by large NE-SW trending folds (May and Highton, 1997). The latter include the Corrieyairack Synform and, further to the NW, the complimentary Tarff Anticline and Tarff Syncline (Fig. 2.4). Minor related folds, formed during the regional deformation, plunge at low to moderate angles in the same direction as the NNE-trending subvertical axial plane of the Tarff Syncline (May and Highton, 1997).

The surveyed tunnel section is located in the northwestern flank of the Tarff Syncline, which is part of the Tarff Banded Formation, consisting of quartz-mica schists, quartz schists, and quartzites. The classification of rocks in the tunnel survey into one of these lithologies depends on the mica content and the spacing of the foliation (SSE, 2004a), such that:

- Quartz-mica schists (QMS) are generally thinly banded with a well developed schistosity and mm-thick bands of mica.
- Quartz schists (QS) are mostly thick beds displaying faint schistosity (mainly observable in thin sections) and have a mica content < 10%.
- Quartzites (Q) form beds of 50 to 500-mm width and contain little to no mica.

The primary discontinuities of the rock mass are formed by a foliation developed along the mica-rich beds, which most likely corresponds to the original orientation of the sedimentary bedding planes (May and Highton, 1997). Large- and small-scale folding caused the development of a schistosity, which, according to televiewer results (Jacobs, 2004), often seems to coincide with the foliation. In the planning phase of the construction site, preliminary investigations suggested that the Rheidean fault, interpreted from linear features in the British Geological Survey (BGS) mapping (BGS, 1993) as well as in aerial photographs, might be exposed in the surveyed tunnel section (Fig. 2.4). This was not validated during the survey.

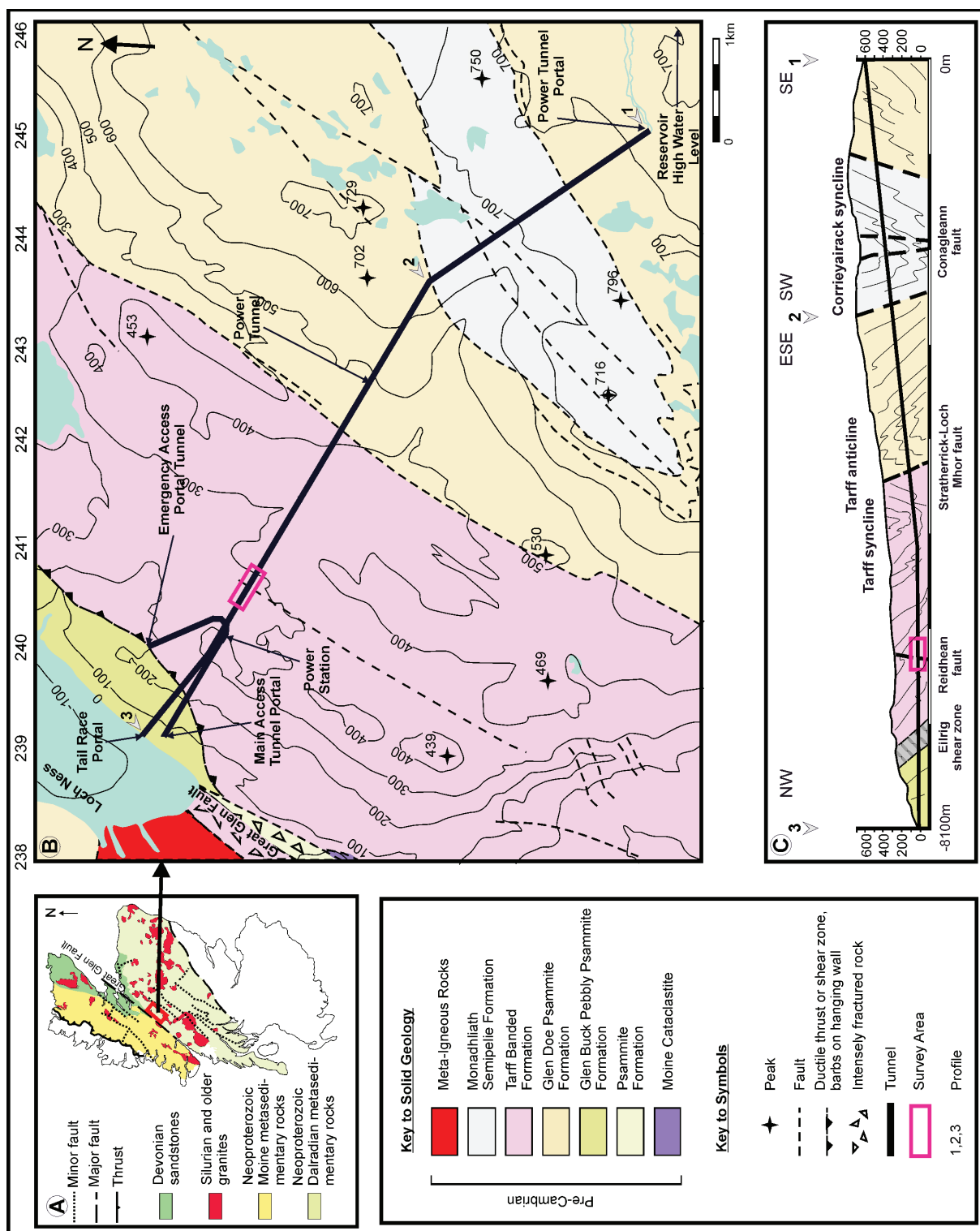


Figure 2.4: Geological setting of the Glendoe Hydro Electric Power Plant. (a) Overview of the regional geology and the location of the construction site. (b) Geological map of the construction site area SE of Loch Ness in the Scottish Highlands (based on: Jacobs, 2004, BGS, 1993, BGS, 1996 and Fettes, 1979). (c) Geological cross section along the power tunnel (source: SSE, 2004b).

Rock-Mass Properties along the Glendoe Survey

During the seismic measurements in the Glendoe Hydro Electric Power Plant, geological mapping of a tunnel wall was carried out by Herrenknecht AG (Heim, 2007). In Figure 2.5, the unrolled perimeter map of the tunnel wall is depicted. The lithologies encountered are quartz schist and quartz-mica schist. The quartz schist crops out between -6440 m and -6490 m, alternating with quartz-mica schist on a small scale between -6440 and -6340 m as well as between -6165 and -6152 m. The major part of the surveyed tunnel section is composed of quartz-mica schist. The rock is characterized by small-scale faults and joints, striking mostly WSW-ENE, with a major dip direction of 60° S. Similarly, the schistosity typically dips 55-60° SE (Fig. 2.5). No characteristic joint sets could be distinguished along the survey, in accordance with the evaluation of televiewer loggings in the Tarff Banded Formation (SSE, 2007, 2004b). From the above findings, it follows that the rock along the surveyed section of the Glendoe Tunnel is geotechnically quite homogeneous and the main foliation and fracture orientation in the rocks are generally the same. The rock condition (and the stability of the excavation) is therefore expected to depend mainly on the degree of jointing, the condition of the discontinuities, and the presence of local sheared zones.

The geological tunnel-wall mapping done by Herrenknecht (Heim, 2007) indicated several fault zones of one to several meters width along the geological tunnel profile (Fig. 2.5 b). The location and appearance of the more important of these zones are summarized in Table 2.2.

Tunnel Meter		Specification
from	to	
-6485	-6482	single fault ~1 m in width
-6409	-6405	single fault ~1 m in width
-6373	-6358	increased number of faults
-6334	-6322	increased number of faults
-6322	-6319	rock intensely faulted and fractured
-6257	-6253	~2m wide fault zone
-6253	-6225	increased number of smaller faults
-6157	-6148	strongly faulted
-6090	-6083	strongly faulted

Table 2.2: Location and appearance of geotechnically important structures along the Glendoe Tunnel surveyed area. The most pronounced faulting and fracturing occurred between tunnel meter -6329 and -6319, where the TBM-gripper sank into the tunnel wall.

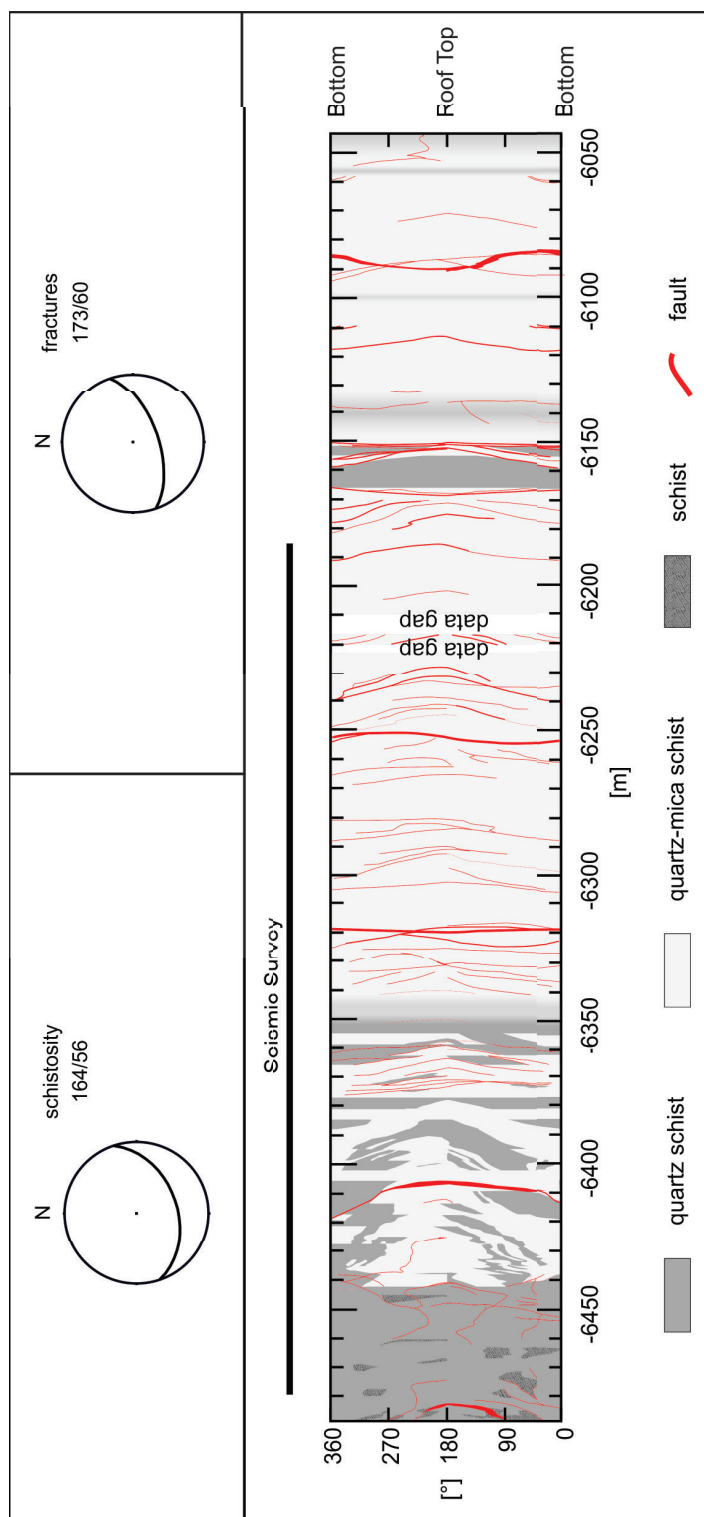


Figure 2.5: Unrolled geological cross section along the seismic survey in the Glendoe Tunnel. (a) Stereographic projection of the main dip of schistosity. (b) Stereographic projection of the main dip of faults and joints. (c) Unrolled geological tunnel wall mapping of the surveyed tunnel section. The white bars mark gaps in the geological dataset. The tunnel reference meter are in ascending order from -6490 to -6040, as the tunnel was referenced from -8100 m to 0 during construction, from the water reservoir to the Loch Ness, respectively (based on the tunnel wall mapping by Heim, 2007).

From a borehole investigation, it was determined that the general uniaxial compressive strength σ_c of the Tarff banded formation is approximately $65.85 \pm 45.14(MPa)$ (Jacobs, 2004; SSE, 2004a) and that the cohesion along the banding and foliation is generally strong, thus the banding does not constitute weak zones in the rock. During the survey, quartz-mica schist and quartz schist were recorded. The σ_c values of these rock types do not significantly differ from each other, as described in the ground reference report by SSE (2004a).

The fractures are mainly closed but show high aperture e of 300 to 400 mm between tunnel meter (TM) -6257 and -6249 and near meter -6094, coinciding with fault zones as indicated in Figure 2.6 and Table 2.2. Such a large aperture is unrealistic, however, and does not match the sketches made of the geological situation during the excavation. It is therefore concluded that these values are likely to be caused by a transcription error. Four out of five possible classes for fracture roughness r (from rough to slickensided, cf. Sec. 1.4) were recorded, and over large distances the roughness r is predominantly smooth. The geotechnically most unfavorable class "slickensided" was only identified outside of the seismic survey area, near -6050 m. The roughness is thus generally stronger in the gneisses of the Faido Adit than in the quartz-schists and quartz-mica schists of Glendoe. For the fracture infilling f the classes "no infilling", "hard infilling" were determined. More exact classification was not possible due to the semi-quantitative nature of the data acquisition. Three out of five classes were recorded for the water inflow Q along the profile. Those are "dry", "damp" and "wet", which indicates that no major water inflow took place; only two significant fault zones between -6257 and -6249 m were water-bearing.

As mentioned above, the rock exposed in the Glendoe Tunnel was continuously unweathered. The total discontinuity spacing s_t , as also outlined above, includes all kinds of discontinuities but does not include the schistosity. The graph in Figure 2.6 clearly shows that s_t is low along all faulted zones. The TRQD was determined from the reciprocal of s_t that equals the discontinuity frequency $\frac{1}{s_t}$ (Eq. 1.4.5). The two parameters, total discontinuity spacing s_t and TRQD, hereafter referred to as RQD for convenience, strongly influence the RMR but σ_c has no effect here, as it stays constant throughout the Tarff Banded Formation. The latter exhibits values that are mainly classified as "fair" to "good". The classes "very good" and "poor" are only realized in small intervals. Both the RQD and RMR do reflect low values along densely faulted and fractured areas; however, the realized range of values is small so that the classification by SVMs deals only with small variations in the data.

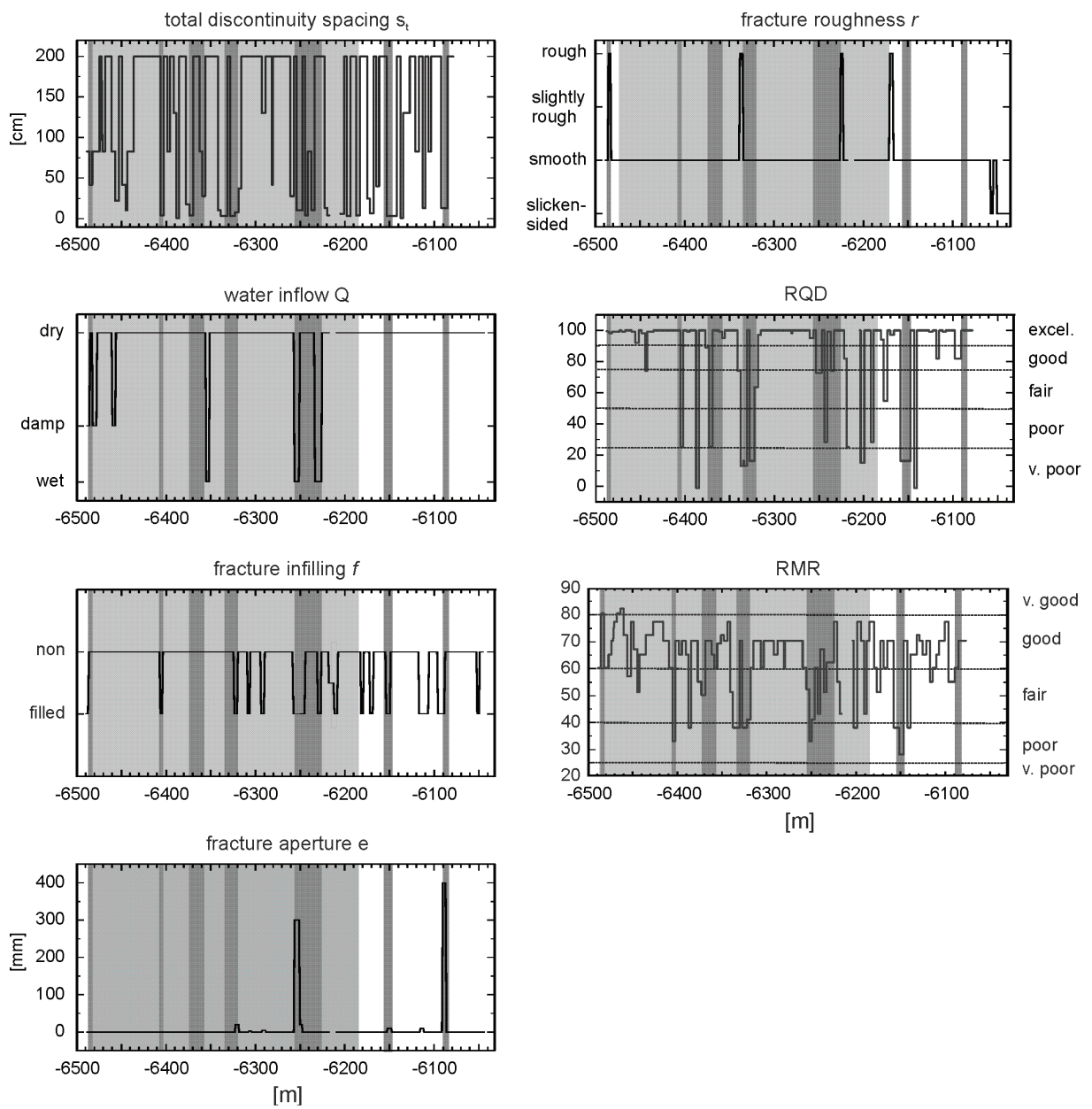


Figure 2.6: Rock-mass properties (s_t , Q , f , e , r , RMR , $TRQD$) along the seismic survey in the Glendoe Tunnel. The seismic survey area is highlighted light gray. Darker gray bars mark faulted to densely faulted areas.

2.2 Seismic Measurements

2.2.1 Seismic Data Acquisition in the Faido Adit

Seven seismic campaigns, approximately 70 m in length, were done between tunnel meter 880 and 2440 during the excavation of the 2600 m-long, NE-SW oriented Faido Adit. The measurement campaigns were carried out at intervals of about 200 m. Each seismic profile began less than 10 m behind the advancing tunnel face. As the tunnel was excavated with the drill and blast method, the seismic source (cf. Sec. 1.7) was moved independently. Eight to ten 3-component receivers, installed on rock anchors drilled two meters deep into the left tunnel wall (referring to the tunnel advance direction, cf. Sec. 1.7), were recording simultaneously along each profile. One rock anchor was positioned on the opposite wall of the tunnel to control several guided waves along and around the tunnel surface.

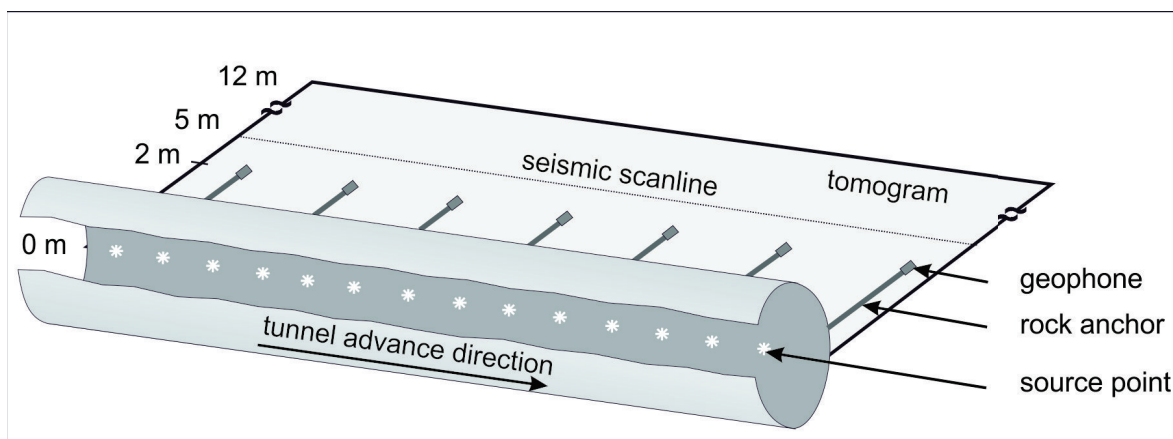


Figure 2.7: General source and receiver geometry of the seismic surveys in the Faido Adit. The 2-D tomograms were calculated along planes that extend perpendicularly from the left tunnel wall (source: Klose, 2004).

Average distances between the receivers of around 9 m and a source point interval of 1 to 1.5 meters were realized. The maximum source-receiver offsets were between 50 to 70 m. An overview of the seismic measurements can be found in Giese et al. (2005). For a more detailed description of the seismic data, refer to Klose (2004).

The S- and P-waves showed average velocities of $3200 \frac{m}{s}$ and $5640 \frac{m}{s}$, respectively. In general the P-waves displayed frequencies of 800 to 1000 Hz and the S-waves frequencies of 400 to 600 Hz with a wave length of about $\lambda = \frac{v}{f} \approx 4.8m$ to $8.8m$. P- and S-wave velocity tomograms were computed by imaging elastic rock mass properties along the tunnel with the commercial software package PROMAX (Klose, 2004). The travel-time tomographic inversions were generated as horizontal planes connecting the geophone anchors and the source points (Fig. 2.7).

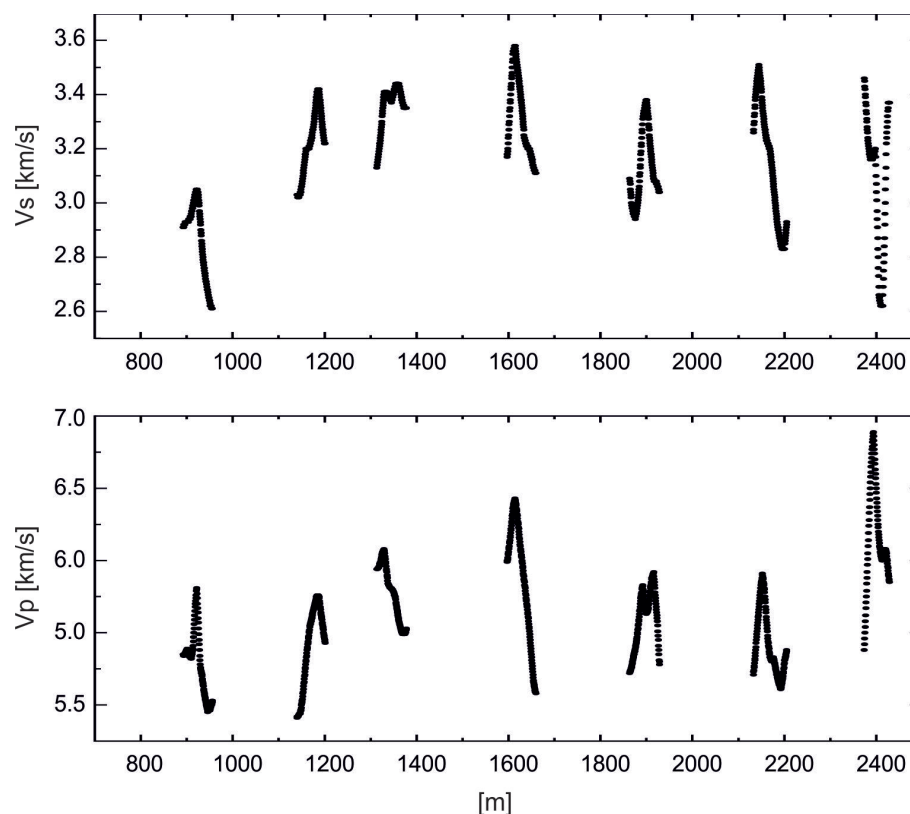


Figure 2.8: Seismic P- and S-wave velocities along the seismic profiles in the Faïdo Adit (source: Giese et al., 2005 and Klose, 2004).

Several tomograms with cell sizes (x,y) , where x is the cell length in tunnel advance direction and y the horizontal distance perpendicular to the tunnel wall, were evaluated (cell sizes: 4×1 , 8×2 , 12×3 , 16×4 and 20×5 m) and then combined into one model of cell length $x = 0.5$ m. A detailed description of the layout of the tomograms can be found in Giese et al. (2005). The seismic velocities were acquired (Fig. 2.8) from the tomograms along scanlines 5 m deep into the tunnel wall to avoid the influence of the excavation damage zone (EDZ). In the tunnel near-field, micro-cracks develop and previously-existing cracks open as a result of the excavation process, forming the EDZ. The influence of the EDZ decreases from the tunnel wall into the rock (Martino and Chandler, 2004). Klose (2004) argues that the differences between the geology mapped along the tunnel wall and the geology at a depth of 5 m are negligible, and the use of the latter rather than the former allows for a realistic comparison between seismic and geological data.

2.2.2 Seismic Data Acquisition in the Glendoe Tunnel

The main purpose of the survey in Glendoe was to show that on-site predictions of geologically hazardous structures in advance of tunneling are feasible using ISIS. The

method employs tunnel surface waves (TS-waves) that are converted into body waves at the tunnel face for the predictions of structures along the projected roadway (Fig. 2.10). The TS-waves propagate along the tunnel walls, dominating the wave field, as shown by finite-difference modeling and field observations at the Gotthard Base Tunnel construction site (Bohlen et al., 2007; Lüth et al., 2008a; Jetschny et al., 2010). It was shown by Lüth et al. (2008c) and Rechlin et al. (2009) that successful predictions can be made by visually comparing migration results and geological mapping, even though this requires the application of a homogeneous seismic velocity model.

The position of the pneumatic impact hammers was adapted to the characteristics of the open-gripper TBM by mounting them onto the grippers on each side of the tunnel boring machine via steel plates (Fig. 2.10). The hammers were triggered during each down-time of the TBM. Down-time occurs about every two meters, when a stroke is finished and the grippers are moved forward (cf. Sec. 1.5). In total, 289 source points with one to five repetitions were realized in the 4.8 m-wide tunnel between tunnel meter -6488.5 and -6195.3.

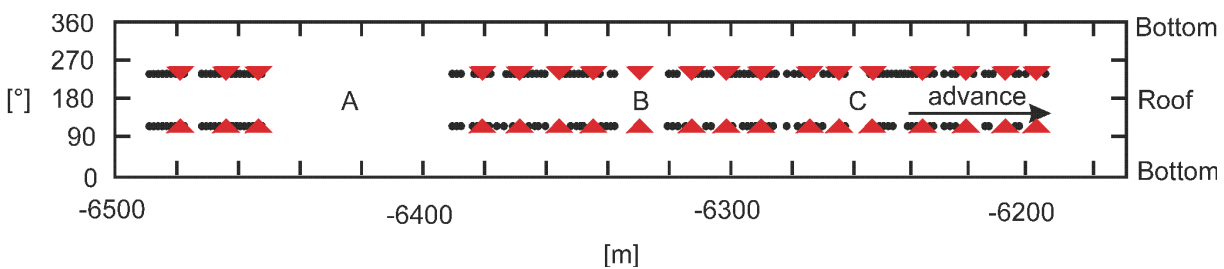


Figure 2.9: Schematic illustration (source: Lüth et al., 2009) of the shot (red triangles) and receiver (black dots) points of the seismic survey in the Glendoe Tunnel. Three interruptions (A,B,C) took place due to logistic problems. A: Movement of the data acquisition station. B: Safety inspection of the new data acquisition station. C: ~1h interruption with simultaneous fast TBM advance.

At each source point, also called shot points, a wave field is excited by a seismic source, here a pneumatic impact hammer. The excited wave field was usually recorded by four 3-component receivers, drilled one meter deep into the tunnel wall. The configuration was such that two geophones were positioned on either side of the tunnel at an angle of 130° (Fig. 2.9). Each pair of receivers was active for 15 m of excavation and then reinstalled 2 m behind the cutter head with a source-receiver offsets of 8 to 20 m, allowing the direct surface wave to occur within a small travel time interval. A total of 38 rods were installed between -6478.7 m and -6185 m, on either tunnel side (Fig. 2.9), with three interruptions that were caused by logistic problems.

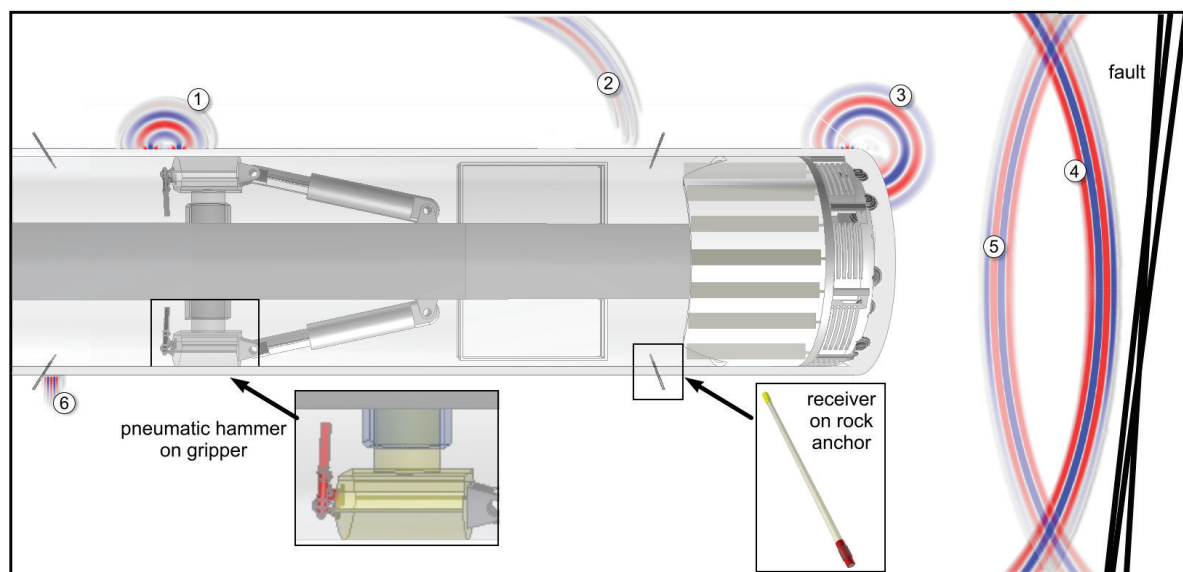


Figure 2.10: Configuration of the ISIS hardware on a tunnel-boring machine and schematic illustration of the wave-field propagation during the measurements in the Glendoe Tunnel (compiled based on Jetschny, 2010 and pers. communication Well, 2010). Two 3-component receivers and one pneumatic hammer were installed at either side of the tunnel. (1) The wave field is excited at the tunnel wall by one of the pneumatic hammers. Important for the prediction ahead of the tunnel is (2) the TS-wave, that is propagating along the tunnel wall to the cutter head where (3) it is converted to body-waves. (4) The converted P- and S-waves travel through the rock and are reflected e.g. at a fault zone. (5) The reflected waves are back-scattered and couple at the tunnel face, called TSST-waves after their travel path, and are recorded at the receivers. For the P- and S-wave velocities along the profile, the direct P- and S-waves were picked.

The processing of the seismic data was done using the ISIS-software. A detailed description of all possible processing steps can be found in Giese and Lüth (2008). Götz (2008) developed a heterogeneous seismic velocity model for the Glendoe survey based on seismic tomography with Singular Value Decomposition (SVD). Compared to the Faido survey, the geophone array and shot-point density were greatly reduced in this setup for TBM-integrated measurements. Thus, the data is noisier and of lower quality than the data in the Faido Adit. The grid for the SVD was defined along a 1D scatter-plot, by imaging the seismic velocities between the tunnel wall and a receiver depth of 1 m. The data in the near field showed a strong velocity dependence on the offset of the P- and S-waves so that a separation of S- and P-waves for offsets smaller than 2 m was not possible (Götz, 2008). Thus, only offsets greater than two meters were used for the velocity model. The model reliability of the SVD-tomograms is good for a cell size of 8 m, but acceptable results also were achieved with a cell size of 4 m. The results from the four-meter cell size were used for the rock-mass classification. The lower resolution of the eight-meter cell size, taking into

account the data gaps for the velocities mentioned above and the exclusion of noisy and time-shifted data, would reduce the size of the dataset too strongly for an implementation into a pattern recognition system. This means that the support vector machine introduced in Section 1.7 could not be trained sufficiently to allow for generalization on unknown data points, and thus a prediction would not be possible. Furthermore, a lower resolution would greatly reduce the possibility of detecting correlations between local geological structures and the velocities. This is especially important because of the small-scale nature of the structural inventory along the Glendoe survey (cf. Sec. 2.1.2).

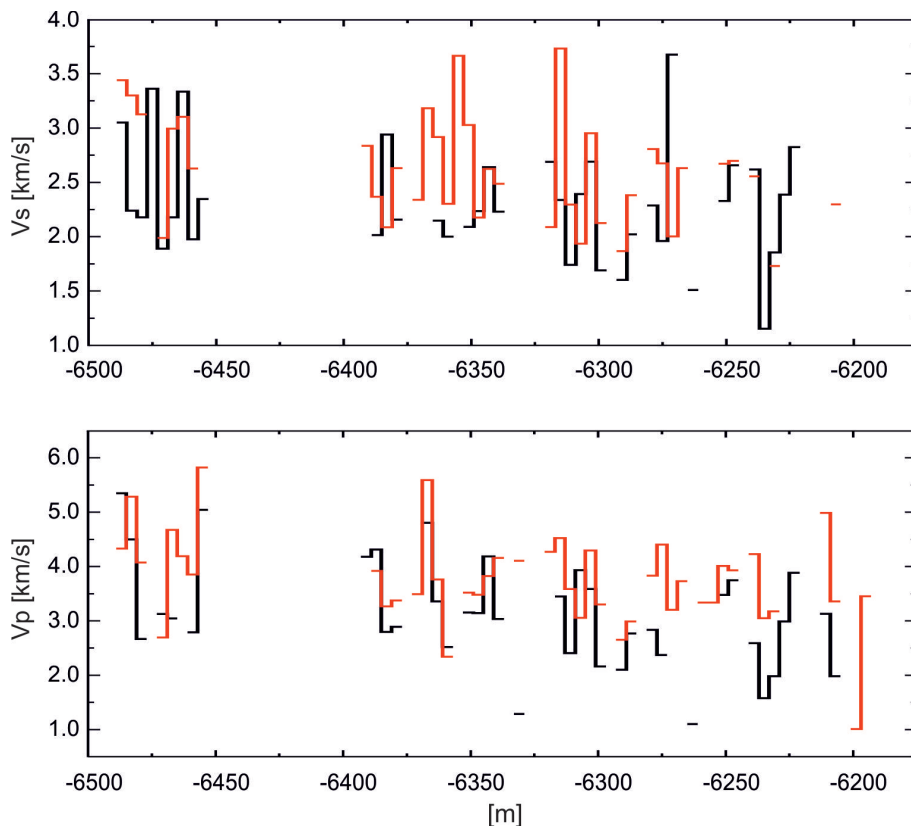


Figure 2.11: Seismic P- and S-wave velocities along the seismic profile in the Glendoe Tunnel. The seismic P- and S- wave velocities are depicted separately for the right (black) and the left (red) tunnel wall with locally strong variations. The data gaps are caused by three interruptions in the measurements and the exclusion of noisy and time-shifted data (source: Götz, 2008).

In general, the velocities lie within the expected range, with the exception of a few outliers. The S-wave and the P-wave velocities show an average of $2500 \frac{m}{s}$ and $3700 \frac{m}{s}$, respectively. Thus, the gneisses of the Faido Adit produced higher velocities than the quartz-mica schists of Glendoe. With a centre frequency around 250 Hz, the S-wave has a wave length of about $\lambda = \frac{v}{f} \approx 8 \text{ to } 10 \text{ m}$ Götz (2008). The seismic velocities in Figure 2.11 are shown separately for the left and the right tunnel wall. Locally strong variations in the velocities

of the same wave type from the left to the right tunnel wall are apparent. These variations, as interpreted by Götz (2008), are caused indirectly by the Excavation Damage Zone (EDZ) because the EDZ comprises increased microcracking that in conjunction with the small offsets in this study cause variations in the seismic velocities. Thus, only the average velocities were regarded in this work, to reduce the influence of the EDZ on the seismic data.

The velocity models from Glendoe and Faido are of different resolutions. Because the geology along the profiles was determined by defining homogeneous areas throughout the surveys, and each point in a homogeneous unit is defined by the same value (cf. Sec. 2.1.1), the seismic resolution was the limiting factor for the data-point density. The different cell sizes of the two surveys do not allow for a direct correlation of the data. Consequently, the datasets are treated separately in the following chapters, meaning that independent Support Vector Machines are developed for both surveys (cf. Chap. 4). For the implementation of a routine prediction system, it is desirable to unify the data acquisition such that results become available at smaller grid point intervals.

2.3 Acquisition of Tunnel-Driving Data in the Glendoe Tunnel

The close correlations between the thrust force, cutter head torque, cutter head speed, power consumption, penetration and advance speed parameters have been shown in Section 1.5.

The headrace tunnel in the Glendoe project has been excavated by an open single gripper-TBM. Its machine data was continuously measured and stored along the entire tunnel section investigated. The selection of the parameters regarded in this work is based on the interaction of the parameters outlined previously and the following considerations: The net advance speed as [mm/min], that is often equated with the drillability of a formation or homogeneous rock mass unit (Thuro and Brodbeck, 1998) is the net product of the penetration $[\frac{mm}{rev}]$ and the cutter head speed $[\frac{1}{min}]$. Therefore, penetration and advance speed do not need to be considered separately. Because of its independence to the cutter head speed, the penetration is preferred to the advance speed as a preliminary step for the transferal of the results of this study to other construction sites. The direct relation between power consumption pc [kW], and cutter head speed cs $[\frac{1}{min}]$ and cutter head torque ct [kNm] is described by:

$$pc = \frac{2 \times PI \times cs \times ct}{60}. \quad (2.3.1)$$

This relationship implies that only the power consumption or the cutter head speed and torque need to be taken into account. Maintaining the power consumption only would keep the feature matrix for the SVM small, which is desirable but may lead to a loss of information at the same time. Therefore, the parameters were explored statistically in Section 3.2 before the decision making.

The data collected in 10 s steps were sorted in Excel spreads for each day. Consequently, the concatenation of the data requires a considerable amount of sorting. Furthermore, data points collected during machine downtime were deleted from the dataset, as they represent zero values rather than actual geological conditions, and would create errors in the subsequent steps. To suppress noise and outliers, a Fast Fourier Transformation (FFT) and low pass filter were applied. All values were verified as positive, because negative values indicate measurement errors. It should be noted that the re-sorting process is specific to one project, as it depends on the recording process of the data and the hard- and software used. Further processing was restricted to the parameters enlarged upon in Section 1.5, to obtain a comparable dataset.

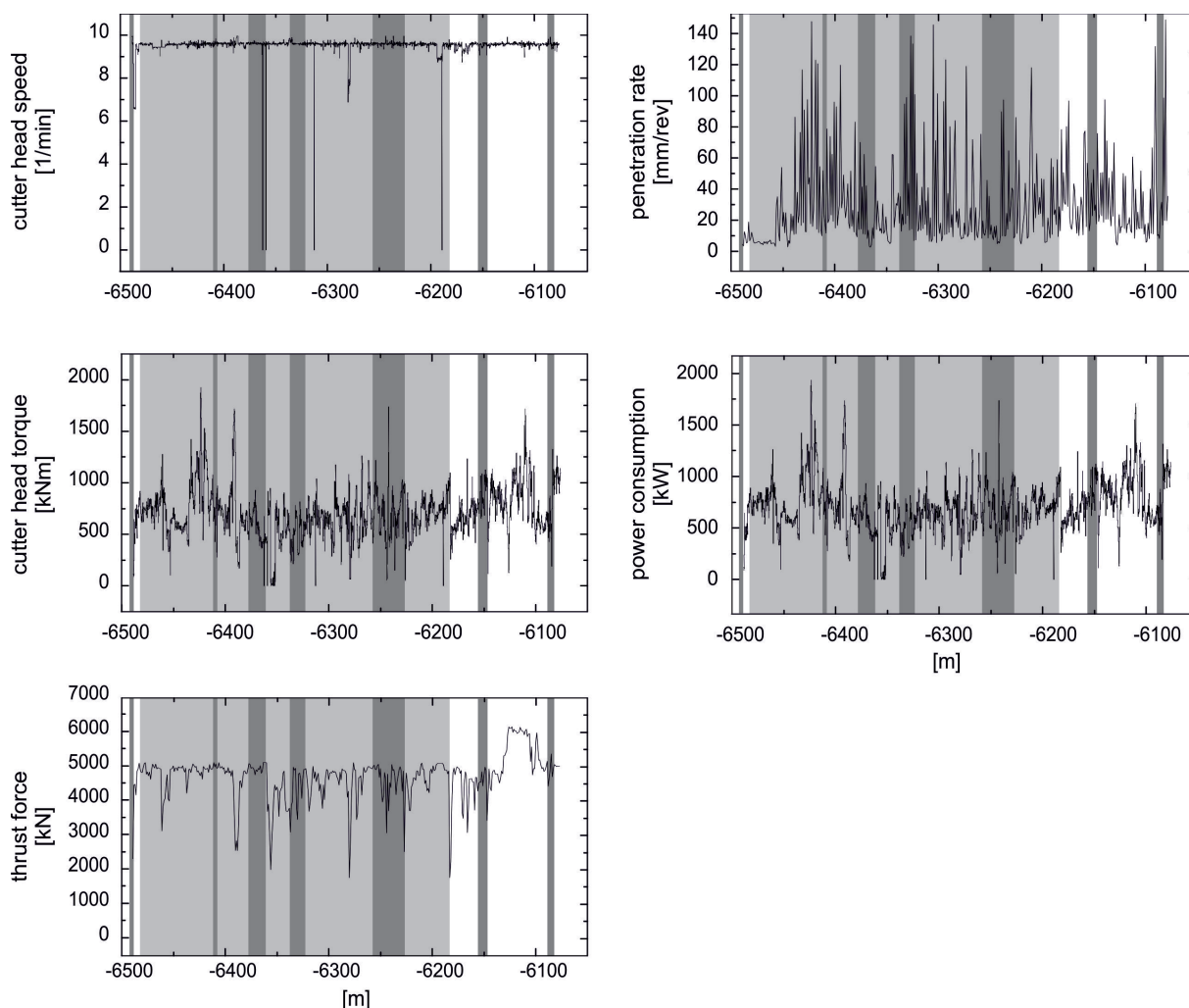


Figure 2.12: Tunnel-driving parameters along the survey in the Glendoe Tunnel were automatically acquired and stored. The advance speed is not considered further, as it was calculated directly from the penetration rate. The seismic survey area is highlighted light gray. Darker gray bars mark faulted to densely faulted areas.

As the data for the tunnel-boring machine was acquired in the time domain, the data needs to be converted to the space domain before further interpretation or processing can be carried out. The simplest way would be to use the penetration [mm/rev] in reference to the survey start. However, the values for penetration show a systematic error in the range of factor 3. Subsequently, this parameter could not be used for the determination of the tunnel meter achieved. Thus, all available specifications regarding the tunnel face position at a given time were considered (~every two meters, which is the length of a stroke) and further tunnel positions were linearly interpolated. In order to transform the data for the tunnel-boring machine from the time- into the space domain, the data was divided into bins in the next step. This way, a data-set of technical parameters with a sample grid of four meters cell length, in regard to the seismic tomogram, was created and incorporated

into the feature matrix (for the SVM) with the seismic data. However, the data point density for technical data is much greater than the seismic data so that information may be lost. Thus, a second dataset for the Glendoe Tunnel was created for a separate SVM construction with a smaller bin size of one meter.

3 Statistical Evaluation

The Rock Quality Designation Index (RQD) is easily obtained during tunnel construction (cf. Sec. 1.6 and 2.1) and provides a good first estimate of the rock-mass quality in terms of geotechnical applications. The discontinuity spacing that builds the basis for the RQD calculation is strongly related to seismic velocities; however, in contrast to the Rock Mass Rating System (RMR), the RQD lacks the incorporation of further parameters, such as the estimation of the discontinuity properties or the uniaxial compressive strength σ_c , necessary for thorough rock-mass characterization. One aim in this study is therefore to investigate whether the simpler RQD or the more elaborate RMR is better suited for a classification based on seismic velocities and tunnel-driving data. The RMR and the RQD data obtained in the field surveys are individually discussed and separately used as target variables for a rock-mass classification via support vector machines (SVMs). Before training the SVM, the data is analyzed with statistical methods to determine the data quality, to investigate the feasibility of the target variables (RQD and RMR) and to detect possible data correlations in the feature space.

3.1 Statistical Evaluation of the Faido Data Set

As the Faido Adit was excavated using the drill-and-blast method, no TBM data was collected for the Faido survey. Thus, the seismic P- and S-wave velocities (V_p and V_s , respectively) of seven seismic profiles constitute the data base for the classification of the rock into RMR or RQD classes. The data set contains a total of 897 samples with a grid spacing of 0.5 m along the tunnel wall.

The value distribution for all parameters is visualized as boxplots in Figure 3.1. Boxplots are non-parametric, i.e. they display differences between populations without making any assumptions of the underlying statistical distribution. The edges of the boxes are the 25th and 75th percentiles, P_{25} and P_{75} , and the distance between those edges is called the interquartile range that contains 50 % of the data. From both edges, so called whiskers extend outwards by up to 1.5 times the interquartile distance (1.5xIQD); their exact length is determined by the most extreme data point in the 1.5xIQD range. Data points outside this range are likely to be outliers and are plotted individually as red crosses.

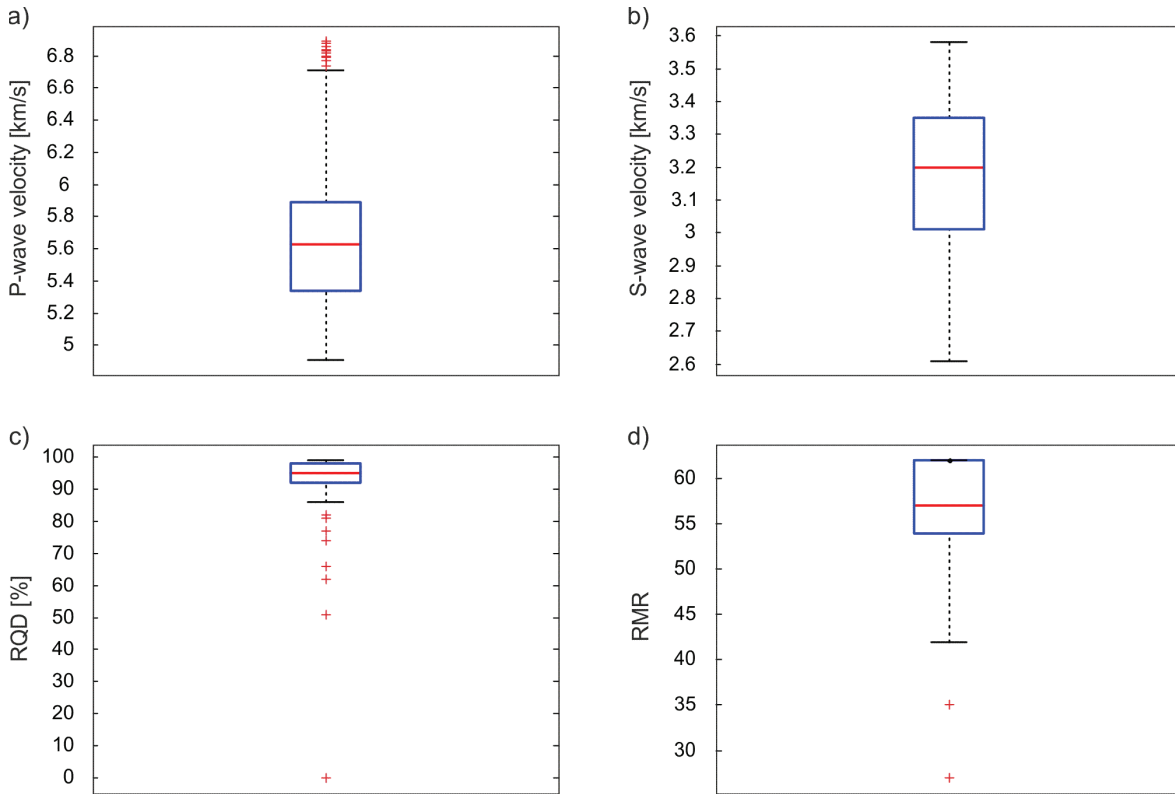


Figure 3.1: Boxplots of (a-b) the seismic velocities, (c) the RQD and (d) the RMR from the Faido Adit data set. The edges of the boxes are the 25th and 75th percentiles, P_{25} and P_{75} . The whiskers extend to the most extreme data points not considered outliers. Data points considered as potential outliers are plotted individually as red crosses.

For the seismic P-wave velocity V_p , the measured values lie in the range of 4.91 and $6.89 \left[\frac{km}{s} \right]$ with a median at $5.63 \left[\frac{km}{s} \right]$, a low skewness of 0.5 and a kurtosis nearing 3 (Tab. 3.1). The skewness describes the asymmetry of a distribution:

$$skewness = \left(\sum_{i=1}^N \frac{(x_i - \bar{x})^3}{s^3} \right),$$

and is 0 for a symmetric normal distribution. How peaked or flattened a distribution is in relation to the normal distribution is described by the kurtosis:

$$kurtosis = \sum_{i=1}^N \frac{(x_i - \bar{x})^4}{s^4}.$$

A distribution more strongly peaked than the normal distribution has a kurtosis of > 3 , while a kurtosis < 3 marks a flat distribution with heavy wings. Thus, the distribution of V_p is close to normal distribution. The skewness is also visualized in the boxplots by the position of the mean value with regard to the box edges, while the kurtosis can be

approximately determined by regarding the box width (Fig. 3.1). The seismic S-wave velocity V_s ranges between 2.61 and 3.58 $\left[\frac{km}{s}\right]$ with a mean value of 3.2 $\left[\frac{km}{s}\right]$. Similar to V_p , the S-wave velocity exhibits nearly normal distribution, expressed in a small skewness of -0.53 and a kurtosis of 2.6 (Tab. 3.1).

	Min	Max	Mean	Median	Std. Dev.	Skew	Kurt	P_{25}	P_{75}
$V_p \left[\frac{km}{s}\right]$	4.91	6.89	5.64	5.63	0.4	0.5	3.09	5.34	5.89
$V_s \left[\frac{km}{s}\right]$	2.61	3.58	3.16	3.2	0.23	-0.53	2.6	3.01	3.35
RQD	0	99	90.12	95	16.22	-4.11	21.99	92	98
RMR	27	62	56.75	57	7.17	-1.9	7.27	54	62

Table 3.1: Basic statistics of the Faido Adit data. The sample distribution of the geotechnical parameters, especially the RQD, are strongly peaked and exhibit negative tails. P_{25} , P_{50} , P_{75} are the 25, 50 and 75 percentiles.

The defined range of 0 to 100 [%] RQD is nearly covered completely by the data samples in the Faido Adit (c.f. Sec. 1.4). Nonetheless, there is a wide gap in the range between 1 and 51 [%] (Fig. 3.1 c), while an extreme peakdness is observed in the narrow range between the 25th and 75th percentiles (Fig. 3.1 c and Tab. 3.1). Subsequently, a generally low degree of jointing can be assumed for the rocks in the Faido Adit. A significant number of samples with values < 86 [%] RQD are outside of the 1.5xIQD range, causing a strong negative tail that is expressed in a skewness of -4.11 . These data points are not interpreted as outliers as they are caused by locally increased fracturing or faulting.

The major goal of this study is to find out whether rock mass that exhibits geotechnically important structures can be identified using SVMs. Consequently, data samples with low RQD values should be regarded separately, if possible. 58 out of 897 samples in the Faido Adit data set are assigned to RQD values ≤ 75 [%]. After Deere and Deere (1988), rocks with a RQD ≤ 75 [%] are assumed to have a quality between “very poor” to “fair”; above that boundary, the rock is either “good” or “excellent” (c.f. Tab 1.1). The few samples in the range between 0 and 75 [%] RQD thus describe those rocks along the adit that are geotechnically most important; however, if the classes are extremely small, the self-learning algorithm is prone to over- or underfitting (c.f. 4). Thus, the data points that correspond

to classes of low rock-mass quality are merged in one class, while the distinction between RQD classes "good" and "excellent" remains:

- Class 1: "very poor" to "fair" rock-mass quality described by RQD values from 0 to 75 [%].
- Class 2: "good" rock-mass quality described by RQD values from 76 to 90 [%].
- Class 3: "excellent" rock-mass quality described by RQD values from 91 to 100 [%].

In comparison, the RMR exhibits less strong peakedness with a kurtosis of 7.27 (Tab. 3.1), even though the interquartile range that spans between 54 and 62 RMR (Fig. 3.1 d) is not significantly larger than that of the RQD. The upper whisker in the RMR boxplot is completely amiss so that the 75th percentile coincides with the maximum value, which indicates that 25 % of all data points are assigned to $RMR = 62$. Additionally, the range of values below the 25th percentile extends to $RMR = 27$, causing a negative skewness of -1.9. In consequence, most data points lie in the "fair" or "good" classes of the RMR classification scheme. Thereby, the peak of the distribution is in strong proximity to the corresponding class boundary (c.f. 1.4). The low variance in conjunction with the small range in the data distribution leads to the distinction of two classes for the RMR in the Faido Adit with the separating class boundary at $RMR = 60$:

- Class 1: low rock-mass quality including data points of the class "fair" and lower, described by RMR values from 0 to 60.
- Class 2: high rock-mass quality including data points of the class "good" and higher, described by RMR values from 61 to 100.

The challenge in this classification task is to distinguish between two neighboring classes on the basis of a real and therefore noised data set, in which the majority of samples lies close to the class boundary.

As described in Section 1.6 by Equation 1.6.4 and 1.6.5, a logarithmic correlation resides between the RQD and the Young's modulus E_{dyn} , as much as a linear correlation exists between the RMR and E_{dyn} . These relationships are determined as null hypothesis for RQD or RMR with E_{dyn} , respectively. The Young's modulus E_{dyn} is calculated based on the in-situ bulk density ρ_b and the Poisson's ratio ν that in turn is calculated from the seismic body-wave velocities (Eq. 1.6.2 to 1.6.3). Constant values of ρ_b for either gneisses and quartz-mica schists –given by Telford et al. (1990)–, were used to calculate the Poisson's ratio ν . In consequence, the variance in the Young's modulus E_{dyn} is solely caused by the seismic velocities. The null hypothesis for the RQD correlation to E_{dyn} could not be rejected, as the correlation coefficient $r = 0.0518$ nears 0. The same holds true for the null hypothesis of a linear correlation between E_{dyn} and RMR. Here, the

correlation coefficient $r = 0.2432$ is also far below the significance level selected at 0.95 (Fig. 3.2). In addition to the regression curves between E_{dyn} and the measured RQD or RMR values, the Young's modulus E_{dyn} is additionally plotted against the theoretically determined RQD and RMR values, respectively, obtained by Equation 1.6.4 and 1.6.5 (Fig. 8.1). For both, RQD and RMR, the theoretically determined values are much higher than the actually measured values, even though the slopes are similar. Moreover, the theoretically determined RQD values are outside the defined range between 0 to 100 [%]. The relationship described by El-Naqa (1996) could thus not be verified for the Faido Adit.

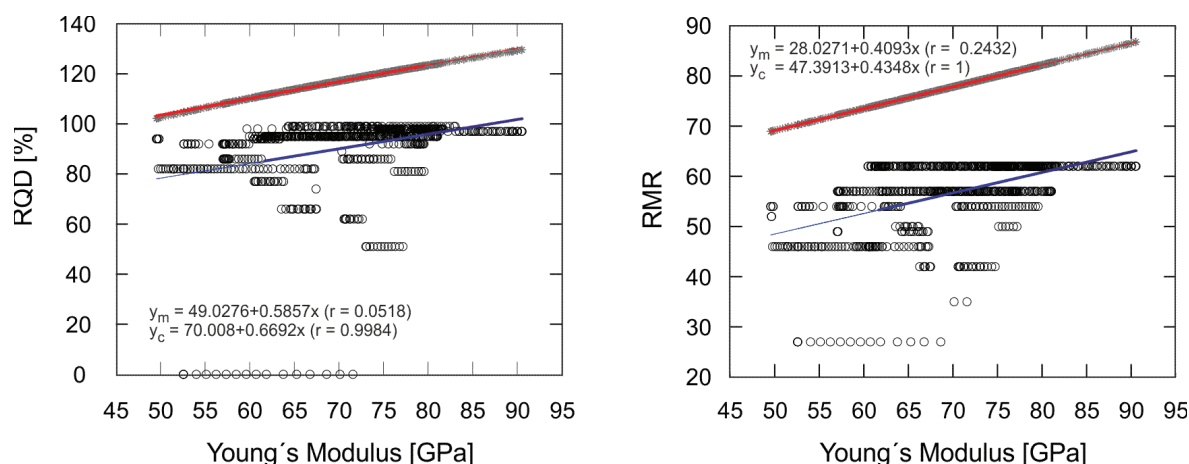


Figure 3.2: Relationship between elastic dynamic modulus E_{dyn} and rock-mass quality descriptive parameters RQD (left) and RMR (right). No correlation was detected during regression of the collected data (regression line y_m) and E_{dyn} . The RQD or RMR values calculated using the Equations set by El-Naqa (1996) are significantly larger than the measured values but the curve trends exhibit similar slopes. In case of the RQD, the theoretically determined values lie outside of the defined range between 0 to 100 [%] RQD.

The regression curves for the seismic velocities and the RQD and RMR are given in 8.1 in the Appendix. From the discussion in Section 1.6 and Table 1.2 for both, RQD and RMR, a logarithmic correlation with the seismic body-wave velocities is determined as the null hypothesis. The correlation coefficient r did not exceed 0.51 for none of the correlations and was thus far beneath the significance level of 0.95. Even though, the correlation coefficient r is higher for either RQD and RMR with V_s compared to V_p .

For the visualization of interaction patterns between more than two parameters, parallel coordinate plots were used. In this manner, the correlations between the input parameters and the single classes can be visualized at the same time. The polylines that belong to the above selected RQD classes show different mean gradients. For the RMR classes, the medians depict a marked differences in their y-axis intercepts but with similar gradients. Hence, the classes show no distinctive, unique pattern neither for the RQD, nor for the

RMR. It is thus assumed that the data is not linearly separable for either RQD or RMR in the data space (Figure 8.2 to 8.3 in the Appendix). As a result, a simple correlation cannot be determined between seismic velocities and rock quality; however, unknown relationships may reside between the parameters in the data base and the RQD or RMR that are detectable by the self-learning algorithm of the support vector machine.

3.2 Statistical Evaluation of the Glendoe Data Set

The seismic velocities in the Glendoe survey were determined by the use of a 1D-tomography with a 4-m grid spacing between tunnel meter -6478.7 and -6185, while data acquisition of geological and tunnel-driving parameters continued until tunnel meter -6079. As a result, seismic velocities are available for 293.7 m at a 4-m spacing, while the RQD, the RMR and the tunnel-driving parameters were determined for a total of 401 meters. Furthermore, the data gaps mentioned in Chapter 2.2 further reduce the data-point density of the seismic velocities. The entire data set thus discloses a large number of missing points in the seismic data. In comparison, the data-point density of the tunnel-driving parameters is much higher because of the continuous sampling interval of 10 s. The rock-mass quality is influenced by a number of different parameters (cf. Sec. 1.4). As the complexity of the classification task is high, it can be assumed that a large number of samples is needed to identify the unknown underlying patterns in the data (cf. Sec. 1.3). In consequence, to fully exploit the the information contained in the tunnel-driving data on the rock-mass quality, the tunnel-driving parameters are first regarded separately at a 1 m grid spacing. A draw-back of this classification attempt is the discussed ambiguity of the relationship between very high and very low values for TBM parameters and the targets (RQD, RMR) (cf. Sec. 1.6.2). The SVM training is therefore repeated with integrated seismic velocities, leading to a second data set, which is restricted to a 4 m sampling interval by the cell size of the seismic tomogram (cf. Sec. 2.2). The results from the “1-m data set” and the “4-m data set” will be compared to determine the influence of the data set size and the contribution of single parameters on the classification.

The boxplot in Figure 3.3 a clearly shows that 50 % of all samples of the thrust force lie in the range of 4538 to 4975 [kN]. The slight negative skewness (-1.28) and high kurtosis (6.95) in conjunction with the broad scattering of values between 1781 and 6159.8 [kN] suggest a large number of outliers at small values (Tab. 3.2).

	Min	Max	Mean	Median	Std. Dev.	Skew	Kurt	P_{25}	P_{75}
Thr [kN]	1781	6159.8	4708	4866.6	658.4	-1.28	6.95	4538	4975
Tor [kNm]	9.72	1791	709.07	691.64	229.27	0.56	5.33	574	824
Pen [$\frac{mm}{rev.}$]	2.69	148.84	30.04	18.41	29.4	1.83	6.06	10.9	38.8
Spe [$\frac{1}{min}$]	6.59	9.94	9.54	9.58	0.24	-7.94	81.91	9.56	9.61
V_p [$\frac{km}{s}$]	1.15	3.67	2.4	2.45	0.36	0.14	2.84	3.01	3.85
V_s [$\frac{km}{s}$]	1.01	5.43	3.44	3.38	0.62	0.46	3.16	2.18	2.61
RQD	0	100	86	100	27.95	-1.94	5.2	94	100
RMR	28	82	62	67	12.32	-1.03	3.19	57	70

Table 3.2: Basic statistics of the tunnel-driving parameters thrust force (thr), cutter-head torque (tor), penetration rate (pen), and cutter-head speed (dri) as well as for the geotechnical targets at a 1-m sample spacing and the seismic velocities at a 4-m sample spacing.

Similarly, the other tunnel-driving parameters also show broad scattering, a large number of potential outliers and high kurtosis values. Especially the distribution of the cutter-head speed is extremely peaked, expressed by the extreme kurtosis of 81.91 and the narrow box with short whiskers in Fig. 3.3 d. The high negative skewness clearly indicates a wide scattering of outliers for small values. Given this distribution, it is very unlikely that the parameter has explanatory power about the variance of the target parameters. By enlarging the sample interval to 4 m, a reduction of outliers and noise is achieved for the tunnel-driving parameters (cf. Fig. 3.3 and Tab. 8.6 in the Appendix).

The seismic velocities, on the other hand, feature skewness and kurtosis values that indicate normal distribution (Tab. 3.2 and Fig. 3.4). The unusually low minimum value 1.15 [$\frac{km}{s}$] of V_p , as much as all other V_p values $< 1.5[\frac{km}{s}]$ are not correlated to any geological structure and are interpreted as extreme outliers.

Similar as to the Faido Adit, the RQD samples cover the whole range of possible values in the Glendoe Tunnel, with a marked gap in the interval between 29 to 52 [%] RQD. The median at 100 [%] RQD coincides with the 75th percentile P_{75} , which indicates that at least 25 % of all data points are assigned to the largest possible value.

The P_{25} at 94 [%] RQD exceeds the mean value by 8 [%] RQD, which indicates that a large number of values is statistically regarded as outliers. This, however, is attributed to the strong representation of rocks with few to no jointing in the Glendoe Tunnel (c.f. Sec. 2.1). Just as for the Faido Adit, the rock-mass class "excellent" (Deere and Deere, 1988) is regarded separately because of its strong representation in the data set.

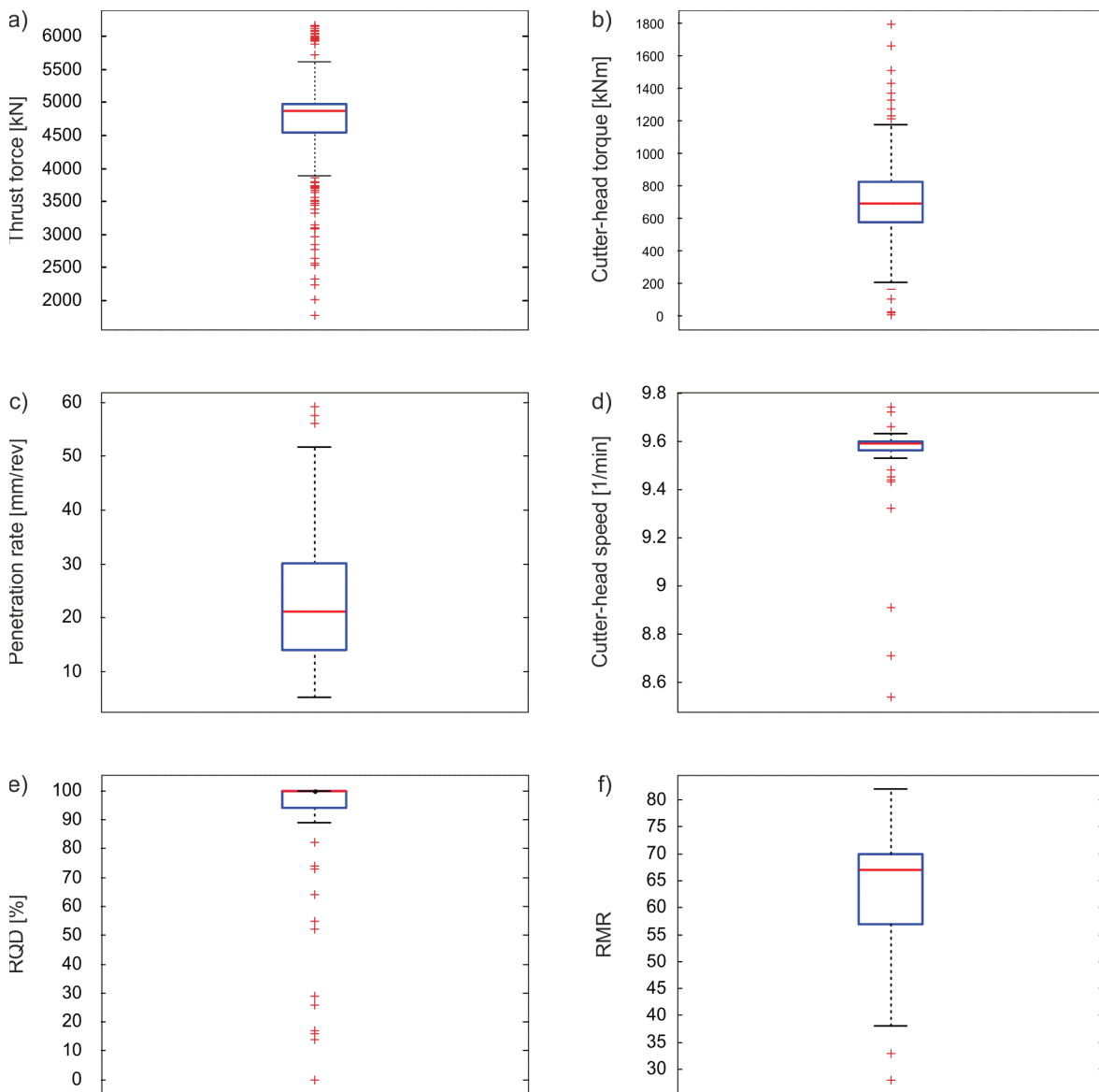


Figure 3.3: Boxplots of the tunnel-driving parameter and the target parameters, RQD and RMR, of the Glendoe Tunnel "1-m data set". The boxplots of the tunnel-driving parameters indicate peaked distributions for (a) the thrust force, (b) the cutter-head torque, (c) the penetration, and (d) an extremely peaked distribution for the cutter-head speed. The RMR (f) is concentrated within the "fair" to "good" classes and the RQD values (e) are peak in the Class "excellent".

Because the remaining data is distributed evenly between the classes "very poor" to "good", a class with solely poor rock-mass quality data is distinguished from the classes with medium rock-mass quality for the SVM approach:

- Class 1: "very poor" to "poor" rock-mass quality described by RQD values from 0 to 50 [%].
- Class 2: "fair" to "good" rock-mass quality described by RQD values from 51 to 90 [%].
- Class 3: "excellent" rock-mass quality described by RQD values from 90 to 100 [%].

This class separation is slightly different than that of the RQD classification in the Faido Adit because of the more unbalanced data distribution at the latter test site.

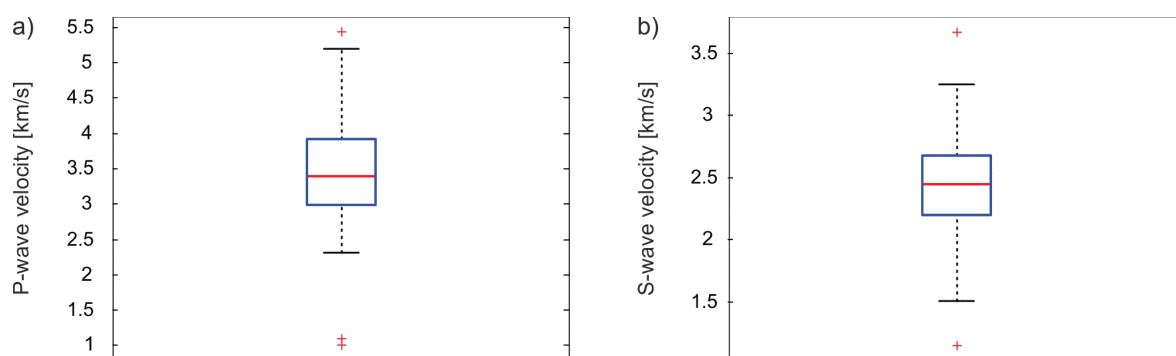


Figure 3.4: Boxplots of the seismic velocities of the Glendoe Tunnel data set. The seismic S- and P-wave velocities in (a) and (b), respectively, are sampled at a 4-m sampling interval according to the 4-m cell size of the 1-D seismic tomogram instead of the 1-m interval depicted for all other parameters in Fig. 3.3.

The RMR shows a similar distribution as in the Faido Adit, with the classes "fair" and "good" being the best represented in the data set. When the extreme classes are absent (Fig. 3.3 f) the distribution shows a nearly normal peakedness and a short negative tail, expressed by a skewness of -1.03 for the RMR (Tab. 3.2). Thus, the definition of classes for the Glendoe Tunnel and Faido Adit data sets are the same, with the class boundary for both test sites being set to $RMR = 60$:

- Class 1: low rock-mass quality, expressed in RMR values from 0 to 60.
- Class 2: high rock-mass quality, expressed in RMR values > 60 .

The correlation matrix in Figure 3.5 a gives an overview on the correlation coefficients r between all tunnel-driving parameters themselves as much as for the RMR and RQD. From the discussion on the correlation of the tunnel-driving parameters in Chapter 1.5, a linear correlation between the thrust force, penetration and cutter-head torque may be expected. The result, however, still suggests little to no linear correlation between the

tunnel-driving parameters with r being < 0.6 . This could be interpreted as a result of the strong peakedness in the distributions described above, which in turn might be caused by low variability in the geology. As expected, the highest correlation coefficient r is achieved between the thrust force and the cutter-head torque, as the torque is directly related to the thrust force. Given the direct relationship between the two parameters, it might be argued that either the thrust force or the cutter-head torque should be eliminated from the data base for the SVM, as no new information is contributed to the classification task; however, preliminary tests with SVM constructions proved to provide more stable results when both parameters were included. This was interpreted as a result of noise reduction.

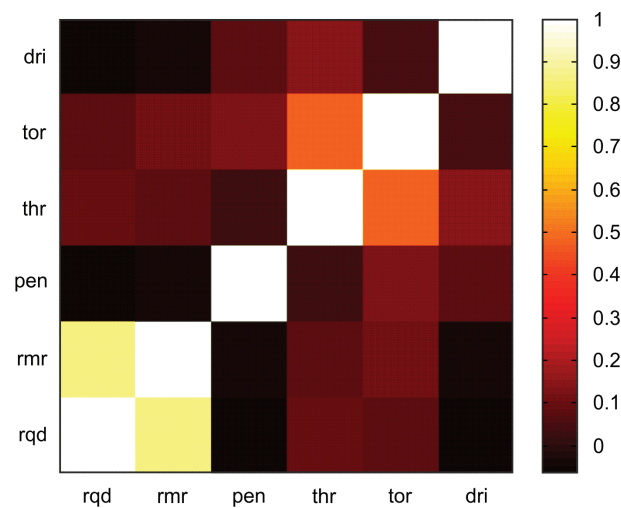


Figure 3.5: Correlation matrix for the Glendoe Tunnel "1-m data set" exhibits the Pearson's correlation coefficient r between each pair of variables. The linear correlations between the tunnel-driving parameters and the rock-mass quality seems generally negligible between the rock-quality, expressed as RQD or RMR, and the penetration (pen), thrust force (thr), cutter-head torque (tor) and cutter-head speed (dri).

The cutter-head speed stays constant for both, the RQD and RMR, though a quality change in the rock conditions should entail a response of the cutter-head speed. This is interpreted to be caused by the regulations done by the machine driver (Sec. 1.5), which aims to keep the cutter-head speed at a predefined high level to maintain a high level of performance of the machine. It is concluded that the parameter has no explanatory power on the variance in the RQD or RMR. Thus, the cutter-head speed is eliminated from the data base for the SVM.

Based on the discussion in Section 1.6, it is assumed that a non-linear relationship persists between the tunnel-driving parameters and the rock-mass quality expressed in RQD or

RMR, respectively. Thus, a non-linear relationship tunnel-driving parameters and the rock-mass quality is set as the null hypothesis. The regression curves in Figure 3.6 illustrate the strong concentration of data points at high RQD values. This restriction of samples to a small subspacedo not lead to a general conclusion about the correlation behavior between tunnel-driving parameters and RQD. The null hypothesis must also be rejected for the RMR because of the strong scattering of samples in Figure 3.7 a-c.

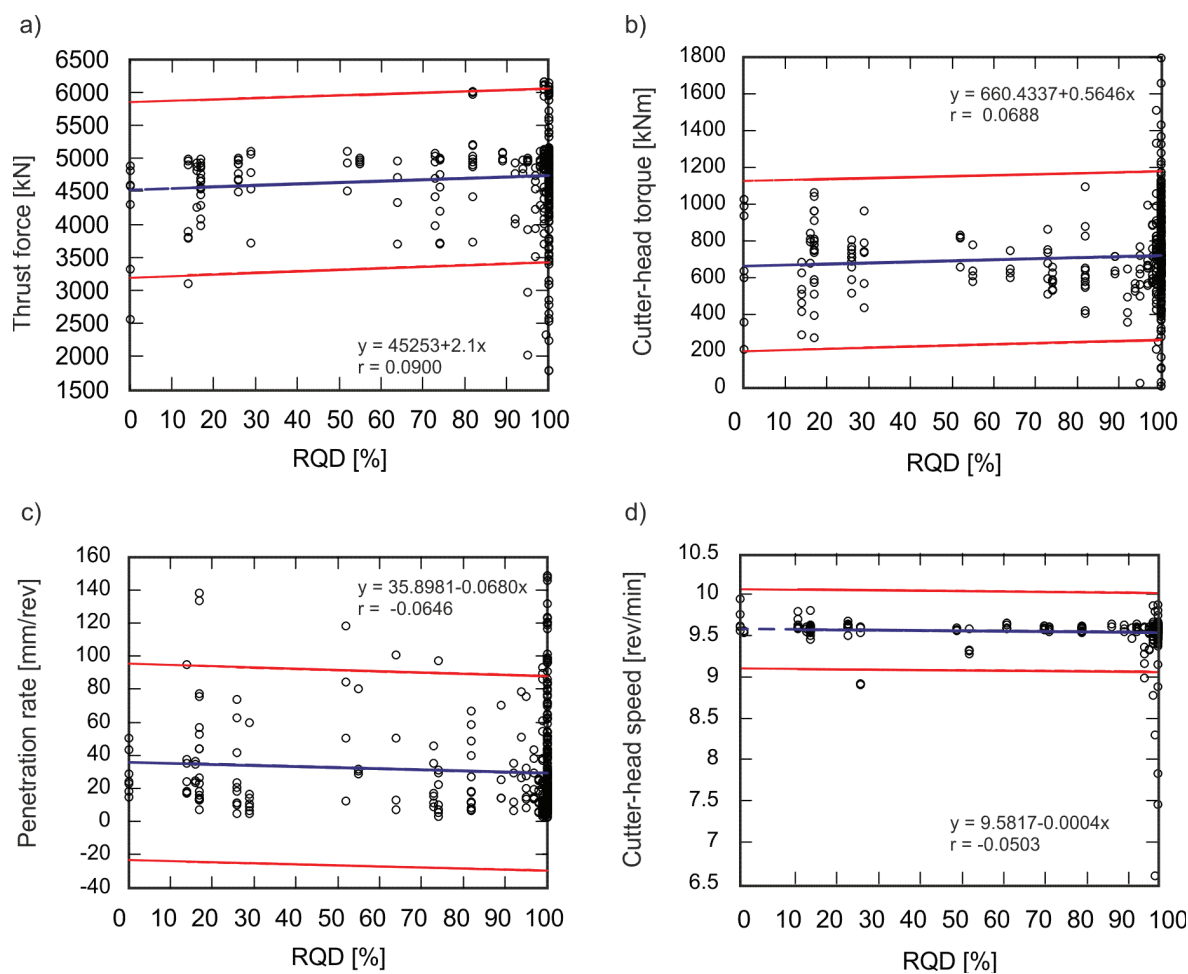


Figure 3.6: Regression curves between tunnel-driving parameters and the RQD from the Glendoe Tunnel data set. The black circles mark single data points, the red dashed lines mark the 95 % confidence bounds, and the blue line is the regression curve. Generally, there is no correlation detectable between the tunnel-driving parameters and the RQD.

In Figure 3.8 the Young’s modulus E_{dyn} is plotted against the RQD and the RMR, respectively. The null hypothesis of a logarithmic correlation between RQD and E_{dyn} is rejected as much as the null hypothesis of a linear correlation between RMR and E_{dyn} . The theoretically determined regression curves for both, RQD and RMR, deviate from the measured curve trends in the gradients and the y-axis intercepts. It is concluded that the relationship established by El-Naqa (1996) cannot be verified. The RQD values

again exceed a 100 [%] RQD and are thus outside the defined range. It can therefore be concluded that the equation set by El-Naqa (1996) does not sufficiently describe the relationship between E_{dyn} and RQD.

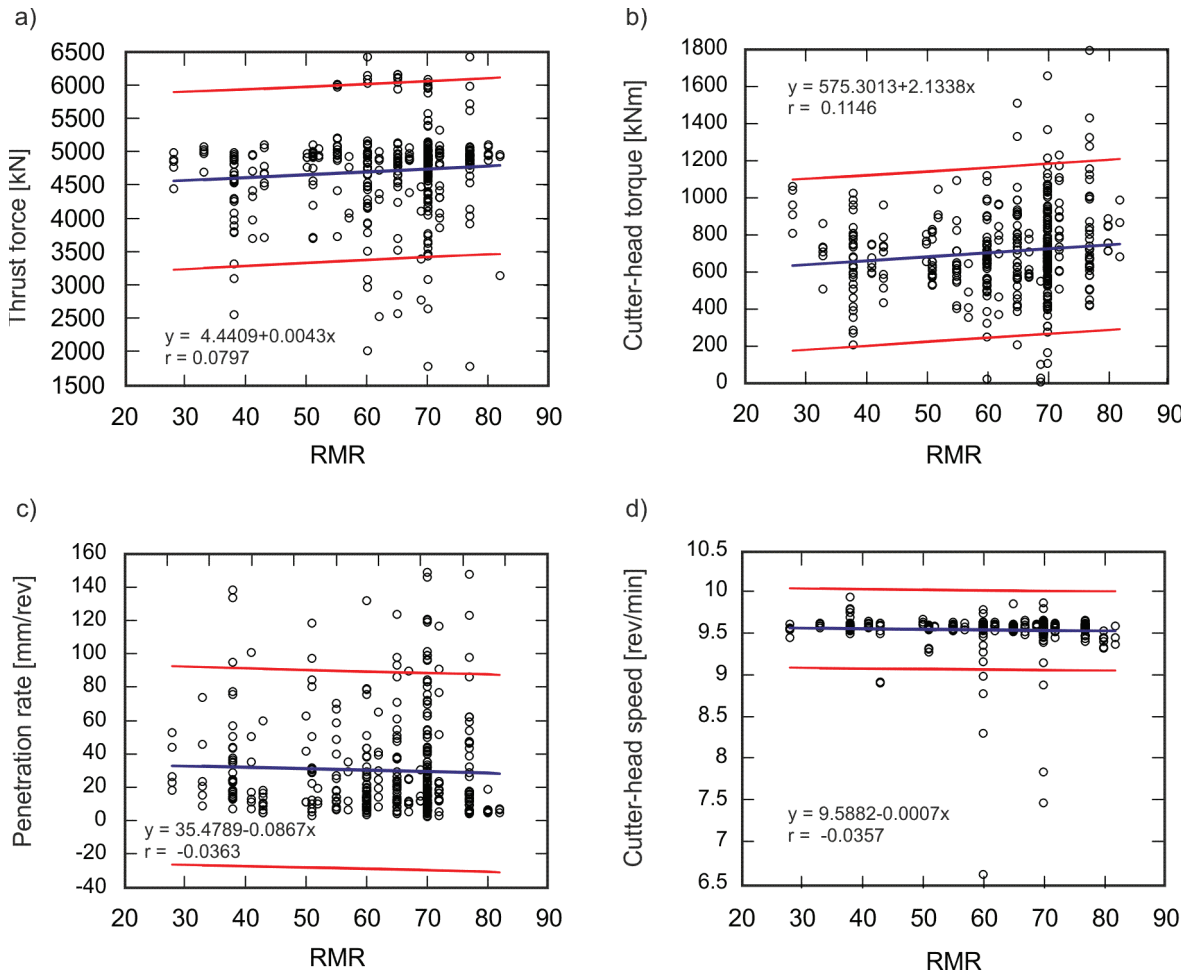


Figure 3.7: Regression curves between tunnel-driving parameters and the RMR from the Glendoe Tunnel data set. The black circles mark single data points, the red dashed lines mark the 95 % confidence bounds, and the blue line is the regression curve. Generally, there is no correlation detectable between the tunnel-driving parameters and the RMR.

Inspection of the parallel coordinate plots revealed that no specific patterns in the feature space could be visually determined for the RQD or the RMR classes (Fig. 8.5 in the Appendix). The extremely peaked distribution of the cutter-head speed is also reflected in the parallel coordinates plots of the RQD and the RMR. In this visualization of dependencies between several parameters, the cutter-head speed bundles all lines into one point, disregarding a few strong outliers (cf. Fig. 8.6 in the Appendix). The parameter was removed from the data set before training of the algorithm to save computational time.

In the parallel coordinate plots of the “4m-data set” 8.5 and 8.6, which include tunnel-

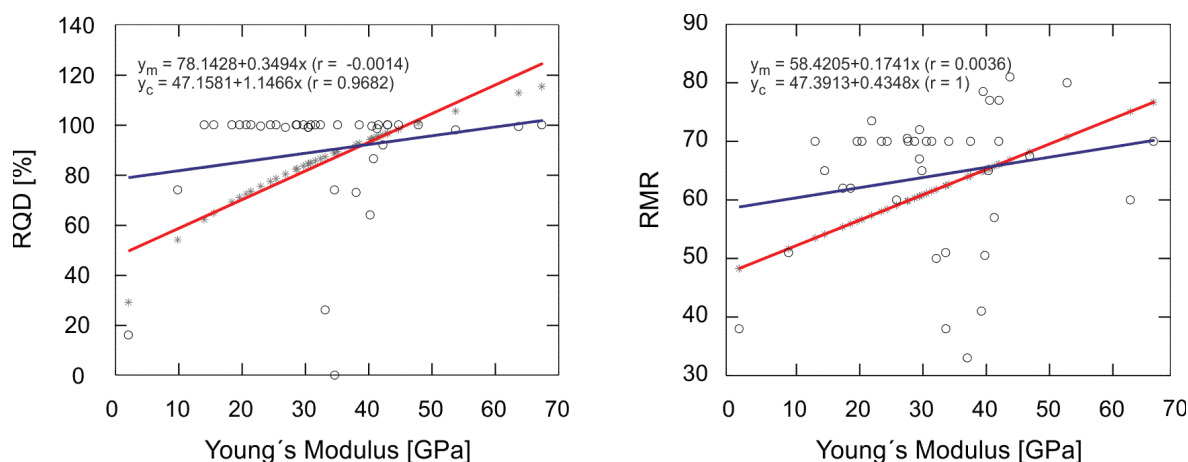


Figure 3.8: Relationship between elastic dynamic modulus E_{dyn} and rock-mass quality descriptive parameters RQD (left) and RMR (right). No correlation was detected during regression of the collected data (regression line y_m in red) and E_{dyn} . The RQD or RMR values calculated using the equations set by El-Naqa (1996) are significantly larger than the measured values though the curve trends (regression line y_c in blue) exhibit similar slopes.

driving parameters as much as seismic velocities, the sparse character of the data base and the high amount of missing values in the seismic data becomes apparent.

3.2.1 Final Remarks

For both target parameters, the majority of the data indicates good rock quality, which was expected from the general geological setting at both test sites. Few data points are realized in the low rock-quality classes. The narrow value range and the concentration of values for high to middle rock-mass quality requires the merging of RQD classes (Deere and Deere, 1988) and RMR classes (Bieniawski, 1989).

Neither linear correlations between the geotechnical parameters nor logarithmic correlations between seismic velocities and rock-mass quality could be verified in the statistical analysis. In Chapter 1.6.1, the theoretical correlations among the parameters involved have been discussed; however, the correlations have often been determined during laboratory studies with only one or two parameters changing at a time. Apart from complex interaction patterns that may not be detected by classical statistical evaluation, the causes for the weak correlation might be:

- the small size of the data sets,
- the over-representation of rocks with high rock-mass quality in the available data sets,

- noise or possible errors during data acquisition.

The lithology along the surveyed tunnel sections did not change significantly, given that jointed, unweathered hard rock was excavated during both surveys. Accordingly, the RMR values vary especially within the Classes “fair” to “good”, while the mean RQD is slightly higher than expected. The restricted size of the available data sets and the limited number of samples for low rock-mass quality present a the major challenge for the automated classification via SVMs.

4 Development of a Support Vector Machine for Rock-Mass Classification

The classification of the rock-mass quality, expressed in RMR or RQD classes, along the Faido Adit and the Glendoe Tunnel by Support Vector Machines (SVM) is based on seismic velocities and tunnel-driving data. The set-up of the seismic surveys was adapted to the specifics of the tunnel construction at each site, resulting in different cell sizes of the tomographies for the Faido and the Glendoe survey and subsequently to unequal resolutions of the datasets. The tunnels were excavated using different tunnel-excavation modes – TBM in the Glendoe Tunnel and drill-and-blast in the Faido Adit– and reinforcement layouts. Because of the different preconditions, a joint interpretation of the datasets would not be valid; however, the SVM approach developed in this chapter should be applicable to all classification tasks in the present study, and also for application to a wider range of future data sets.

The surveyed tunnel sections are relatively short and the rock masses exposed in each tunnel do not include a wide variety, such that there is a tight grouping of rock-mass class and a lack of a range of data falling into each of the classes integral in the RMR or RQD. In Chapter 3 it was shown that in the Faido and Glendoe datasets, two and three classes are distinguished in the RMR and RQD, respectively. Thus, two different classification problems are set:

- (a) a binary classification for the RMR and
- (b) a multi-class classification for the RQD.

It follows that the approach developed in this chapter should be capable to deal with multi-class classification problems, as well as binary classification tasks. Therefore, despite the fact that a binary classification approach would probably suffice for the RMR in this study, the type of SVM and the work flow for its construction are kept constant by usage of a multi-class SVM. This is possible as the multi-class classification approach pursued here is also able to deal with the simpler case of a binary classification. Hence, the consistent handling of data for RQD and RMR classification is ensured.

Taking into account the two different sampling intervals for the Glendoe Tunnel (cf.

Chap. 3) and the aforementioned necessity to evaluate the Glendoe and Faido datasets independently, a total of 6 classification tasks are set that are summarized in Table 4.1.

Survey Area	Resolution [m]	Label	Feature Matrix
Faido	0.5	RQD	V_p, V_s
Faido	0.5	RMR	V_p, V_s
Glendoe	1.0	RQD	pen, thr, tor
Glendoe	1.0	RMR	pen, thr, tor
Glendoe	4.0	RQD	pen, thr, tor, V_p, V_s
Glendoe	4.0	RMR	pen, thr, tor, V_p, V_s

Table 4.1: Overview on the classification tasks for the Faido and Glendoe survey. The classification tasks differ in either target or feature matrix. The parameters appearing in the feature matrix are the penetration rate (pen), the thrust force (thr), the cutter head torque (tor), the P-wave velocity V_p , and the S-wave velocity V_s .

The process of SVM construction is depicted in Figure 4.1. Firstly, training and testing subsets are created from the data base. The following step is the training process, which includes a grid search on the SVM-parameters. Afterwards, a SVM-model is created that contains information on the support vectors and the spatial position of each separating hyperplane between the respective classes. The model is then tested to determine the generalization ability and the model with highest generalization ability is selected as the best model for further predictions.

Feature Selection

Before the actual SVM construction, features in the input space are selected. The focus in feature selection lies on the reduction of the size of the feature matrix, in order to save computational time and to reduce noise in the prediction performance. Features that have a low impact on the explanatory power of the feature matrix are omitted. Tools for feature selection are, e.g., principal component analysis or graphical models. Applied to rock-mass classification, the latter could, e.g., automatically select the tunnel-driving parameters to be included, depending on the mode of excavation. In this study, the parameter selection has been based on the availability of the data (number of seismic features that can be integrated), theoretical considerations (cf. Sec. 1.5) and statistical evaluation (Sec. 3).

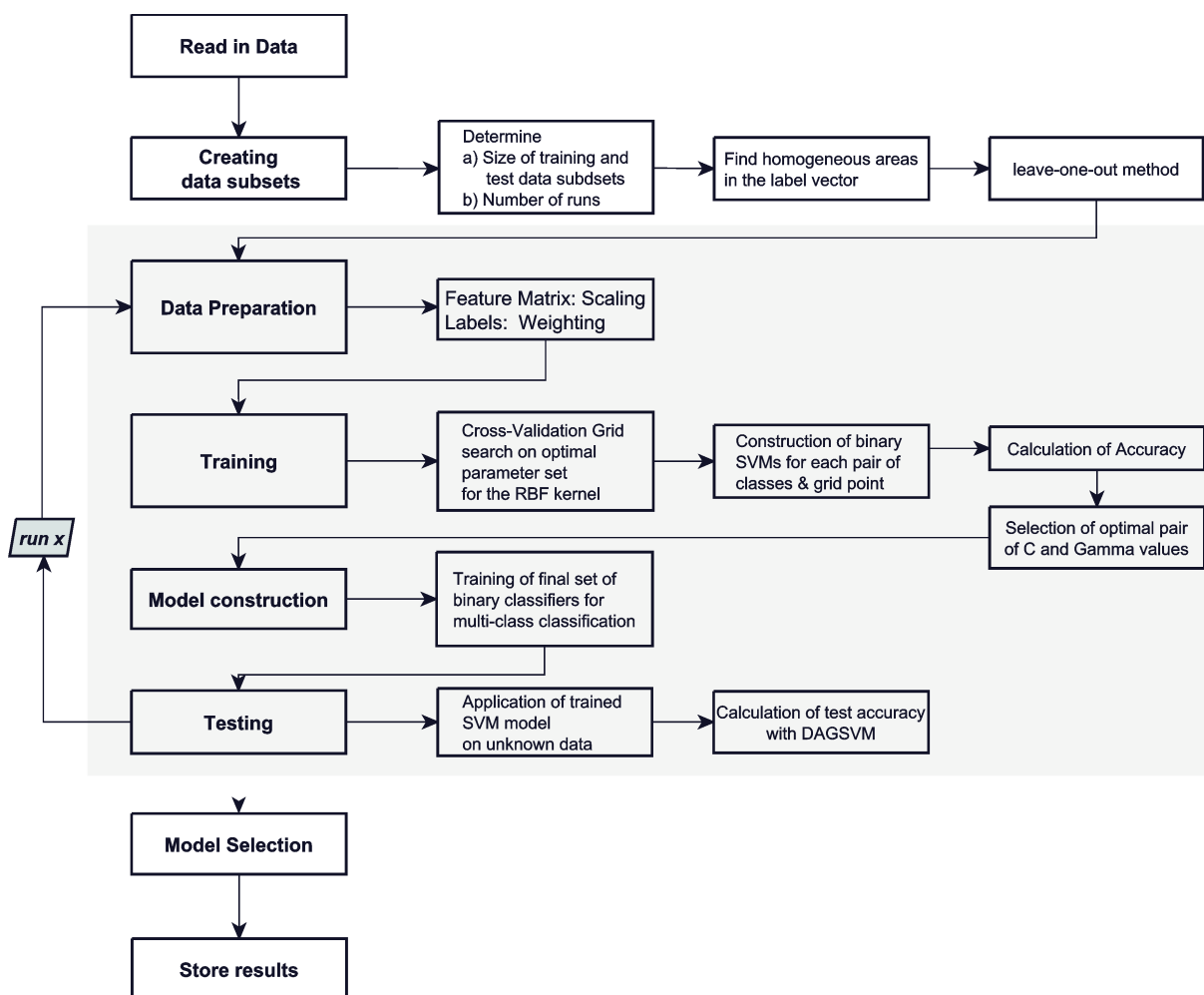


Figure 4.1: Work flow of the implemented multi-class SVM. Firstly, training and testing subsets are created from the data base. In the subsequent step, the training process follows that includes a grid search on the SVM-parameters. The grid search includes a fivefold cross-validation in which the data is mixed randomly to reduce neighboring effects. Then a multi-class SVM is created that contains information on the support vectors and the spatial position of each separating hyperplane between the respective classes. Subsequently, the model is tested to determine its generalization ability. Finally, the model with the highest generalization ability is selected as the best model for further predictions.

Data Subset Generation

In Figure 4.2 the construction of the label vector y and the corresponding feature matrix X is depicted. The rock-mass class at a specific tunnel location is called a label y_i that belongs to the label or target vector y . The values of all measured seismic and tunnel-driving parameters build the feature vector x_i for the label y_i . All feature vectors x_i in a dataset or data subset build the feature matrix X . A feature vector x_i in conjunction with its corresponding label y_i is a data sample.

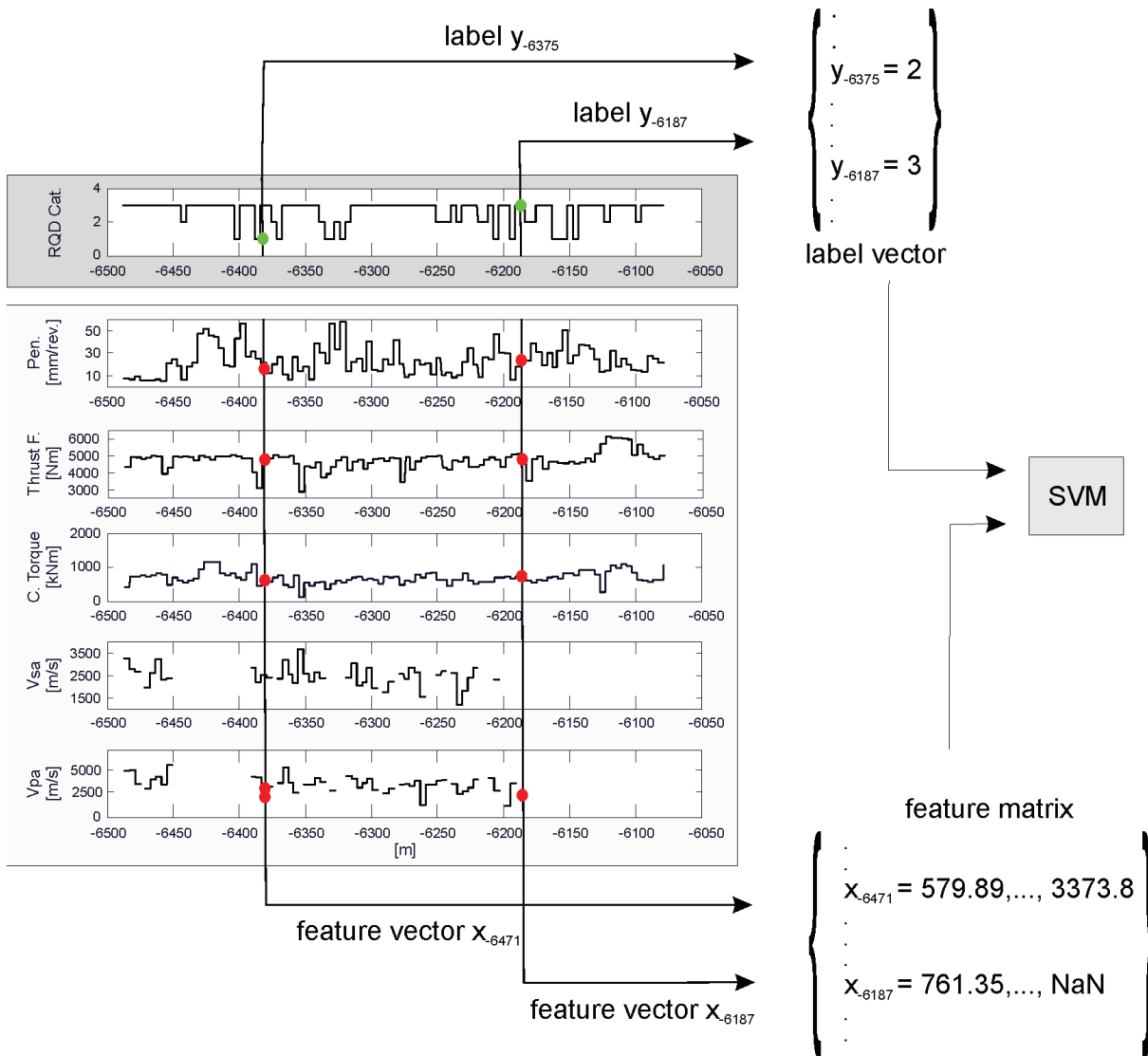


Figure 4.2: Construction of the label vector and the feature matrix from a dataset. The rock-mass class at a specific tunnel location is called label y_i of the label or target vector y . The values of all measured seismic and tunnel-driving parameters built the feature vector x_i for the label y_i . The feature matrix X includes all feature vectors x_i in the dataset. The illustration is based on data sampled at a 4-m interval from the Glendoe project.

In the present study the data base is small so that it should be entirely used for training; however, data points that have been used for training cannot also be used for testing, because the generalization ability cannot be tested by using already known data samples. This problem is overcome by using a kind of cross-validation with the *leave-one-out* technique. Using this technique, the dataset is subdivided into equally sized subsets of data. Apart from one subset S that is used for testing, the data is used for training. A SVM model is created that is independent from the subsequent steps where the part of the data used for testing is shifted to the next data subset S_{+N} and again all other data

samples are used for training. This procedure is then repeated until the whole dataset has been used for testing once (Fig. 4.3 a).

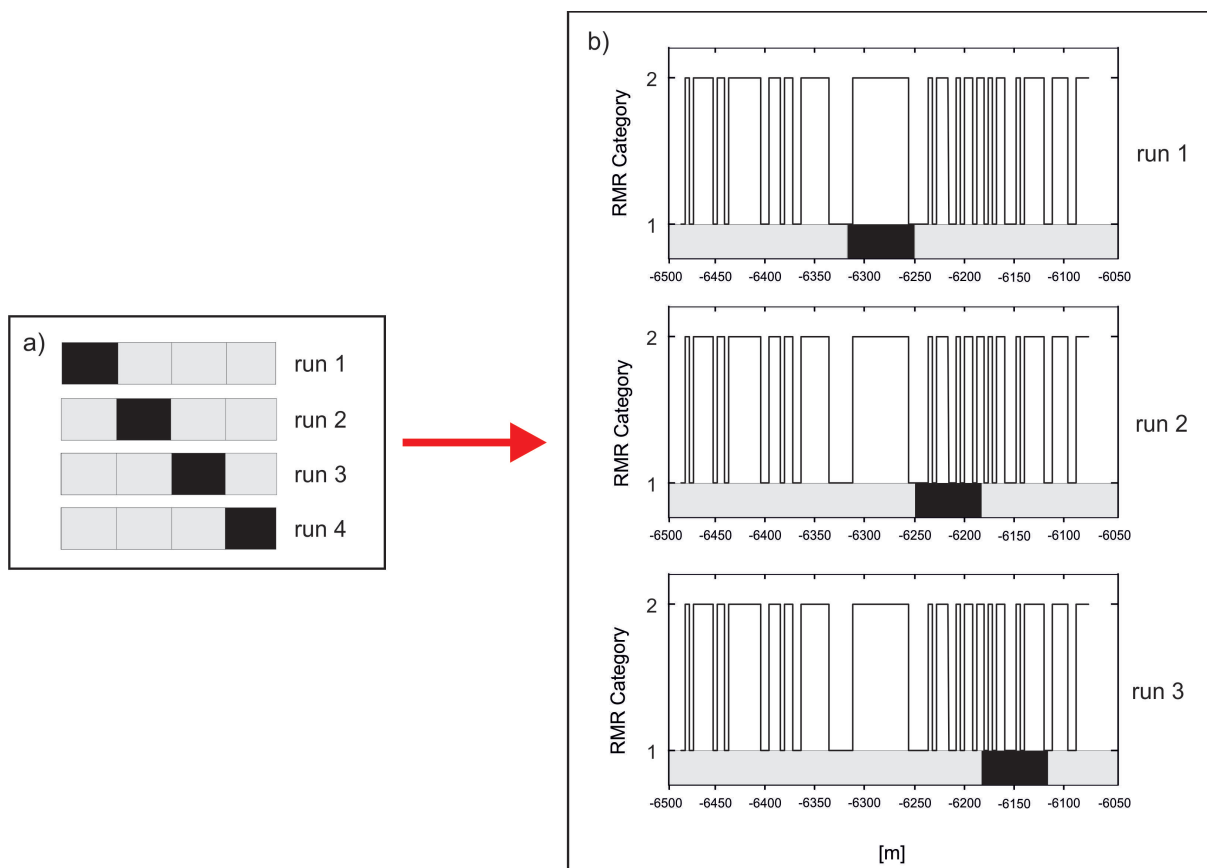


Figure 4.3: Generation of data subsets for training and testing: (a) By using the *leave-one-out* technique, the dataset is subdivided into equally sized subsets of data. One subset (marked black) is used for testing and the rest of the data is used for training (highlighted gray). The method in (b) is a variation of the *leave-one-out* method, where the size of the test dataset depends on the distribution of the rock-mass classes (labels) along the surveyed tunnel section. The test dataset is chosen according to the largest homogeneous label region to avoid overfitting as a consequence of the influence of neighboring values.

The data collection along a tunnel wall is usually continuous, such that the two consecutively collected data points are neighboring values. In Chapter 2, the idea of regionalization of the rock mass along geological cross sections was introduced. Along a tunnel wall, several consecutive data samples can comprise the same label, e.g., the same RMR-class. These data samples thus constitute homogeneous regions that are reflected in the label vector y ; however the independence of the data samples in the feature matrix is required to counteract overfitting of the algorithm. Due to the nature of the datasets available (small size, continuous logging), this dilemma remains.

To reduce the influence of neighboring values, the size of the test dataset can be chosen

according to the largest region that continuously comprises the same labeling (cf. Fig. 4.3b). In doing so, it is guaranteed that at least one region has to be predicted without forming part of the training data. This way, the generalization ability and, subsequently, the predictive performance of the model can be tested. Otherwise, the unvarying "rock block" will be present in the test and training dataset, leading to misconceivably high test results on the prediction performance of the model. The repetition of the process is then in accordance with the *leave-one-out* method, but the number of iterations depends on the size of the longest encountered homogeneous region of the SVM target and consequently on the size of the test dataset. The length of the training and test dataset as well as the number of iterations for SVM construction thus depend upon the distribution and the variance in the labels that are the equivalent to the rock-mass classes here.

After the subsets are generated, the feature matrices for both test and training data are transformed to sparse format to save computational time (Fig. 4.2). The training data is then scaled to [0,1] and the test data is scaled relative to the maximal and minimal values of the training data.

Kernel Selection

In the next step, the SVM is trained by using the kernel-trick that was introduced in Section 1.8. The kernel functions are crucial to the performance of the SVM as they explicitly define the feature space and the capacity of the model. The most common kernel functions are:

- Linear kernel: $K(x_i, x_j) = x_i^T x_j$.
- Polynomial kernel: $K(x_i, x_j) = (\gamma x_i^T x_j + r)^d, \gamma > 0$.
- Gaussian (RBF) kernel: $K(x_i, x_j) = \exp(-\gamma \|x_i - x_j\|^2), \gamma > 0$.
- Sigmoid kernel: $K(x_i, x_j) = \tanh(\gamma x_i^T x_j + r)$.

With, γ , r and d being the kernel parameters (Hsu et al., 2010), x_i is being the feature vector (Fig. 4.2) and y_i the label of the observational point i . For the SVM implementation in this study, the RBF kernel was chosen because:

1. The RBF is able, unlike the linear kernel, to map the feature vectors into a higher dimensional space, so that classifications with non-linear relationships between the class labels and their attributes can be handled. Furthermore, the linear kernel might be regarded as a special case of the RBF kernel (Keerthi and Lin, 2003).
2. In comparison to the polynomial kernel, the RBF kernel needs fewer hyper-parameters (leading to a reduced model complexity) and has fewer numerical difficulties (Hsu

et al., 2010).

3. The RBF matrix is semi-positive, as required, under most conditions, unlike the matrix of the sigmoid kernel (Lin and Lin, 2003). Furthermore, the sigmoid kernel does not usually lead to better results than the RBF kernel.

A case where the application of an RBF-kernel might become difficult is for very large feature spaces combined with a small kernel bandwidth γ . Under these conditions the use of an RBF kernel might lead to overfitting because it is distance-based (Kanevski et al., 2009).

Training

The term "training" describes the process of optimizing the coefficients of the SVM in Equation 1.8.13 by using the quadratic programming problem (QP) in Equations 1.8.8 to 1.8.9. To solve the QP problem, the LIBSVM-package uses the sequential minimal optimization algorithm first proposed by Platt (1998). The quadratic function in Equation 1.8.8 is iteratively minimized by sequentially updating a couple of variables in each iteration Kanevski et al. (2009). Using the RBF kernel, the variables that have to be updated in the QP are:

1. the kernel bandwidth γ from Equation 4 and
2. the trade-off constant C , which regulates the impact of training errors on the margin boundaries and which is also called penalty parameter.

With increasing values of C , both the tolerance against training errors and the margin around the separating hyperplane decrease. In Section 1.8 it was also noted that the selection of the penalty parameter C is arbitrary. This is also true for the kernel bandwidth γ . Subsequently, a parameter grid search over a user defined interval, where the grid-points are defined by pairs of C and γ values, is carried out.

SVMs were originally designed for binary classification, and their application to multi-class problems is still a field of ongoing research (Platt et al., 2000; Wu et al., 2004). Of the multi-class methods the *one-against-one* approach (Knerr et al., 1990) and the *directed acyclic graph SVM* (Platt et al., 2000) have shown the best performance in practical applications (Hsu and Lin, 2002). The two approaches (Fig. 4.5) share the same training algorithm that is also used in this study.

For training, $n(n-1)/2$ binary SVMs are constructed at each grid-point in the parameter grid search, where n is the number of classes in the classification. A voting tournament scheme is established after the "winner-takes-all" principle. This means, the winning class

for the training sample x is usually taken according to the maximum response of the binary classifiers, in consideration of the actual decision function. Uncertainty regions, however, might occur when two classes have been assigned to the same data example during the binary-classifications (Fig. 4.5 b). In this case, the usual way of determining the winner class is to choose the class with the smaller index, making the selection process arbitrary (Huang et al., 2006). The pair of C and γ values that is selected as the best fit to the optimization problem is then applied to the $n(n-1)/2$ binary classifiers developed during model construction. This means, the decision functions of all binary classifiers in the constructed model share the same values of C and γ .

In the LIBSVM-package, the performance of the algorithm during training is calculated for each grid-point in the parameter grid search by calculating the average accuracy over all classes A_t :

$$A_t = \frac{1}{\left(\frac{T_c}{N_x}\right)} \cdot 100, \quad (4.0.1)$$

with T_c being the sum of correctly classified labels over all classes and N_x being the number of all feature vectors in the training data set. This calculation of the SVM performance does not take into account the class size. Therefore, classes which are strongly represented in the training data can lead to falsely high training accuracies. The binary classifications that are carried out for each pair of classes often lead to differently well defined class boundaries, especially when classes including few data points are present. As a result, the finally constructed SVM may show a high total accuracy T_c but rarely classifies the labels of small classes correctly; however, the selection of the best fit SVM is based on the average accuracy L_c . Thus, the test labels are also assigned to the largest class. As a result, the average accuracy L_c can be relatively high while the generalization ability is extremely low because the smaller or less well defined classes are omitted. To avoid this behavior a new calculation of the model accuracy, which takes into account the weighting of the classes, has been programmed during this study and is calculated by:

$$A_w = \frac{1}{n} \cdot \left(\left(\frac{T_{A_{c1}}}{N_{c1}}\right) + \left(\frac{T_{A_{c2}}}{N_{c2}}\right) + \dots + \left(\frac{T_{A_{cn}}}{N_{cn}}\right) \right) \cdot 100, \quad (4.0.2)$$

with A_w being the weighted averaged accuracy over all classes, $T_{A_{ci}}$ being the number of correctly classified labels in each single class ($i = 1, 2, \dots, n$) and N_{ci} is the number of feature vectors in each single class. It is especially important to use A_w if only small datasets are available, as is the case in the present study. Moreover, the training function now also provides the percentage of correctly classified feature vectors with respect to the number of feature vectors in each class $\left(\frac{L_{ci}}{A_{ci}}\right) \cdot 100$.

To achieve a stable result, a five-fold cross-validation (Fig. 4.1) is carried out for each point in the grid search. During the cross-validation, the data is randomly mixed to counteract neighboring effects. The selection the number of cross-validation iterations is arbitrary and has been set to five here after several test runs showed that increasing the number of iterations further did not lead to better results.

The generalization ability, or performance of the model, is influenced by the two parameters C and γ in the following way:

1. The **higher** γ and the **smaller** C , the greater the tendency to **underfit**. The stronger the tendency to underfit, the simpler the model. In the case of severe underfitting, the entire data space is assigned to the majority class.
2. The **smaller** γ and the **higher** C , the stronger the tendency to **overfit**. The overfitting is additionally characterized by high training accuracies, a high number of SVs and poor generalization ability, leading to low prediction accuracies in the test phase. In the case of severe overfitting the model creates small regions around the training examples of the minority class, while the rest of the data space is classified as the majority class. Large values of C constrain the weights α less and allow the model to follow the data samples exactly and even fit the noise and outliers if they exist, expressing a believe in the quality of data.

Thus, an optimal classification is achieved with intermediate values of the parameters C and γ (Fig. 4.4); however, there are no definite criteria as to when the parameters are to be regarded as "high" , "intermediate" or "low" (Kanevski et al., 2009). Moreover, numerical problems might arise for large or very small C and γ values (Keerthi and Lin, 2003).

The training time is strongly influenced by the cross-validation process. This dependence cannot be described analytically but the training time in a Gaussian RBF kernel generally increases for increasing C and γ values. To save computational time, a rough grid search was carried out first. As an example: For the RMR classification of the Glendoe Tunnel dataset at 1-m sample spacing, which contains exclusively tunnel-driving parameters in the feature matrix, a parameter search in the range of $\log(C) = [-5:1:15]$ and $\log(\gamma) = [-15:1:5]$ takes about 4h ,where the first and the last value detail the first and the last value in the search space, respectively. The second value denotes the incremental step size. In comparison, the cross validation for a grid in the range $\log(C) = [-10:1:20]$ and $\log(\gamma) = [-10:1:20]$ takes around 12h.

In the next step the whole training set is trained with the best found set of C and γ values and a final model for the present run is generated (Fig. 4.1). The SVM model includes the decision values and the location of the support vectors for each class. Therefore, the

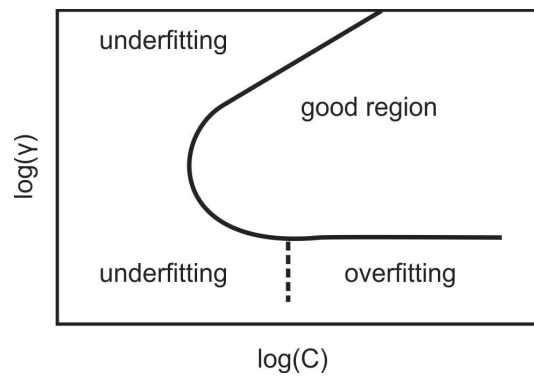


Figure 4.4: The selection of values for penalty parameter C and kernel bandwidth γ influences the model complexity and can lead underfitting, overfitting or good model generalization ability. To find the best fit parameter set, a 2-D grid is constructed and the binary classifiers are trained on each pair of C and γ at uniform incremental steps in this grid. This grid search is the step in model construction that takes most computational time. Comparatively large γ values lead to underfitting, while large C values, in comparison to γ , lead to overfitting (Source: Keerthi and Lin, 2003).

spatial location of the hyperplane can be obtained from the model.

Testing

The testing is the last part of the process, where the ability of generalization of the constructed model to new data points is checked. It was mentioned above that the *one-against-one* approach is implemented in the LIBSVM-package by default and that the *directed acyclic graph* of the DAGSVM showed similar results in practical applications (Hsu and Lin, 2002); however, the DAGSVM has one major advantage over the *one-against-one* approach during testing because it avoids uncertainty regions during prediction by using a *rooted binary directed acyclic graph*, while the *one-against-one* approach uses the same scheme as described for the training process. The *rooted binary directed acyclic graph* exhibits $n(n-1)/2$ internal nodes and leaf nodes (Platt et al., 2000) (Fig. 4.5), each node standing for a binary SVM. Given a test sample x , starting at the root node, the binary decision function is evaluated. In accordance with the winning class of the binary SVM, the next binary classification to be evaluated is chosen.

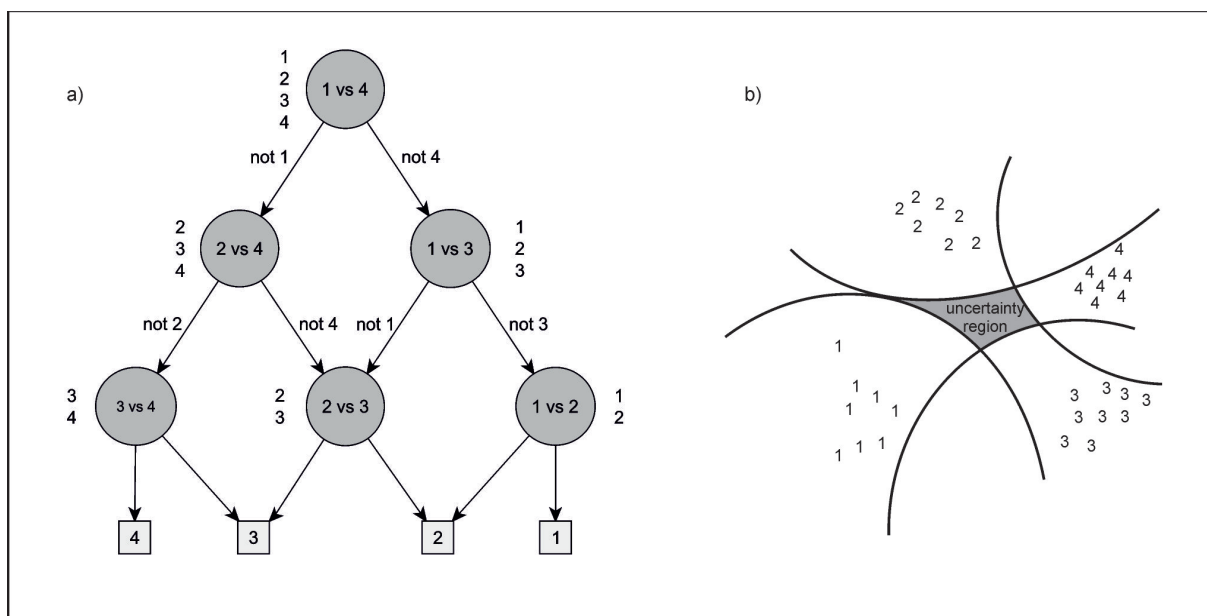


Figure 4.5: Comparison of the DAGSVM to the *one-against-one* SVM method. (a) Sketch of a directed acyclic graph from the DAGSVM to find the most fitting class out of four classes. The numbers beside the nodes stand for the classes which have yet to be decided on. (b) In the *one-against-one* approach, a binary classifier (SVM) is constructed for each pair of classes. A voting scheme is constructed to combine all the pairs of classifiers. In the region highlighted gray, each class has 2 wins and the final decision has to be resolved choosing the class with merely the smaller index (Figure modified after (a) Platt et al., 2000 and (b) Kanevski et al., 2009).

Subsequently, a path is run through until the leaf node indicating the actual predicted class is reached. This way, no uncertainty regions occur because no double assignment can take place. Another advantage of using the DAGSVM approach is that some analysis of generalization can be established. Such theoretical results are not established for similar binary multi-class approaches like the *one-against-one*. Just as for the training accuracy, the calculation of the overall prediction accuracy was reprogrammed according to Equation 4.0.2.

4.1 Programming Environment

The code for the presented SVM was programmed using algorithms from the LIBSVM-library (Chang and Lin, 2010) in the version 2.89-3. This library is one of the most widely used for SVM applications (Scheidler, 2008; Welle, 2009; Yao et al., 2008; Kanevski et al., 2009) and freely available on the Internet. It can be integrated into applications under C, Java, Matlab, R and several other coding languages. Here, the interactive programming environment Matlab was used. It allows for the development of programs and algorithms

for the analysis and visualization of data and numerical calculations. The code can be used in the programming environment as algorithms and programs or it can be compiled in stand-alone programs or integrated into applications (e.g. Excel Add-Ins). There are also various toolboxes, with libraries of custom-designed functions, that expand the programming environment. A major advantage is, that the code written in Matlab can be easily translated to C/C++, FORTRAN, Java and other programming environments. The LIBSVM-code is also programmed in C/C++ and afterwards translated to Matlab. The described re-programming of the calculation for the training accuracy was therefore done in the C-code of the training function. Thus, the code used here can be easily implemented into an interpretation system for seismic data and tunnel driving data.

5 Results of Rock-Mass Classification using SVMs

The data set of the Faido Adit (FA) is composed of 897 data samples at a 0.5 m sample spacing. The samples are distributed along seven seismic profiles that are separated from each other by a few tens to hundreds of meters. The feature matrix, for both the RQD and the RMR classification task in the Faido Adit, comprises the normalized seismic S- and P-wave velocities.

The data sets for the RMR and RQD classifications along the seismic profile in the Glendoe Tunnel (GT) between -6490 to -6040 m consist of 401 or 103 samples at either a 1 m or 4 m sampling interval, respectively. The 1-m data set includes exclusively tunnel-driving parameters in the feature matrix, while results from seismic velocity measurements add to the feature matrix in the 4-m data set. The classification tasks thus differ from each other either in the target or the sampling interval, as well as in the size of the feature matrix.

From the general remarks on over- and underfitting in Chapter 4, it follows that a selection of intermediate values for the parameters C and γ is desirable in order to achieve an optimal classification result; however, there are no definite criteria as to when the parameters are to be regarded as "high", "intermediate", or "low". Discussions in literature are usually about "sufficiently" large or small values (e.g., Kanevski et al., 2009 or Keerthi and Lin, 2003). To determine the search space for the grid search on penalty parameter C and kernel bandwidth γ , values from literature were taken into account, as well as examples from the LIBSVM-webpage. The values indicate that the range in a normal search space does not exceed values of $\log(C)$ between -5 to 15 and of $\log(\gamma)$ between -15 to 5. To test the adequacy of this grid size, several test runs with wider and smaller grids at different incremental steps were carried out on the available data sets. The results showed that the above mentioned grid size is sufficiently large and no better classification results are to be expected for a wider search. The grid search is thus carried out in the interval $\log(C) = [-5:1:15]$ and $\log(\gamma) = [-5:1:15]$, where the first and the last value detail the first and the last value in the search space, respectively. The second value denotes the incremental step size.

The share of each class on the total amount of training or test labels varies between the data subsets generated in preparation for the SVM construction (cf. Chap. 4). Of those, only the training subset that provided best training results and the corresponding test

subset of each classification task are detailed in Table 5.1 for the FA and in Table 5.3 for the GT.

5.1 RQD Prediction on the Faido Adit Data Set

For the RQD classification in the Faido Adit (FA-RQD), there are 376 training data points and 521 test data points (Tab. 5.1). Thus, the test data set is larger than the training data set, which results from the homogeneity of the rock-mass quality over large distances of the tunnel alignment.

The weighted training accuracy A_w is 85 %, which suggests a good overall classification result (Tab. 5.2). In comparison to Classes 2 and 3 that comprise 146 and 176 samples, respectively, Class 1 is slightly underrepresented with 54 samples. Class 1, however, achieves an extremely high training accuracy of 96 % . For Class 2 and Class 3, classification results of 70 % and 90 % training accuracy, respectively, are achieved. The weighted training accuracy A_w is used to determine the penalty parameter C and kernel bandwidth γ for the final construction of the binary classifiers for the multi-class classification by automatically selecting the smallest parameter set C/γ achieving the highest A_w (Fig. 5.1).

Notation	Unit	RQD	RMR
Interval	[m]	0.5	0.5
N_x	[No.]	376	609
N_{C1}	[No.]	54	298
N_{C2}	[No.]	146	311
N_{C3}	[No.]	176	-
P_x	[No.]	521	288
P_{C1}	[No.]	4	169
P_{C2}	[No.]	4	119
P_{C3}	[No.]	513	-

Table 5.1: Description of the training and test data set for the RQD and RMR classification tasks in the Faido Adit, respectively. The number of feature vectors in the training set is specified as N_x , the number of feature vectors in each class as N_{C1-3} , the number of feature vectors in the test set is P_x and the number of feature vectors of each single class in the test set are named P_{C1-3} .

Notation	Unit	RQD	RMR
Interval	[m]	0.5	0.5
$\log(C)$		14	15
$\log(\gamma)$		-15	-15
A_w	[%]	85	76
T_{AC1}	[%]	96	70
T_{AC2}	[%]	70	81
T_{AC3}	[%]	90	-
s	[%]	80	74
s_{C1}	[%]	100	76
s_{C2}	[%]	78	72
s_{C3}	[%]	75	-
P_w	[%]	74	70
P_{AC1}	[%]	0	97
P_{AC2}	[%]	100	43
P_{AC3}	[%]	73	-

Table 5.2: Details on the training and test results of the RQD and RMR classification tasks in the Faïdo Adit. The notation includes the logarithm of the kernel bandwidth $\log(\gamma)$, the logarithm of the penalty parameter $\log(C)$, the weighted averaged training accuracy A_w , the number of correctly classified labels in each respective class T_{AC1-3} , the number of support vectors for all classes s and for each class separately s_{C1-3} . The weighted average prediction accuracy is denominated P_w and the prediction accuracy of each single class is listed as P_{AC1-3} .

All binary classifiers are constructed with the same set of parameters by anewed training. In the case that classifiers would be trained with different parameter sets, they would not map to the same feature space (cf. Sec. 1.8) and could therefore not be compared. The binary classifiers are stored in the model, which is then tested on the corresponding test data subset. Information on the generalization ability of the model is obtained by considering the number and distribution of support vectors of each class and the complexity of the optimal hyperplane H . In conjunction with the prediction performance tested on the test data, the model performance can be evaluated.

The weighted training accuracy A_w increases steadily with increasing penalty parameter C , for fixed values of the kernel bandwidth γ (Fig. 5.1), which suggests that an optimal solution is not found. The latter provides knowledge on the prediction performance, and thus, on the generalization ability of the model. The grid-search does not show the expected "good region" from Figure 4.4 in Chapter 4 even at test runs with larger C or larger γ . The grid-search result thus provides extreme values of $\log(C) = 14$ and $\log(\gamma) = -15$ (Fig. 5.1 and Tab. 5.2). It should be noted that the optimal set of parameters C and γ is not only dependent on the weighted training accuracy A_w , but is also influenced by the model

complexity and the prediction result. The automated selection of a parameter set C/γ has been carried out by first evaluating the weighted training accuracy A_w during the grid-search over all created subsets. If the weighted training accuracy A_w increases, the weighted prediction accuracy P_w on the corresponding test data set is determined and in case that P_w also increases, the parameter set C/γ is stored. Thus, the weighted prediction accuracy P_w is regarded only if an increase in the weighted training accuracy A_w has been measured previously. To check the validity of this approach, more balanced parameter sets (e.g., $\log(C)/\log(\gamma) = (4, 0)$) were selected at the expense of the weighted training accuracy A_w ; however, none of these tests lead to better prediction performance or lower model complexity. In contrast, the constructed model and the prediction performance are exactly the same as before. This was not expected, as the selection of the optimal parameter set C/γ is supposed to have great influence on the generalization ability of the model.

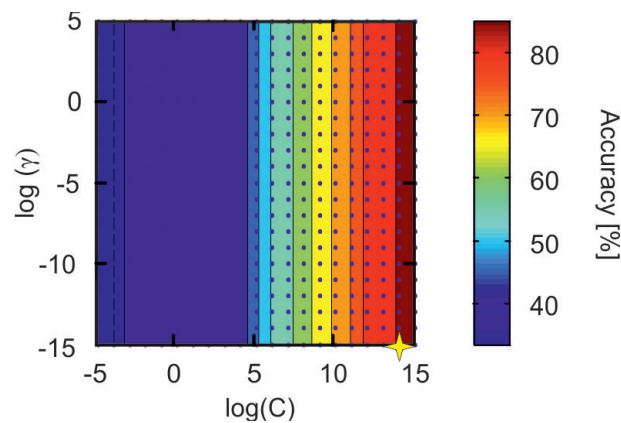


Figure 5.1: Results from the grid search on C and γ for the RQD classification based on the data set of the Faido Adit. The weighted training accuracy A_w increases steadily with increasing penalty parameter C , but remains constant for the kernel bandwidth γ . The parameter set C/γ with the smallest values for the highest achieved accuracy is automatically selected as best-fit parameter set for model construction (yellow star).

In Table 5.2 the number of support vectors s_i in each class is detailed together with the percentage of support vectors with respect to the entire size of the respective class. Between 75 %, for Class 3, and 100 %, for Class 1, of the training data was used as support vectors. These are extremely high values.

In the test data set, Classes 1 and 2 are underrepresented because they are only composed of 4 samples each, in comparison to the 513 test samples that comprise Class 3 (Tab. 5.2). The best fit model construction was carried out in the first run, which uses the largest homogeneous label area as the test data set (Fig. 5.2). This explains the overwhelming representation of Class 3 in the test data. While none of the Class 1 data samples was

correctly predicted, Class 2 reached 100 % and Class 3 achieved 73 % of correctly predicted data samples (Tab. 5.2).

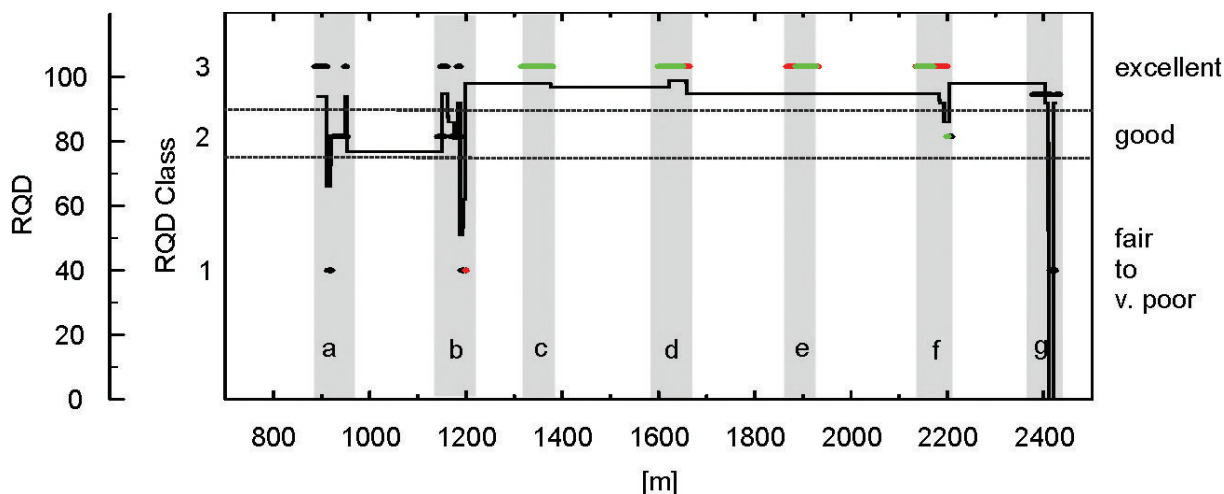


Figure 5.2: Spatial distribution of training and correctly or incorrectly classified test samples in the RQD classification along the tunnel alignment of the Faido Adit. The seven seismic profiles are highlighted as gray bars, the exact measured RQD is shown as a black line and the training samples are tagged as black circles. The test samples are tagged as either correctly (green dots) or incorrectly (red dots) predicted labels.

To get an insight on the model complexity, the distribution of the support vectors from two classes are highlighted in Figure 5.3. The optimal hyperplane H cannot be visualized as such but to give an insight in the model complexity it is sufficient to determine the decision boundary B_{C_i} between two classes in the input space. The optimal hyperplane H is defined as a decision boundary in the higher dimensional feature space. The decision boundary is calculated by using the euclidean norm of the support vectors to the grid points of an equidistant 2-D grid in the input space. Subsequently, the corresponding class label is allocated to this grid point. For the RQD classification discussed here, the model complexity is rather low, because the areas assigned to the classes stretch out over large connected parts of the space. Well defined areas for the class boundaries Class 1 vs. Class 2 (C_1-C_2), Class 1 vs. Class 3 (C_1-C_3) and Class 2 vs. Class 3 (C_2-C_3) are depicted in Figures 5.3 a-c, particularly in the upper right-hand sides.

For the definition of the optimal decision boundary $B_{C_1-C_2}$ of the binary classification task C_1-C_2 in Figure 5.3 a, a large number of densely packed support vectors are necessary above and below Point 1 to define $B_{C_1-C_2}$. Moreover, the support vectors of the opposing classes, indicated by black circles for support vectors of Class 1 and green circles for those of Class 2, are situated at an extremely short distance, so that the margin becomes extremely small in this subspace. At Point 2 in Figure 5.3 b, a segment of the optimal decision boundary $B_{C_1-C_3}$ is not sufficiently defined by support vectors. The predictability

of samples from the test data set situated in this subspace would be low. Figure 5.3 b at Point 3 and in Figure 5.3 c at Point 4 illustrate two areas with strong accumulation of support vectors. These support vectors are composed of either Classes 1 and 3 (Fig. 5.3 b) or Classes 2 and 3 (Fig. 5.3 c) for B_{C1-C3} and B_{C2-C3} , respectively. It can be assumed that in these areas strong noise blurs the class boundaries. For better understanding, the reader should remember that the support vectors are feature vectors of a specific class, and that not all feature vectors are necessarily support vectors. The values of the parameters contained in the feature vectors can determine the location of the feature vector in the data space and in the feature space (cf. Fig. 1.3 in Sec. 1.8 and Fig. 4.2 in Chap. 4). In case a parameter is especially noisy, or patterns in the feature matrix of different classes are similar, more support vectors are needed to define optimal decision boundary B . As B is mapped to a lower dimension, the support vectors may appear to lie within the class area (e.g., Point 5 in Fig. 5.3), rather than at the edges; however, the scope here is to determine the model complexity and to elaborate on the quality of the definition of the class boundaries.

The model complexity is relatively simple, even though the number of support vectors is high and the penalty parameter C is large in comparison to the kernel bandwidth γ . A large number of support vectors and large C values are indicators of overfitting. In the case of overfitting, the model complexity increases because the model is strongly fitted to the data. The prediction performances of Classes 2 and 3 are high. As a result, it can be assumed that a RQD classification based on seismic velocities is generally possible; however, the generalization ability on Class 1 is low. In fact, the small Class 1 was completely assigned to the large Class 3. Note that the decision boundary between Classes 1 and 3 is partially, imprecisely defined. Moreover, the Class 1 feature vectors in the training data were completely used as support vectors for this class. It is, therefore, obvious that the binary classifier between Classes 1 and 3 did not generalize well. This might have been expected instead for neighboring classes like RQD Classes 1 and 2 that express very poor to fair rock-mass quality and good rock-mass quality, respectively. The interrelationship of the discontinuity spacing and, consequently, the RQD with the seismic velocities is acknowledged in literature (e.g., Deere and Deere, 1988). Additionally, the distinction between Classes 2 and 3 is feasible. Therefore, it may be speculated here that either the size of Class 1 is crucial or that the samples labeled as Class 1 do not contain combinations of features that are specific to this class. Class 1 contains the widest range of values between 0-75 [%] RQD and, moreover, the geotechnically most significant low rock-mass quality data. In contrast to the rock in Class 3 that exhibits few discontinuities, the Class 1 rock contains discontinuities of various kinds and conditions. It might be interpreted that the resulting variability in the data reduces the ability of the algorithm to generalize rules

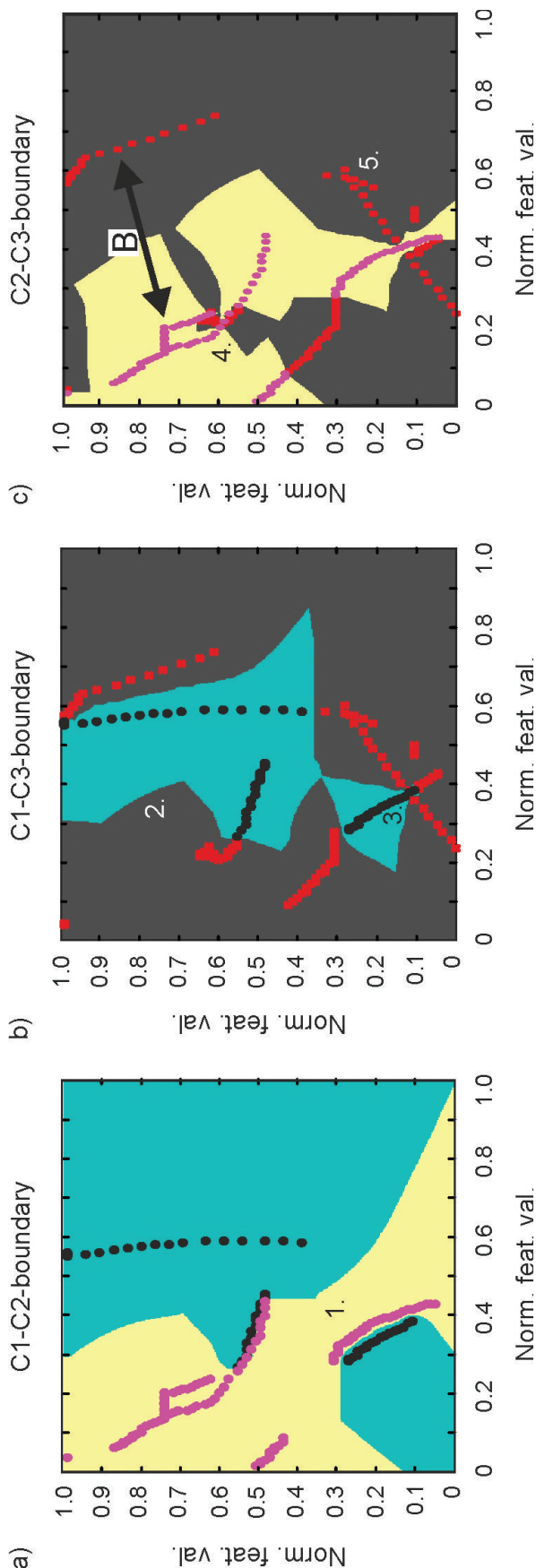


Figure 5.3: 2-D plots of the binary classifiers in the RQD multi-class classification based on the Faido Adit data set. The separating decision boundary is visualized in 2-D by calculating the euclidean norm of the support vectors in reference to the grid points of an equidistant 2-D grid over the normalized input space and by allocating the class label of the nearest support vector to the grid point in question. Class 1 is highlighted green and its support vectors are depicted as black circles, the support vectors of Class 2 (yellow area) are shown as purple circles and the gray areas are assigned to Class 3, whose support vectors are depicted as red crosses. (a) B_{C1-C2} a large number of densely packed support vectors are necessary above and below Point 1 to define B_{C1-C2} . (b) At Point 2, a segment of the optimal decision boundary B_{C1-C3} is not sufficiently defined by support vectors and Point 3 and (c) Point 4 illustrate two areas with strong accumulation of support vectors. The position of the optimal decision boundary B is exemplified in (c).

from the data further in addition to the small class size.

5.2 RMR Prediction on the Faido Adit Data Set

With 609 samples, the training data set of the RMR classification on the Faido Adit data set (FA-RMR) is significantly larger than that of the FA-RQD classification. Class 1 contains 298 data samples of low rock-mass quality with $RMR\ values \leq 60$ and is thus in balanced with Class 2, which contains 311 samples of high rock-mass quality expressed in $RMR\ values > 60$ (Tab. 5.3). The weighted training accuracy A_w achieves an acceptable value of 76 % during the grid-search; however, A_w increases steadily with increasing penalty parameter C until $\log(C) = 12$, at which point it then decreases slightly until it shows an increase of a few percent in A_w at $\log(C) = 15$. Changing the kernel bandwidth γ does not influence the result at all. The accuracies of the single classes are slightly higher for Class 2 with 81 % in comparison to Class 1, which has 70 % correctly classified feature vectors (Tab. 5.2). Equal to the RQD classification task, the automatically stored parameter set C/γ exhibits extreme values, with C being much larger than γ ($\log(C) = 15$ and $\log(\gamma) = -15$; Fig. 5.4). Again, test runs for verification of the parameter selection process were carried out but again the model construction was not affected. As a result, it is assumed that the model construction and the prediction performance are not influenced at all by the training result or the parameter selection.

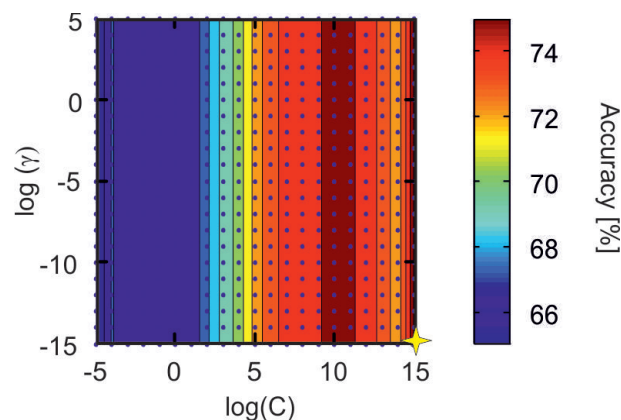


Figure 5.4: Results from the grid search on C and γ for the RMR classification based on the Faido Adit data set. The weighted training accuracy A_w increases with increasing penalty parameter C but is constant for increasing kernel bandwidth γ . The parameter set C/γ with the smallest values for the highest achieved accuracy is automatically selected as best-fit parameter set for model construction (yellow star).

For both classes, around $\frac{2}{3}$ of the training samples were used as support vectors (Tab. 5.2). The larger the number of support vectors, the more complex the model becomes.

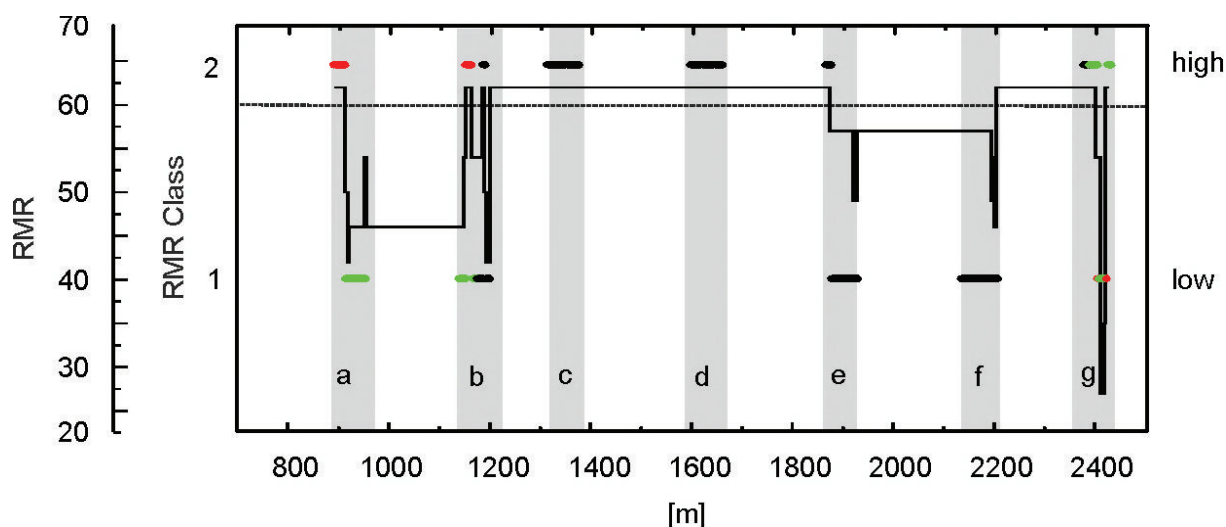


Figure 5.5: Spatial distribution of training and correctly or incorrectly classified test samples in the RMR classification along the tunnel alignment of the Faido Adit. The seven seismic profiles are highlighted as gray bars, the exact measured RQD is shown as a black line and the training samples are tagged as black circles. The test samples are tagged as either correctly (green dots) or incorrectly (red dots) predicted labels.

The usage of $\frac{2}{3}$ of training as support vectors indicates that the generalization process is not optimal; however, an acceptable weighted prediction accuracy P_w of 70 % is achieved for the FA-RMR classification, so that P_w is nearly as high as the weighted training accuracy A_w , which could be regarded as a sign of successful generalization. Nonetheless, the prediction accuracy varies strongly between the single classes, with 97 % correctly predicted Class 1 labels and 43 % correctly predicted Class 2 labels (Fig. 5.5). It may be interpreted that despite the implementation of a directed acyclic graph for the test phase, the weight put on the class that contained more training samples is much stronger than for the smaller class.

From Figure 5.5 it is obvious that all falsely classified Class 2 samples are situated in the seismic profiles a and b, whereas all correctly predicted Class 2 labels are encountered in the seismic profile g. For the seismic profiles a and b, the total discontinuity spacing s_t appears to be generally lower and the uniaxial compressive strength σ_c generally higher than those for seismic surveys c-g (cf. Fig. 2.3 in Sec. 2.1.1), which may have influenced the result, because the seismic velocities are sensitive to changes in the total discontinuity spacing s_t and the uniaxial compressive strength σ_c .

In Figure 5.6 the support vectors of both classes are mainly restricted to a small subspace, where a large number of support vectors is necessary to define the optimal decision boundary B with a very small margin, and "node points". Examples of such node points are Points 1 to 3 in Figure 5.6. These indicate that the optimal decision boundary B is

not well defined in these areas, which could be caused by noise in the data. In Chapter 3, the low variability of the data and the proximity of a large number of data points to the class boundary at $RMR = 60$ are discussed and might be the cause of the poorly defined optimal decision boundary B . In these classification results, all information from the model construction indicates an overfitted model. Some connection between the RMR classes and the seismic velocities is evident but not sufficient in the Faido Adit data set for an automated rock-mass classification.

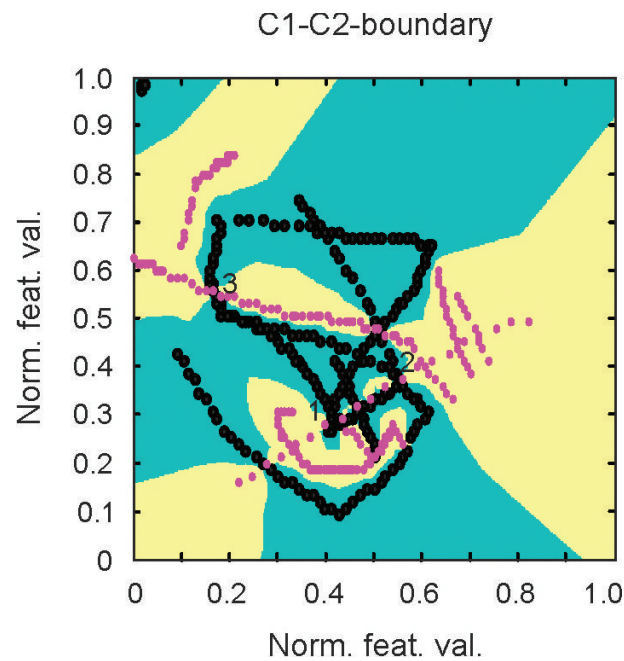


Figure 5.6: 2-D plot of the binary classifier (C1-C2-boundary) between Class 1 (green area) and Class 2 (yellow area) of the RMR classification based on the Faido Adit data set. The separating optimal decision boundary B is visualized in 2-D by calculating the euclidean norm of the support vectors in reference to the grid points of an equidistant 2-D grid over the normalized input space and by allocating the class label of the nearest support vector to the grid point in question. The support vectors of Class 1 are sketched as black circles and those of Class 2 as purple circles.

5.3 RQD Prediction in the Glendoe Tunnel 1-m Data Set

The training set of the RQD classification of the 1-m data set from the Glendoe Tunnel (GT-1-m-RQD) is composed of 332 samples. Of these, 50 samples are assigned to Class 1, 36 samples are assigned to Class 2 and the remaining 246 samples are categorized as Class 3 (Tab. 5.3). Both, Classes 1 and 2, were not correctly classified during training but Class 3 had a training accuracy of 100 %, which leads to a weighted training accuracy A_w of 33 %. The weighted training accuracy A_w remained more or less constant over the whole search space with variations of $< 0.5\%$. These variations are solely caused by increasing penalty parameter C at already high values of $\log(C) > 8$. Similar to the two classification tasks based on the FA data set, increasing γ values have no impact on the training result (Fig. 5.7). As a result, the smallest possible value for penalty parameter C ($\log(C) = -5$) is selected in the automated parameter selection (Tab. 5.4). Because all samples were classified as Class 3 in the training phase, severe underfitting or overfitting is conjectured for the classification task. Just as for the previous classifications, no variability in model construction and prediction accuracy were detected in test runs with different parameter sets C/γ .

Notation	Unit	RQD	RMR	RQD	RMR
Interval	[m]	1.0	1.0	4.0	4.0
N_x	[No.]	332	364	29	29
N_{C1}	[No.]	50	139	1	8
N_{C2}	[No.]	36	225	5	21
N_{C3}	[No.]	246	-	23	-
P_x	[No.]	69	37	12	14
P_{C1}	[No.]	16	9	2	3
P_{C2}	[No.]	7	28	0	9
P_{C3}	[No.]	46	-	10	-

Table 5.3: Description of the training and test data set for the RQD and RMR classification tasks in the Glendoe Tunnel. The number of feature vectors in the training set is specified as N_x , the number of feature vectors in each class in the training subset N_{c1-3} , the number of feature vectors in the test set is P_x and the number of feature vectors of each single class in the test set are named P_{c1-3} .

Notation	Unit	RQD	RMR	RQD	RMR
Interval	[m]	1.0	1.0	4.0	4.0
$\log(C)$		-5	15	-5	-5
$\log(\gamma)$		-15	-15	-15	-15
A_w	[%]	33	50	34	50
T_{AC1}	[%]	0	7	0	0
T_{AC2}	[%]	0	93	20	100
T_{AC3}	[%]	100	-	83	-
s	[%]	60	78	66	72
s_{C1}	[%]	60	96	100	100
s_{C2}	[%]	91	68	100	62
s_{C3}	[%]	53	-	57	-
P_w	[%]	33	50	33	50
P_{AC1}	[%]	0	0	0	0
P_{AC2}	[%]	0	100	0	100
P_{AC3}	[%]	100	-	100	-

Table 5.4: Details on the training and test results of the RQD or RMR classification tasks in the Glendoe Tunnel. The notation includes the logarithm of the kernel bandwidth $\log(\gamma)$, is the logarithm of the penalty parameter $\log(C)$, the weighted averaged accuracy over all classes A_w , the number of correctly classified labels in each respective class T_{AC1-3} , the number of support vectors for all classes s and for each class separately s_{C1-3} . The weighted prediction accuracy is denominated P_w and the prediction accuracy of each single class is listed as P_{AC1-3} .

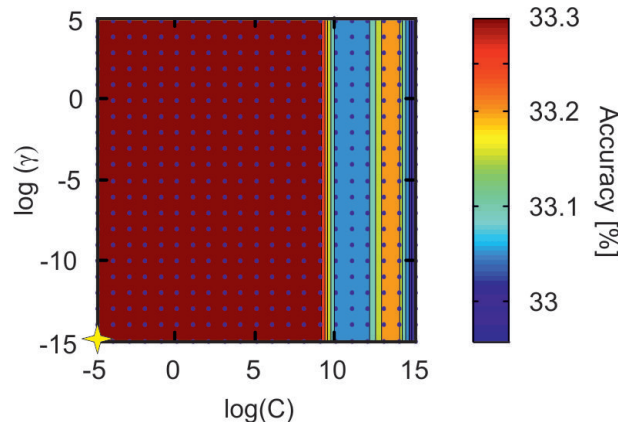


Figure 5.7: Results from the grid search on the parameter set C/γ for the GT-1-m-RQD. The A_w varies by about 33 % over the whole search space with with less than 0.5 % variation. The parameter set C/γ with the smallest values for the highest achieved accuracy is automatically selected as best-fit parameter set for model construction (yellow star).

Figure 5.8 reveals that the training data points of all 3 classes are distributed over several homogeneous areas. The faulted tunnel segment that is situated between tunnel meter -6329 and -6319, where the TBM-gripper sank into the tunnel wall, is both part of the

training data and the test data sets; even though this homogeneous area exhibits samples in both, the training and the test data set, none of the test samples at this location was correctly predicted, nor any other samples from Class 1 or Class 2 (Tab. 5.4). This was, however, expected as the training result had not entailed any correctly classified labels in one of these classes. The predicted labels stored during the test phase further reveal that all the incorrectly classified data points from Classes 1 and 2 were assigned to Class 3 during the prediction. This is a strong indicator for an extremely low generalization ability of the model.

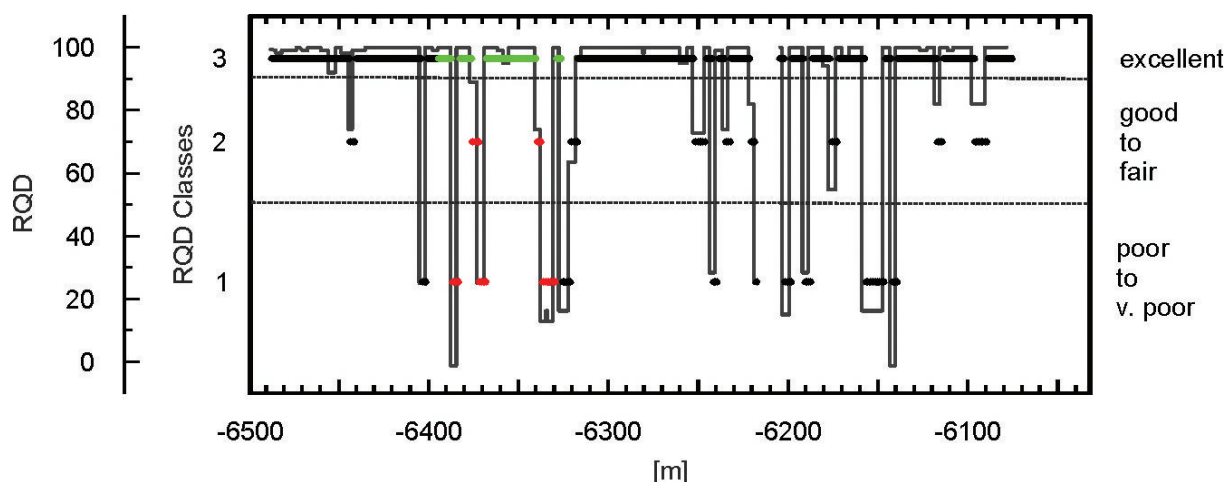


Figure 5.8: Spatial distribution of training and correctly or incorrectly classified test samples in the RQD classification along the tunnel alignment of the 1-m data set from the Glendoe Tunnel. The seven seismic profiles are highlighted as gray bars, the exact measured RQD is shown as a black line and the training samples are tagged as black circles. The test samples are tagged as either correctly (green dots) or incorrectly (red dots) predicted labels.

The percentage of support vectors in the total number of training samples in each respective class is largest for Class 2 with 91 %, and second largest for Class 1 with 60 %. Class 3 exhibits a relatively low percentage of 53 % of support vectors, compared to all other classification (Tab. 5.2 and Tab. 5.4). The data space covered by the support vectors is depicted in Figure 5.9 a-c for each of the binary classifiers. For each of these classifiers, most support vectors are situated in a small subspace visible in the upper right quarters of each subplot. The lower parts of these plots are defined by only a small fraction of the support vectors, and the decision boundaries seem much simpler in this lower area; however, in the upper right corner of Figure a-c, the model is highly complex and fits strongly to the support vectors. This clearly indicates strong overfitting of the model in conjunction with over-representation of the data samples in this subspace. Thus, strong overfitting of the model is deduced from:

1. the training algorithm assigns the majority samples to the largest class; the number of correctly classified Class 1 labels, expressing low rock-mass quality, is insignificant,
2. the highly complex decision boundaries that create small regions around the support vectors of both Classes 1 and 2 in small subspaces of the model and
3. assignment of the rest of the data space to the majority class.

The confidence in the data is, thus, high and the model even follows outliers and noise. These findings suggest that no significant information on the RQD classes is contained in the feature matrix that is built up by tunnel-driving parameters.

5.4 RMR Prediction on the Glendoe Tunnel 1-m Data Set

Just as for the FA-RMR classification task, the RMR values along the Glendoe Tunnel were categorized into 2 classes that contain either low values of $\leq 60RMR$ or $RMR\ values > 60$. During the grid search in the RMR classification in the Glendoe Tunnel at a 1-m sample interval (GT-1-m-RMR), A_w did not exceed 50 %. Similar to the classification tasks discussed so far, A_w was not influenced by changing values of the kernel bandwidth γ . Moreover, no changes in the A_w value occurred for values of $\log(C) < 7$. For $\log(C) \geq 7$, the A_w marginally decreased (Fig. 5.10); however, the variations do not exceed 1 % A_w and were therefore not regarded as significant. Nonetheless, the small increase in training accuracy for $\log(C) = 15$ leads to a much larger automatically selected penalty parameter C value for the GT-1-m-RMR classification, in comparison to the cross-validation result of the GT-1-m-RQD. For a variability of weighted training accuracy $A_w < 1\%$ in the grid search, the choice of an optimal parameter set for C and γ seems arbitrary. Tests on model construction with different, balanced parameter sets C/γ had no impact, which is in accordance with the results in the classification tasks discussed this far.

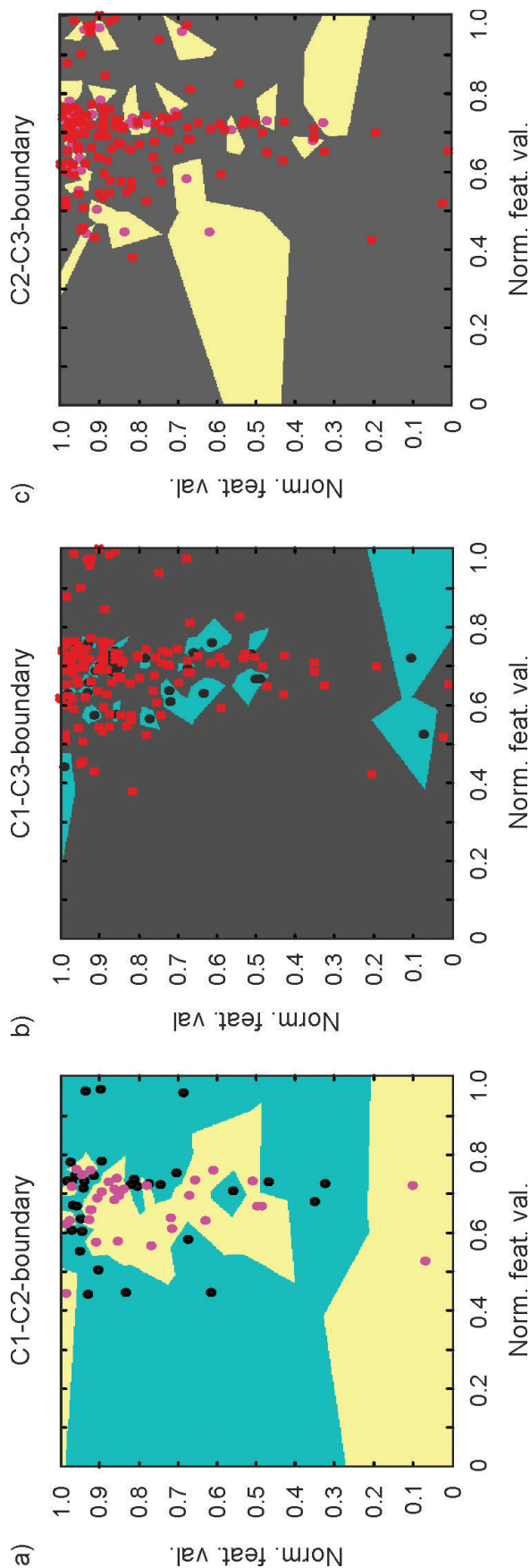


Figure 5.9: 2-D plots of the binary classifiers in the multi-class classification of the RQD classes based on the 1-m data set of the Glendoe Tunnel. The separating decision boundary is visualized in 2-D by calculating the euclidean norm of the support vectors in reference to the grid points of an equidistant 2-D grid over the normalized input space and by allocating the class label of the nearest support vector to the grid point in question. Class 1 is highlighted green and its support vectors are depicted as black circles, the support vectors of Class 2 (yellow area) are shown as purple circles and the gray areas are assigned to Class 3, whose support vectors are depicted as red crosses.

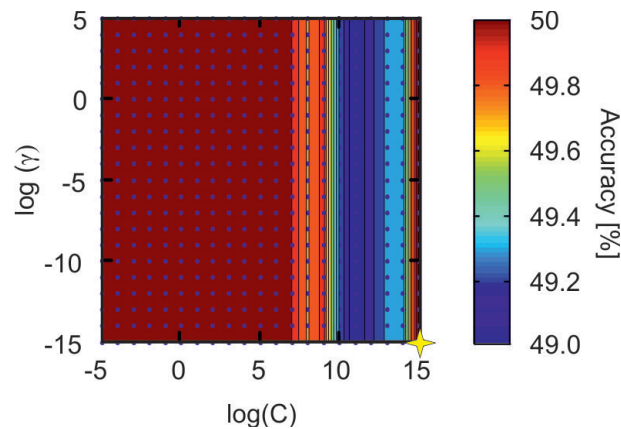


Figure 5.10: Results from the grid search on penalty parameter C and kernel bandwidth γ for the GT-1-m-RMR classification. The weighted training accuracy A_w only changes by 1 % between 49 to 50 % over the entire search space. The parameter set C/γ with the smallest values for the highest achieved accuracy is automatically selected as best-fit parameter set for model construction (yellow star).

Class 1 is smaller than Class 2 in the training data with 139 samples compared to 225 samples, respectively. Only 7 % of the Class 1 labels were correctly classified, while the training accuracy of Class 2 $T_{A_{C_2}}$ was 97 % (Tab. 5.4).

During model construction, 287 out of 364 training samples were used as support vectors. Of these, 134 support vectors belonged to Class 1 and 153 support vectors belonged to Class 2, which were 96 % and 68 % of the training samples in the respective classes. It is pointed out here that the class containing fewer data points, even though not strongly under-represented, again produced most support vectors. These comprised nearly all the available data points in the class, which suggests strong fitting of the model to the data points and consequently low generalization ability.

The test data set was comparatively small as it contained just 37 samples of which 9 and 28 data points belonged to Classes 1 and 2, respectively (Tab. 5.3). During the test phase solely Class 2 was predicted correctly and all Class 1 labels were additionally assigned to Class 2.

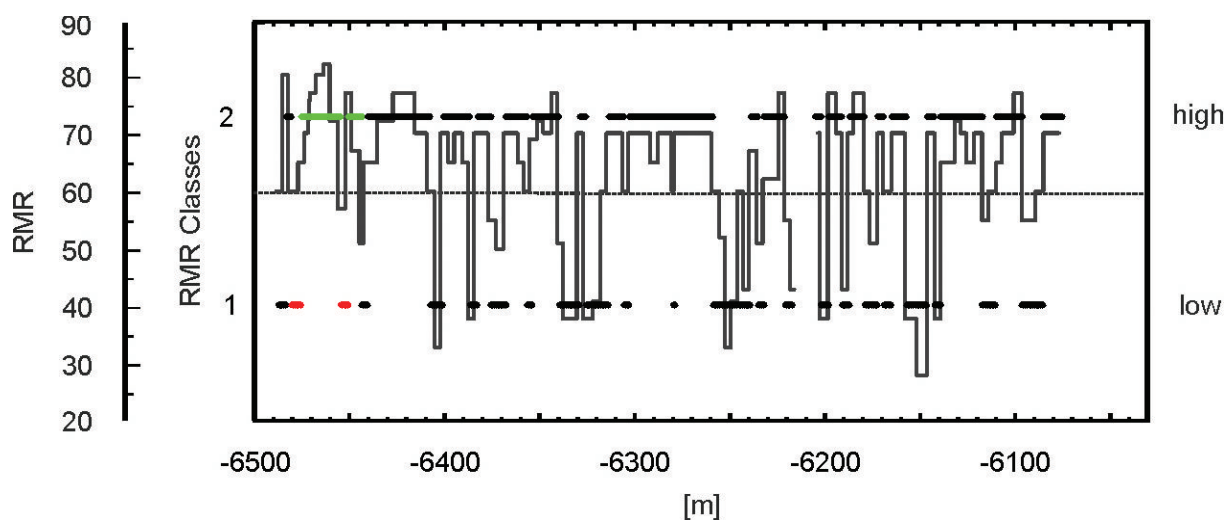


Figure 5.11: Spatial distribution of training and test samples along the tunnel alignment for the GT-1-m-RMR classification. The black line highlights the exact RMR values, and the dark gray bars designate tunnel segments, where geotechnically important fractured or faulted rock was mapped. The data samples are tagged as either green dots, for accurately predicted class labels, or red dots for incorrectly predicted class labels in the test data set. Black dots are assigned to training data points.

Similar to the GT-1-m-RQD classification, most support vectors are positioned in a small subspace in the upper right corner (Fig. 5.12). The pattern of support vectors from both classes is nearly chaotic. In this subspace, small regions are created around the support vectors of both classes. The model is defined by only a small number of support vectors in the remaining regions, and appears extremely simple in these areas, such that the connected areas assigned to one class increase in size, particularly for Class 2. It must be assumed that the feature space is not equally well defined by support vectors.

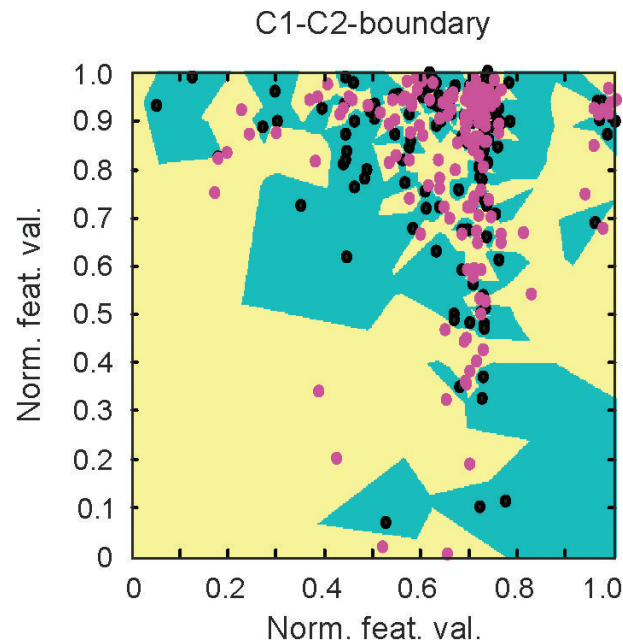


Figure 5.12: 2-D plot of the binary classifier (C1-C2-boundary) between Class 1 (green area) and Class 2 (yellow area) of the RMR classification based on the 1-m data set of the Glendoe Tunnel. The separating decision boundary is visualized in 2-D by calculating the euclidean norm of the support vectors in reference to the grid points of an equidistant 2-D grid over the normalized input space and by allocating the class label of the nearest support vector to the grid point in question. The support vectors of Class 1 are sketched as black circles and those of Class 2 as purple circles.

The support vector machine created in this classification task, thus, shows every sign of severe overfitting. Strong indicators of severe overfitting of the model include:

1. The training result,
2. the extreme percentage of 94 % of support vectors for Class 1,
3. the prediction result where all available test samples are assigned to Class 2, and
4. the complex model that creates small areas around the training samples of the minority Class 1.

One reason for the overfitting could lie in the proximity of the Class 1 test samples to the class boundary, which is documented in Figure 5.11 between tunnel meter -6485 and -6445. The variance in the data could thus be too small for proper separation of the classes as the noise level is quite high in the tunnel-driving parameters.

5.5 RQD Prediction on the Glendoe Tunnel 4-m Data Set

The 4-m data set comprises an exceptionally large number of missing values in the seismic P- and S- wave velocities, as described in Chapter 3. Matlab is generally able to deal with missing values, but numerical problems arise using the LIBSVM-package such that the feature vectors containing missing values need to be omitted from the data set. As a result, the size of the feature matrix discussed here is reduced to 41 samples, containing both tunnel-driving data and seismic P- and S-wave velocities. Taking into account the results from the classification tasks described and discussed thus far, it is likely that the database is not large enough for the complex task of RQD or RMR classification; however, the results of the FA classifications based on seismic measurements are superior to those of the GT classifications at 1-m sample spacing that are based on tunnel-driving data. The additional use of seismic velocities in the 4-m data set of the GT could thus positively influence the generalization ability of the model that is to be constructed.

The training data for the GT data set at 4-m sampling interval (GT-4-m-RQD) classification consists of 29 training samples of which 1 data point is labeled Class 1, 5 data points are labeled Class 2, and the remaining 23 data points are members of Class 3. During training, nearly all feature vectors from the minority Classes 1 and 2 were incorrectly classified (Tab. 5.4). One exception was encountered, composed of one single feature vector that was correctly assigned to Class 2. The A_w decreases with increasing $\log(C)$ from 30 % to 0 % training accuracy and is constant for varying values of the kernel bandwidth γ . The automatically selected $\log(C)/\log(\gamma)$ values are equal to the smallest pair of values in the search space (Fig. 5.13), which could be an indicator for underfitting. The model was not sensitive to and remained constant for varying $\log(C)/\log(\gamma)$ values, in accordance with previous findings in the classifications discussed above.

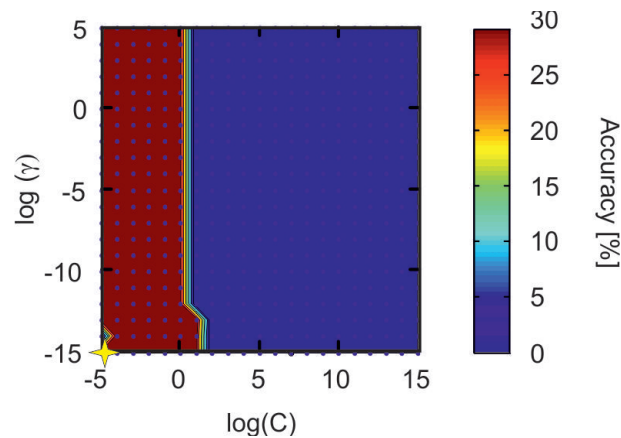


Figure 5.13: Results from the grid search on C and γ for the GT-4-m-RQD. The A_w decreases with increasing $\log(C)$ from 30 % to 0 % training accuracy. The parameter set C/γ with the smallest values for the highest achieved accuracy is automatically selected as best-fit parameter set for model construction (yellow star).

In Figure 5.14 the number of missing values in the seismic data becomes especially apparent when compared to Figure 5.8 in Section 5.3. Class 2 is not included in the test data set because the seismic data is missing for the data points between tunnel meter -6451 and -6439.

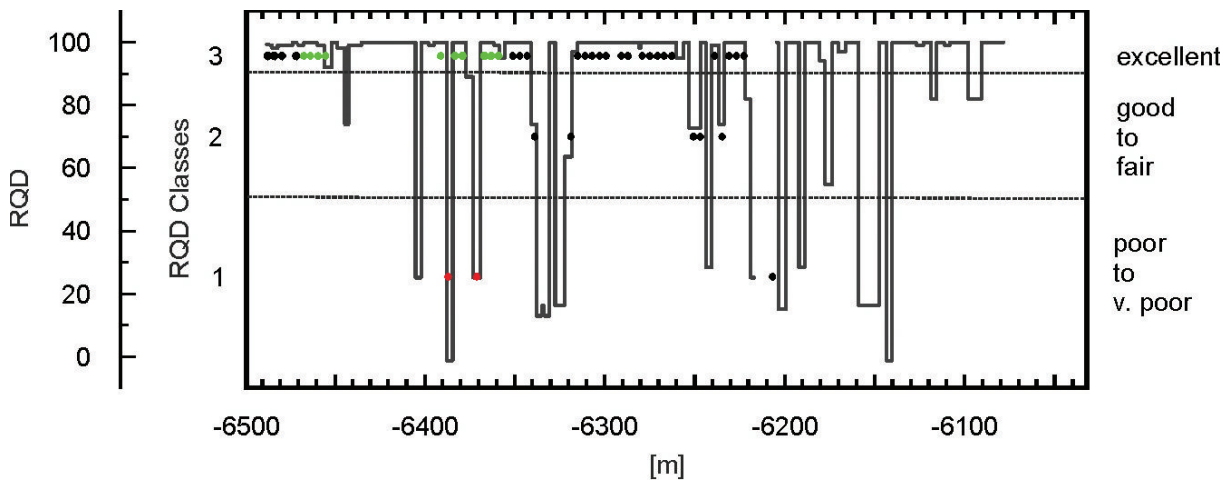


Figure 5.14: Spatial distribution of training and test samples along the tunnel alignment for the GT-4-m-RMR classification. The black line highlights the exact RMR values, and the dark gray bars designate tunnel segments, where geotechnically important fractured or faulted rock was mapped. The data samples are tagged as either green dots, for accurately predicted class labels, or red dots for incorrectly predicted class labels in the test data set. Black dots are assigned to training data points.

Class 3 is the only class, with 13 out of 23 training samples, for which not all feature vectors were used as support vectors (Tab. 5.4). At the same time, Figure 5.15 a-c show

that wide areas of the data space are assigned to one class, while the optimal decision boundary B is very poorly defined by the feature vectors.

In the test phase, all test data points were assigned to Class 3, which is another strong indicator of low generalization ability; however no test labels of Class 2 are included and Class 1 is composed of two samples in the test data set so that a statistical basis for a sound interpretation is not feasible. From the low model complexity shown in Figure 5.15 a-c and the training and test results, an underfitted model could be interpreted. Considering the data set size, as well as the poor data quality of the seismic data (1-D tomography, cf. Sec. 2.2), the strong noise in the tunnel-driving data, and the semi-quantitatively geological data collection, discussed in Section 2.1.2, it seems likely that the database is too small and noised for the task of RQD classification.

5.6 RMR Prediction on the Glendoe Tunnel 4-m Data Set

The RMR classification of the Glendoe Tunnel data set at 4-m sampling interval (GT-4-m-RMR) shows strong similarities to that of the GT-4-m-RQD classification. Of the Classes 1 and 2, Class 2 is the larger, with 21 training samples and 9 test samples, and was correctly classified to a 100 % T_{AC2} during training and also to a 100 % P_{AC2} during testing (Tab. 5.4) . Class 1 contains 8 training samples and 3 test samples, and was neither correctly classified during training nor correctly predicted during testing. On the contrary, all Class 1 test samples were incorrectly assigned to Class 2 during prediction instead. The automatically selected parameter set C/γ is, again, equal to the smallest pair of values in the search space (Fig. 5.13) and, as observed in all the other classification tasks, the kernel bandwidth γ has no impact on the weighted training accuracy A_w . Also similar to each of the previous tasks, the selection of balanced parameter sets C/γ did not influence model construction and prediction results.

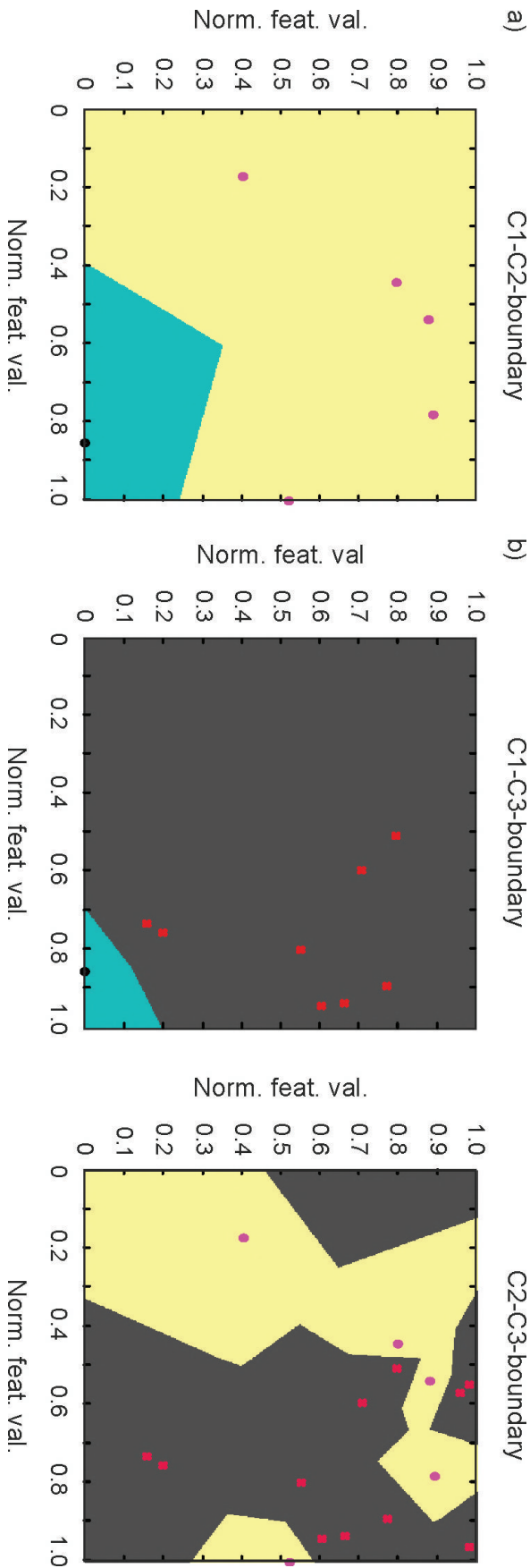


Figure 5.15: 2-D plots of the binary classifiers in the multi-class classification of the RQD classes based on the 4-m data set of the Glendoe Tunnel. The separating decision boundary is visualized in 2-D by calculating the euclidean norm of the support vectors in reference to the grid points of an equidistant 2-D grid over the normalized input space and by allocating the class label of the nearest support vector to the grid point in question. Class 1 is highlighted green and its support vectors are depicted as black circles, the support vectors of Class 2 (yellow area) are shown as purple circles and the gray areas are assigned to Class 3, whose support vectors are depicted as red crosses.

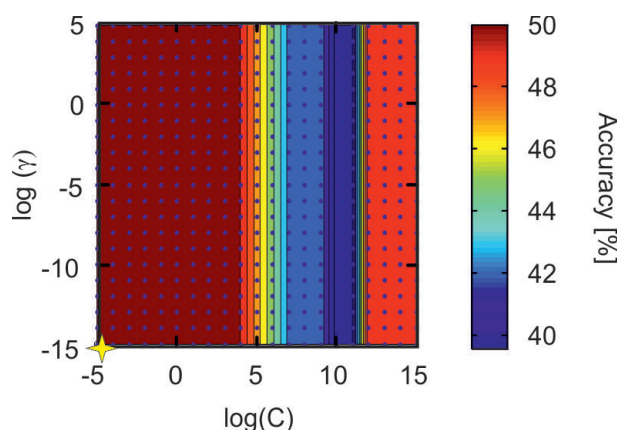


Figure 5.16: Results from the grid search on C and γ for the GT-4-m-RMR. The A_w changes with increasing $\log(C)$ but is constant for all $\log(\gamma)$ values. The parameter set C/γ with the smallest values for the highest achieved accuracy is automatically selected as best-fit parameter set for model construction (yellow star).

The data gaps and the sole correct prediction of Class 2 are apparent in Figure 5.14. Note that the data set only contains data points between tunnel meter -6487 and -6207, where the seismic survey took place.

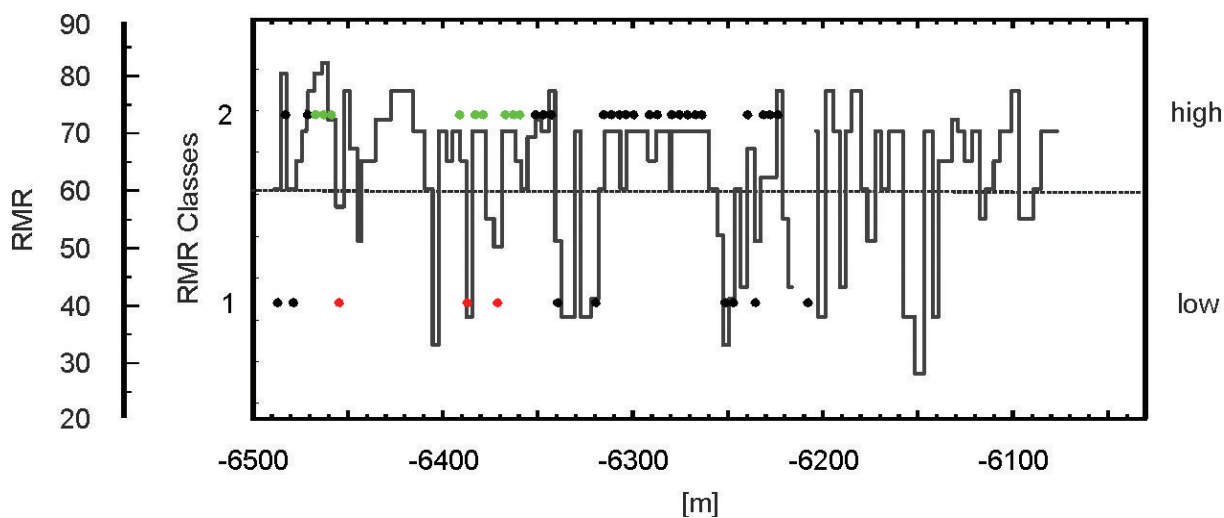


Figure 5.17: Spatial distribution of training and test samples along the tunnel alignment for the GT-4-m-RMR classification. The black line highlights the exact RMR values and the dark gray bars designate tunnel segments, where geotechnically important fractured or faulted rock has been mapped. The data samples that have been measured along the seismic profile are tagged as either green dots, for accurately predicted class labels, or red dots for incorrectly predicted class labels in the test data set. Black dots are assigned to training data points.

As expected from the results in Sections 5.1 to 5.4, all training samples of Class 1 are used as support vectors but only 62 % of Class 2 training samples. Similar to the GT-4-m-RQD

classification, the decision boundary seems poorly defined and the support vectors appear to be randomly distributed (Fig. 5.18), while the areas assigned to either Class 1 or 2 are continuous over wide areas of the data space. The model that was constructed for the GT-4-m-RMR classification is therefore regarded to be based on an insufficient number of data examples which results in an extremely underfitted model.

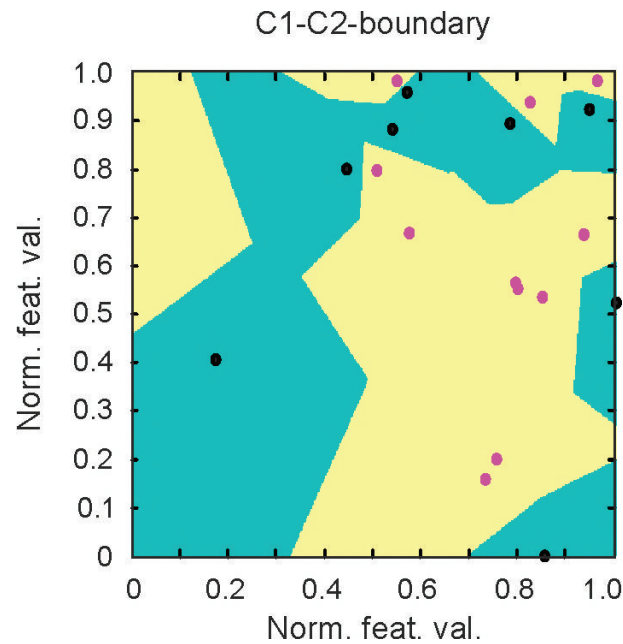


Figure 5.18: 2-D plot of the binary classifier (C1-C2-boundary) between Class 1 (green area) and Class 2 (yellow area) of the RMR classification based on the 4-m data set of the Glendoe Tunnel. The separating decision boundary is visualized in 2-D by calculating the euclidean norm of the support vectors in reference to the grid points of an equidistant 2-D grid over the normalized input space and by allocating the class label of the nearest support vector to the grid point in question. The support vectors of Class 1 are sketched as black circles and those of Class 2 as purple circles.

6 Discussion

The aim of this study was to establish and evaluate an expert system for rock-mass classification based on high-resolution data that was gathered during tunnel construction. From various pattern recognition algorithms considered, the support vector machines (SVMs) have been selected because of their straight forward nature, applicability to small data sets, secure convergence to the global optimum, robustness against overfitting. Moreover, SVMs work well for future updating processes, as only the support vectors need to be stored in the memory.

Parameters included in the data base for training and testing of the SVMs, the so called features, are seismic body-wave velocities obtained with the Integrated Seismic Imaging System (ISIS) and tunnel-driving parameters that are automatically stored during tunnel advance. The classes to be predicted, also called target, are based on the Rock Quality Designation (RQD) index and the Rock Mass Rating (RMR) factor, respectively. Three classes, from low to high rock-mass quality, are distinguished for the RQD and two for the RMR in both available data sets, the Faido Adit (FA) and the Glendoe Tunnel (GT). The statistical evaluation of the two data sets unveiled low correlation between the features and the target of the classification in the input-space. An interrelation between the RQD or RMR, respectively, and the Young's modulus was not verified. Taking into account that SVMs can detect hidden relationships in data by mapping into a higher dimensional feature space, this approach was followed up onto.

For SVM construction, the available data sets need to be separated into training and test subsets without overlap. Generating a new procedure of data subset generation for training and testing was inevitable, as several features are inherent to the data, such as the small number of available samples, the strong homogeneity of the rock-mass that resulted in a strongly peaked value distribution and, in consequence, unequally sized RQD and RMR classes. This procedure of separating the data set into subsets for training and testing, orientates itself on the size of the largest homogeneous area along the surveyed tunnel segment. Thus, it can be largely avoided that homogeneous units are present during both, training and testing. This is mandatory to reduce neighboring effects and to increase the stability of the prediction performance. The distribution pattern of rock-mass classes along the tunnel, consequently, influenced the size of training and test subsets. In both, the Faido Adit and the Glendoe Tunnel, large homogeneous areas of high rock-mass quality are separated by small areas of low rock-mass quality, where the rock exhibits a dense

pattern of structures. This afflicts very small numbers of either training or test samples in the minor classes if the class distribution, which can reduce the significance of the prediction result, as observed during the Class 1 prediction in the RQD classification of the Faido Adit. This class was underrepresented during testing and showed zero effective prediction. To investigate these relationships, the code of the corresponding algorithms in the used LIBSVM-library (Chang and Lin, 2010) was reprogrammed, such that the training and test accuracy of each single class is specified. Moreover, the procedure for performance evaluation of training and testing was changed. Instead of the averaged accuracy, the weighted averaged training- A_w and prediction accuracy P_w constitute the basis for the model assessment. This way, the effect of unequal success in the $n(n-1)/2$ binary classifications of a multi-class classification was accounted for.

Most importantly, however, the general applicability of the classification approach of the support vector machines to rock-mass classification in tunneling has to be evaluated. To this end, the model performance of each trained support vector machine is assessed and the factors that may contribute to the model behavior are analyzed. The model performance can be evaluated by regarding the interaction of several model features:

1. the weighted average training accuracy A_w and the training accuracy of the single classes T_{AC_i} ,
2. the weighted average prediction accuracy P_w and the prediction accuracy of the single classes P_{AC_i} ,
3. the best-fit parameter set C/γ ,
4. the amount of support vectors in reference to the class size, and
5. the model complexity.

The weighted average prediction accuracy P_w in respect to the weighted average training accuracy A_w gives information on how well the model was able to deduce general rules from the data set (generalization ability). If the weighted average prediction accuracy P_w is similar to the weighted average training accuracy A_w , the probability that the classification did work out well is high. The smaller the weighted average prediction accuracy P_w is in respect to the weighted average training accuracy A_w , the lower is the ability to assign the test samples to the correct class based on the rules learned from the training data set. Both classifications, RQD and RMR, of the Faido Adit showed high values for the weighted average training accuracy A_w and similarly high weighted average prediction accuracies P_w . These findings indicate generally successful classification, even though the prediction performance on Class 1 in the FA-RQD classification was low. A quite different picture is drawn from the training and prediction results of the Glendoe Tunnel

classifications. Here, the weighted average training accuracy A_w does not exceed 34 % for the RQD classifications based on either the 1-m or the 4-m data set (GT-1-m-RQD and GT-4-m-RQD), and 50 % for the 1-m or 4-m RMR classifications (GT-1-m-RMR and GT-4-m-RMR), respectively. The test samples of the minority and intermediate classes –the smallest class and the second largest class, respectively– were assigned to the majority class –the largest class and, simultaneously, the class containing highest rock-mass quality samples– throughout during prediction in both FA and GT. Class 1 of the FA-RQD exhibits stronger similarity to the prediction results of the Glendoe Tunnel as Class 1 was also completely assigned to the majority class, Class 3, during prediction; however, unlike the results for the minority and intermediate classes in each of the Glendoe Tunnel classifications, Class 1 in the FA-RQD showed high training accuracy. This is not necessarily conclusive for a better generalization ability of the model but it should be taken into account that the number of test samples of FA-RQD Class 1 is extremely small. Thus, the zero prediction accuracy could be a side effect of the subset generation discussed above.

The values of the penalty parameter C and the kernel bandwidth γ that are selected during the cross-validation before training also contain information on the model performance. The higher C and the smaller γ , the less are the Lagrange multipliers α constrained. The model then follows the data increasingly, which entails high model complexity and a high number of support vectors. This in turn leads to low generalization ability and thus decreasing prediction accuracy: A so called overfitting takes place. In the opposite case, with decreasing C and increasing γ , the model becomes simpler, leading to an underfitting of the model. In severe cases of both, overfitting and underfitting, the test data is likely to be assigned to the largest class in the data set during prediction. For each of the classification tasks carried out in this study, the parameter set C/γ exhibited extreme values with only one distinction:

1. For the FA-RQD, the FA-RMR and the GT-1-m-RMR, the penalty parameter C is extremely high the kernel bandwidth γ is extremely low.
2. For the GT-1-m-RQD, the GT-4-m-RQD and the GT-4-m-RMR, the penalty parameter C and the kernel bandwidth γ are both extremely low.

From the high penalty parameter C and the extremely low kernel bandwidth γ overfitting might be inferred. The prediction accuracy for single classes in the FA-RQD and FA-RMR is smaller than the training accuracy but still on a level of 70 % for the RQD and 74 % for the RMR that indicates that a successful learning process has taken place.

Class 1 is of major interests in each classification, as it contains the rock samples exhibiting lowest self-support of the rock mass. In case of the RQD classification this means the

lowest discontinuity spacing. A different reason for the poor classification of FA-RQD Class 1 might be the selection of a non-optimal set of parameters C/γ . In Chapter 4 the concept of a multi-class classifier is described, where each class is trained separately against all other classes. This leads to the construction of $n(n-1)/2$ binary classifiers. For each of the constructed $n(n-1)/2$ binary classifiers in a multi-class classification there exists a pair of optimal parameters. This parameter set is not necessarily the same for all of the binary classifiers. For the model construction, however, the same set of parameters has to be used for all of the binary classifiers constructed. Otherwise, the decision boundaries of the $n(n-1)/2$ binary classifiers would not be compatible. To check on the robustness of the training and prediction accuracy of the single classes, T_{AC_i} and P_{AC_i} , the models were trained anew with randomly selected sets of parameters C/γ . The test with arbitrary selection of C and γ caused no effect in none of the models, even for C and γ that exhibited different A_w in the average training accuracy A_w surface. Different publications on the matter, however, discuss a strong influence of C and γ (e.g., Chang and Lin, 2010). This behavior should therefore be investigated further in future studies.

In the Glendoe Tunnel classifications the training and prediction accuracy of the single classes, T_{AC_i} and P_{AC_i} , as much as weighted average training accuracy A_w and the weighted average prediction accuracy P_w already suggest that all available samples are assigned to the majority class. Except for the RQD classification on the 4-m data set, where A_w even goes down to 0 %, the average training accuracy A_w surface (e.g., Fig. 5.7) exhibit variations below 1 %. It is concluded that no optimal parameter set C/γ was detectable in the search space of the grid search, even though the chosen grid size is large (e.g., Keerthi and Lin, 2003; Kanevski et al., 2009). The evaluation of all classifications of the Glendoe Tunnel, therefore, suggest that the data base does not explain the variance in the target variables RQD and RMR.

The number of support vectors adds information to the foundation of the assessment on the prediction performance of a model. The support vectors are those data points that are closest to the class boundaries and whose removal from the data set would influence the orientation in space of the optimally separating hyperplane. In all classifications in this study, the number of support vectors in respect to the number of training samples is generally large. The model complexity, however, differs between the classification tasks.

For model visualization, the support vectors of each class were used to allocate the space taken by each class in the data space on a 2-D plot by usage of the euclidean norm. This, of course, is a very restricted picture of the model but nevertheless allows for an insight on the model complexity. Thus, the more general term decision boundary is used in the discussen, rather than the term hyperlpane that is defined as a decision boundary in the

higher dimensional feature space.

The most prominent differences in model complexity are visible between the classifications based on different data sets (FA, GT-1-m and GT-4-m), while the RQD and RMR classification based on the same data set are more similar. The classes from the Faido Adit classification tasks exhibit high training and sufficient prediction accuracy (FA-RQD Class 2 and 3 as well as both FA-RMR classes) and are marked by a percentage of support vectors around $\frac{2}{3}$ of the training samples. Both classifications, FA-RQD and FA-RMR, also exhibit decision boundaries that are well defined by support vectors over large areas of the feature space. Nonetheless, some node points, where support vectors of two classes are densely packed, exist as much as smaller areas of uncertainty that do not appear to be defined by support vectors. The areas that are densely packed by support vectors might be caused by noise and overlap in the feature space of neighboring classes so that the progression of the decision boundary becomes complex. A non-severe case of overfitting is therefore assumed for Faido Adit classifications. Here, additional parameters with explanatory power regarding the variance in the target variables, RQD and RMR, might be needed for further contouring of the decision boundary. In comparison, the GT-1-m classification on RQD and RMR exhibit extremely complex separating hyperplanes. The support vectors are accumulated in a small subspace of the feature space, where small areas around spatially strongly limited clusters of support vectors are created. Outside of this subspace, wide areas with few to no support vectors are identifiable, leading to regions of uncertainty. Because the size of the feature space depends on the normalized data, these regions could either be caused by a large number of outliers or they could reflect real variability within the data that is sparsely covered by example vectors. If the latter, the data does not consistently reflect the possible combinations of features for one class, which negatively influences the generalization ability, and thus, the prediction performance of a SVM.

For the Glendoe Tunnel, those classes that achieved the poor result of 0 % prediction accuracy P_{AC_i} also generally exhibit extremely high percentages of support vectors on the number of training samples. This also holds true for the Class 1 in the FA-RQD classification. The complete assignation of smaller classes to the largest available class is also a sign of low generalization ability and occurs at extreme over- or underfitting.

Most training samples in the GT-4-m-RQD and GT-4-m-RMR are assigned to be support vectors and appear to be distributed randomly in the feature space. Thus, the decision boundaries of the extremely simple models are insufficiently determined, leading to the incapacity of the algorithm to separate classes during training or testing. It is concluded that the size of the data base for the GT-4-m data set is too small for rock-mass quality classification.

For the Faido Adit, the RQD and RMR classes were similarly well predicted. In Chapter 3 it was shown that the RMR values in the Faido Adit peak close to the class boundary at $RMR = 60$ and that the range of values is generally strongly restricted in the small data set. Nonetheless, it was possible to correctly distinguish high from low RMR labels to 70 % P_w . All falsely classified Class 2 labels in the FA-RMR classification are situated in the first two seismic profiles, whereas all correctly predicted Class 2 labels are encountered in the last seismic profile (cf. seismic profile g in Figure 5.5 in Sec. 5.2). The incorrectly predicted test samples comprise generally lower total discontinuity spacing s_t and high uniaxial compressive strength σ_c in comparison to the training and correctly predicted Class 2 samples (cf. Fig. 2.3 in Sec. 2.1.1). Seismic velocities are known to be sensitive to changes in the total discontinuity spacing s_t and the uniaxial compressive strength σ_c , which is one reason why they are expected to be sensitive to RMR classes. A similar result was achieved for the FA-RQD classification, where the RQD class "good" was separable from the RQD class "excellent" based on seismic body-wave velocities. The high training accuracy for poor rock-mass quality samples combined in Class 1, whose decision boundaries do not appear more simple or complex than the C2-C3 decision boundary, may indicate that the poor prediction result for this class is attributed to the very small number of test samples available. This Class 1 (FA-RQD) contains samples of rock mass with increased fracturing or faulting. Such a decrease in the discontinuity spacing, however, is mostly evoked in tectonically stressed rocks and faulted zones, and those, in turn, are affected by a high variability in rock-mass features, such as water content, discontinuity conditions and microstructures. Seismic velocities are known to be sensitive to such rock-mass features; however, these features are not accounted for in the RQD, which may explain the erroneously assigned Class 1 labels and the large number of support vectors in this class.

In Chapter 4 the separation of the data set into training and test data was discussed. It was explained that the use of samples from one homogeneous area in the test and training set will decrease the generalization ability of the algorithm because the samples are not independent from each other. By implementing the modified *leave-one-out* technique that orientates the test and training size on the size of the largest homogeneous area along the tunnel, the independency of the samples was increased. Yet, if one class is very large and another is very small, the apportionment can become problematically unequal, as is the case in the FA-RQD for Class 1. A larger data set with more variability in the data would solve this problem. One might argue that the modified *leave-one-out* technique would not be needed in the Faido Adit because the data was sampled along seven separated seismic profiles; however, this would require the knowledge on the extension of homogeneous rock-mass units outside the profiles. In fact, in case of the Faido Adit,

the RQD and RMR has been mapped outside of the seismic profiles. From Figure 2.3 it can be deduced that RQD and RMR values from different seismic profiles do belong partly to the same homogeneous units. It is thus justified to treat the data set as if it was connected. Nonetheless, the spatial distance between data samples of several seismic profiles might have influenced the generalization ability of the support vector machine in the Faido Adit in a positive way.

A general factor that might decrease the predictability of both RQD and RMR based on seismic velocities, is that seismic velocities contain 3-D information, whereas the rock-mass characteristics are mapped along a 2-D profile. Nonetheless, the structures mapped along the tunnel wall take effect in the rock mass perpendicular to the tunnel wall as well, which is one of the basic assumptions made during geological mapping in general. Even though, undetected structures, such as faults or lithological boundaries, which are not accounted for in the geological mapping, might occur and influence the seismic velocities.

The tunnel-driving data in this study did not provide feasible SVMs for rock-mass classification. It was already pointed out in Chapter 6, however, that this might be a case-sensitive effect and that tunnel-driving parameters should be further investigated as possible input parameters for automated rock-mass classification. Apart from that, large data sets of tunnel-driving parameters are collected during TBM-advance of which some have not been regarded in this work but might prove to contain valuable information for the classification task. In Section 1.6.2, it was shown that very low and very high rock strength, an important factor for the estimation of the rock-mass quality, similarly influence the tunnel-driving parameters, which could lead to ambiguities in the rules underlying the classification between low and high rock-mass quality.

It might be speculated here that seismic velocities are more sensitive to the rock-mass quality than tunnel-driving parameters. A consideration adding to this speculation is that strongly fractured rock has a similar effect on the performance of a TBM in comparison to unfaulted rocks with high rock strength. Seismic velocities, however, should decrease constantly with decreasing discontinuity spacing, if no acoustic closure or increasing stress counteracts the effect. Moreover, economic considerations could have influenced the style of driving of the TBM-operator. Nevertheless, no tunnel-driving data is available for the Faido Adit data set, so that no direct comparison can be performed and the hypothesis that seismic velocities are better fit for rock-mass classification cannot be validated. The comparatively high quality and the small cell size extremely enhanced the explanatory power of the seismic velocities in the Faido Adit in comparison to those in the Glendoe Tunnel. As a result, the usage of receiver arrays with small intervals between the receivers, similar to the Faido Adit survey, is proposed for future investigations. Securing constantly high seismic data quality should therefore be one focus of attention in further research

projects.

The description (Chap. 2) and statistical evaluation of the RMR and RQD (Chap.3) showed peaked distribution and small variance in the data as well as large homogeneous areas of high rock-mass quality, divided by small areas of low rock-mass quality. In conjunction with the small size of the GT-1-m data set, these factors might add to the low prediction performance of the RMR and RQD on the GT-1-m data sets. The classifications on the Faido Adit data set contains 897 data samples, more than twice as many data points as the GT-1-m data set.

7 Conclusion

Two fundamentally different results are achieved during rock-mass classification based on the data sets from the Faido Adit and the Glendoe Tunnel:

1. Based on high-resolution seismic data from the Faido Adit, the classification of RQD or RMR (FA-RQD and FA-RMR) classes proved feasible.
2. Based on either tunnel-driving data, or else tunnel-driving and seismic data combined, from the Glendoe Tunnel with lower resolution, the RQD and RMR classification did not provide satisfying results.

The classification of the RQD class containing poor rock-mass quality data samples, Class 1, from the Faido Adit exhibit strong similarities to the results of the Glendoe Tunnel.

Note that the variability in the rock-mass quality, expressed either as RQD or RMR, is extremely low for the Faido Adit data set and that most data samples show strong proximity to the class boundaries as a result. The mere fact that patterns, linking RQD or RMR to the seismic velocities were detected in the Faido Adit is therefore remarkable, especially for the small number of training samples available. With an extremely small kernel bandwidth γ and a high value for penalty parameter C , a relatively high weighted average training accuracy A_w and a large number of support vectors, the RQD and RMR classification of the Faido Adit show a strong tendency to overfit; however, the generalization ability in both classifications is acceptable, as the weighted average prediction accuracy P_w is only slightly reduced in comparison to the weighted average training accuracy A_w . This indicator for a successful model construction is aided by the balanced appearance of the model complexity over wide areas in the data space. It might be speculated, that including additional seismic parameters in the data base, such as the squared amplitudes, which is a measure for the reflectivity at a certain tunnel location, could enhance the prediction performance and, consequently, the ability to better describe the rock-mass quality.

For the Glendoe Tunnel, the training accuracies of the single classes reveal that the classes were not or poorly classified. The large number of support vectors and the high model complexity, where small regions are created around the training samples exhibit all characteristics of severe overfitting in the classifications on the GT-1-m data set; however, this conclusion is valid only for the small subspace which contains the large number of support vectors. The part of the feature space that contains few support vectors and low model complexity with poorly defined decision boundaries cannot be included. This area

was interpreted to reflect true variability in the data but insufficient samples. It is assumed that no rules were learned from the data set and, therefore, the prediction failed. The statistical evaluation presented in Chapter 3 showed that there exists little to no linear correlations in the Glendoe Tunnel data set. The models based exclusively on tunnel-driving parameters show severe cases of overfitting and extremely low generalization ability. These results do not rule out that higher order correlations exist between tunnel-driving parameters and rock-mass classes in general, but no evidence on this had been discovered in this study. It is, therefore, concluded that the tunnel-driving parameters do not contain information on the rock-mass classes, neither for the RQD, nor for the RMR; however, this does not necessarily mean that information on the rock mass cannot be inferred from tunnel-driving parameters, in general.

The additional use of seismic body-wave velocities in the GT-4-m data base has been inevitably accompanied by a significant reduction of the data set. Adding the seismic velocities to the data base did not influence the classification result positively. The observations on the GT-4-m classifications led to the conclusion that the data set is by far too small for a proper classification approach, such that no rules were learned from the data set and the prediction failed in consequence. The quality and spatial resolution of the seismic observations is, therefore, crucial for the reliability of the prediction of rock-mass classes. The classification results showed that the cell-size of the seismic tomography and, consequently, the source-receiver offset of the seismic set-up is crucial for the explanatory power of the P- and S-wave velocities for rock-mass quality, especially in yet small data sets. The careful planning of the seismic survey is, therefore, determined as a key requirement for the success of a fast and automated rock-mass classification and the detection of hazardous zones in the rock mass. Nevertheless, even with the limited size of the available data sets it was possible to show that SVMs are a powerful tool in real time expert systems for geotechnical applications. It is proven within this study that it is possible to predict rock-mass classifications out of high resolution seismic data with high accuracy.

8 Outlook

Several steps need to be taken in order to reach the long term aim of an automated rock-mass classification for tunneling based on seismic data and tunnel-driving parameters. First, the (seismic) data acquisition and the prediction via support vector machines should be integrated into one system and a user friendly interface should be developed. To this end, results from different test sites need to be comparable. Concepts and strategies to reach such conditions should include:

- the influence of the tunnel diameter,
- different layouts of tunnel boring machines,
- changes in the overburden,
- standardization of the seismic set-up and the seismic processing flow,
- standardization of the sampling interval.

It was shown in this study that the size of the receiver array and the frequency of shot points along the tunnel influences the explanatory power of the seismic velocities in regard to rock-mass classification. The comparatively high quality and the small grid cell size extremely enhanced the explanatory power of the seismic velocities in the Faido Adit in comparison to those in the Glendoe Tunnel. As a result, the usage of receiver arrays with small intervals between the receivers, similar to the Faido Adit survey, is proposed for future investigations. Securing constantly high seismic data quality should therefore be one focus of attention in further R&D projects.

In tunneling, the acquisition geometry of the seismic systems is restricted to the one-dimensional shape of the tunnel, leading to a restricted informative value on the spatial distribution of structures. Thus, structures with strongly oblique angles to the tunnel axis might not be detected. In consequence, the correlation to the true rock-mass conditions decreases. A receiver spread at 90° angles around the tunnel would increase the detection of structure and their spatial distributions.

Scientific advances pursued to achieve this aim currently include the integration of TBM-noise as a seismic source, because TBM-noise exhibits the highest possible spatial coverage of seismic signals, and wireless data loggers that are able to continuously log the full wave field of these signals. It is further recommended to investigate whether additional seismic parameters, as the squared amplitudes, the wave-polarities (kind of reflectors), or the S_1

and S_2 -wave (rock anisotropy) contribute to more precise conclusions on the rock-mass behavior. High reliability and testability of continuous acoustic coupling between rock and seismic receivers is necessary, especially for the integration of the squared amplitudes, a parameter that is sensitive to the degree of jointing. To this end test methods need to be developed. Furthermore, the incorporation of a heterogeneous velocity model is a prerequisite for the application of SVMs to the prediction of rock-mass classes ahead of tunneling.

The tunnel-driving data in this study did not provide feasible SVMs for rock-mass classification. It was already pointed out in Chapter 6, however, that this might be a case-sensitive effect and that tunnel-driving parameters should be further investigated as possible input parameters for automated rock-mass classification. Apart from that, large data sets of tunnel-driving parameters are collected during TBM-advance of which some have not been regarded in this work but might prove to contain valuable information for the classification task.

Another field of tasks that should be looked into further, especially when exploring new parameters in regard to their viability for rock-mass classification, is the automated parameter selection. Here, e.g., the combination of graphical models (GM) and, in a subsequent step, principal component analysis (PCA) replace the time consuming manual pre-selection.

The implementation of SVMs is also conceivable for other applications in rock engineering and in the wider field of geology, such as the determination of primary rock-mass properties, like the elastic moduli. This would open a wide field of practical and scientific applications beyond tunneling.

Acknowledgements

I would like to express my gratitude to my advisors Prof. Frank Schilling, Dr. Stefan Lüth and Dr. Rüdiger Giese. They helped me on many occasions with inspiring and insightful discussion and ideas but also gave me freedom and encouraged me to follow my ideas and plans. Many thanks to Prof. Thomas Bohlen for examining this study and to Dr. Ulrich Harms, who welcomed me at the Plattform Scientific Drilling and supported me as much as he could in the last months in my endeavor to finish this work.

This project would not have been possible without the funding of the BMBF and DFG through the project OnSITE in the framework of the GEOTECHNOLOGIEN program.

My special thanks go to my co-workers from the former Section Environmental Geotechnique and the Central Workshop of the GFZ for their commitment during all fieldworks and for providing the technical equipment that was the pre-requisite for the realization of the fieldworks.

Dr. Johannes Mohr was a great help, not only with inspiring and insightful discussion and ideas on the topic of classifications with support vector machines and artificial neural networks but also with the implementation of the programming code. The constructive ideas and discussions on data preparation and visualization with Dr. Mike Sips gave me new insights in data handling and preparation.

I owe thanks to Dr. Norbert Pralle from Züblin AG and Dr. Thomas Dickmann from Amberg Technologies AG for discussion on different topics, such as the engineering point of view on the possibilities and restrictions of seismic systems in tunneling.

Many thanks to Prof. Mutschler from the Karlsruher Institute of Technology, who gave me new insights on rock-mass characteristics.

Dr. Javier Quinteros always found time for discussion and advice on all matters of code writing. Julia Götz I would like to thank for here support in all matters regarding the editing and also for her excellent groundwork on the seismic velocity tomography for the Glendoe Tunnel in her diploma thesis.

I thank Dr. Birgit Hollenbach, Dr. Cassandra Fenton and Dr. Kirsten Rempel for proof-reading and friendship. inspired me with a fruitful discussion. Many thanks to Anne Kleyböcker for her friendship and whose outstanding ability to look on the bright side of everything always motivated me. Thanks also to all other PhD students who contributed

to the strong social network that I came to appreciate at the GFZ. The strong ongoing and unshaken support and encouragement I received from André was invaluable.

References

- Alimoradi, A., Moradzadeh, A., Naderi, R., Salehi, M. Z., and Etemadi, A. (2008). Prediction of geological hazardous zones in front of a tunnel face using TSP-203 and artificial neural networks. *Tunnelling and Underground Space Technology*, 23(6): 711–717. URL <http://www.sciencedirect.com/science/article/B6V58-4S26RR0-1/2/0e586740e9a8eb5b0f16e86a9288dff7>.
- Amberg, F. (2006). Geologie, Vortriebsmethoden und Bauhilfsmaßnahmen in der Multifunktionsstelle Faido. In: S. Löw, (ed.), *Geologie und Geotechnik der Basistunnels am Gotthard und am Lötschberg*. p.225–237. Symposium Geologie Alptransit, Hochschulverlag AG an der ETH Zürich, Zürich.
- Aminzadeh, F. and de Groot, P. (2006). *Neural Networks and Other Soft Computing Techniques with Application in the Oil Industry*. EAGE Publications, Netherlands.
- Aoki, K., Mito, Y., and Chang, C. S. (2007). The geostatistical prediction technique of geological conditions ahead of the TBM driving tunnel face. In: R. e Sousa, Olalla, and Grossmann, (eds.), *Proceedings of the 7th International Workshop on the Application of Geophysics to Rock Engineering*. ISRM Comission on Application of Geophysics to Rock Engineering, Lisbon.
- Ashida, Y. (2001). Seismic imaging ahead of a tunnel face with three-component geophones. *International Journal of Rock Mechanics and Mining Sciences*, 38(6): 823–831. URL <http://www.sciencedirect.com/science/article/B6V4W-43X1X64-1/1/b1841236589a10a5a1846a0692cadeba>.
- Bandis, S. C., Lumsden, A. C., and Barton, N. R. (1983). Fundamentals of rock joint deformation. *International Journal of Rock Mechanics and Mining Sciences and Geomechanics Abstracts*, 20(6): 249 – 268. URL <http://www.sciencedirect.com/science/article/B6V4V-4814W8Y-T5/2/20280ecc2964d500de4c33b5fee72827>.
- Barton, N. (2007). *Rock Quality, Seismic Velocity, Attenuation and Anisotropy*. Taylor and Francis, London.
- Barton, N., Lien, R., and Lunde, J. (1974). Engineering classification of rock masses for the design of tunnel support. *Rock Mechanics*, 6: 183–236.
- Bernardos, A. G. and Kaliampakos, D. C. (2004). Modelling TBM performance with artificial neural networks. *Tunnelling and Underground Space Technology*, 19: 597–605.

- Berthold, M. and Hand, D. J. (2007). *Intelligent Data Analysis: An Introduction*. Springer Verlag, Heidelberg, 2 edition.
- BGS (1993). Sheet 73W (Scotland) Invermoriston - Solid Geology. British Geological Survey. Johnstone, G.S., Mykura, W.
- BGS (1996). Sheet 73E (Scotland) Foyers - Solid Geology. British Geological Survey. Mallick, D. I. J.
- Bieniawski (1973). Rock mass classification in rock engineering. *Trans. S. Afr. Inst. Civ. Engrs.*, 15: 335–344.
- Bieniawski, Z. T. (1984). *Rock Mechanics design in mining and tunneling*. Balkema, Rotterdam.
- Bieniawski, Z. T. (1989). *Engineering rock mass classifications - a complete manual for engineers and geologists in mining, civil, and petroleum engineering*. Wiley, New York.
- Bishop, C. (2006). *Pattern Recognition and Machine Learning*. Springer.
- Bohlen, T., Lorang, U., Rabbel, W., v. Müller, C., Giese, R., Lüth, S., and Jetschny, S. (2007). Rayleigh-to-shear wave conversion at the tunnel face - from 3D-FD modeling to ahead-of-drill exploration. *Geophysics Special Issue: Seismic Modeling with Applications to Acquisition, Processing and Interpretation*, 72(6): T67–T79.
- Borm, G., Giese, R., Otto, P., Amberg, F., and Dickmann, T. (2003). Integrated Seismic Imaging System for Geological Prediction during Tunnel Construction. In: *ISRM 2003 - Technology Roadmap for Rock Mechanics*. p.137–142. South African Institute of Mining and Metallurgy.
- Borm, G., Giese, R., Otto, P., and Selke, C. (2000). *Pneumatischer Impulsgenerator für Untertageseismik*.
- Brückel, E., Chawatal, W., Mertl, S., and Radinger, A. (2008). Exploration ahead of a tunnel face by TSWD - Tunnel Seismic While Drilling. *Geomechanik und Tunnelbau*, 1(5): 460–465.
- Bruns, B., Gattermann, J., Stahlmann, J., Edelmann, T., and Kassel, A. (2008). Automatische seismische Vorauserkundung in Tunnelbohrmaschinen. In: *6. Kolloquium Bauen in Boden und Fels. Tagungsband des 6. Kolloquium 'Bauen in Boden und Fels'* p.93–100. Technische Akademie Esslingen, Esslingen.
- Burges, C. J. C. (1998). A Tutorial to Support Vector Machines for Pattern Recognition. *Data Mining and Knowledge Discovery*, 2: 121–167.
- Casaopra, S. (1939). Studio petrographico dello gneis granitico Leventina, Valle Riviera e Valle Leventina (Canton Ticino). *Schweiz. Mineral. Petrogr. Mitt.*, 19: 449–717.

- Chang, C.-C. and Lin, C.-J. (2010). LIBSVM: a Library for Support Vector Machines. Department of Computer Sciences, National Taiwan University, Taipei 106, Taiwan. Software available at <http://www.csie.ntu.edu.tw/~cjlin/libsvm>.
- Cherkassky, V. (2006). Computational intelligence in earth sciences and environmental applications: Issues and challenges. *Neural Networks, Special Issue*, 19: 113–121.
- Cortes, C. and Vapnik, V. (1995). Support-Vector Networks. *Machine Learning*, 20(3): 273–297.
- Deere, D. U. and Deere, D. W. (1988). The RQD Index in Practice. ASTM Special Technical Publication, 984: 91–101.
- Deere, D. U., Hendron, A. J., Patton, F. D., and Cording, E. J. (1967). Design of surface and near surface construction in rock. In: C. Fairhurst, (ed.), *Failure and Breakage of Rock*, Proceedings 8th U.S. Symposium on Rock Mechanics. p.237–302. Society of Mining Engineers of AIME, New York.
- Demicco, R. and Klir, G. (2004). *Fuzzy Logic in Geology*. Elsevier Academic Press, San Diego.
- Dempster, T. J., Rogers, G., Tanner, P. W. G., Bluck, B. J., Muir, R. J., Redwood, S. D., Ireland, T. R., and Paterson, B. A. (2002). Timing of deposition, orogenesis and glaciation within the Dalradian rocks of Scotland: constraints from U-Pb zircon ages. *Journal of the Geological Society*, 159: 83–94.
- Dickmann, T. (2008). Theoretical and Applied Case Studies of Seismic Imaging in Tunnelling. *Geomechanik und Tunnelbau*, 1(5): 436–441.
- El-Naqa, A. (1996). Assessment of geomechanical characterization of a rock mass using a seismic geophysical technique. *Geotechnical and Geological Engineering*, 14: 291–305.
- Etter, U. (1999). *Vorerkundung und Prognose der Basistunnels am Gotthard und am Lötschberg*. Balkema, Rotterdam.
- Exadaktylos, G., Stavropoulou, M., Xiroudakis, G., de Broissia, M., and Schwarz, H. (2008). A spatial estimation model for continuous rock mass characterization from the specific energy of a TBM. *Rock Mechanics and Rock Engineering*, 41(6): 797–834.
- Fairhurst, C. and Lin, D. (1985). Fuzzy Methodology in Tunnel Support Design. In: *Proc. Symp. Strata Mech.* p.269–278.
- Fayyad, U. M., Piatetsky-Shapiro, G., and Smyth, P. (1996). From Data Mining to Knowledge Discovery: An Overview. In: *Advances in Knowledge Discovery and Data Mining*. p.1–34. American Association for Artificial Intelligence.

- Fettes, D. J. (1979). A metamorphic map of the British and Irish Caledonides. In: H. C. H. L. B. E. Harris, A. L., (ed.), *The Caledonides of the British Isles, Reviewed*. p.307–321. The Geological Society of London by Scottish Academic Press.
- Fratton, D. and Santamarina, J. C. (2002). Shear wave propagation in jointed rock: state of stress. *Geotechnique*, 52(7): 495–505.
- Fukui, K. and Okubo, S. (2006). Some Attempts for Estimating Rock Strength and Rock Mass Classification from Cutting Force and Investigation of Optimum Operation of Tunnel Boring Machines. *Rock Mechanics and Rock Engineering*, 39(1): 25–44.
- Ge, Q. Z., Ling, Z. C., Hui, X., and Zhang, G. (2008). High Efficient Classification on Remote Sensing Images Based on SVM. *The International Archives of the Photogrammetry, Remote Sensing and Spatial Information Sciences*, 37(B2): 1011–1014. Beijing.
- Giese, R., Dickmann, T., Eppler, T., and Lüth, S. (2006). Seismic tomography to investigate the tunnel surroundings of the Side Gallery West of the multifunctional station Faido. In: S. Löw, (ed.), *Geologie und Geotechnik der Basistunnels Gotthard und Lötschberg*. vdf Hochschulverlag.
- Giese, R., Klose, C., and Borm, G. (2005). In situ seismic investigations of fault zones in the Levantina Gneiss Complex of the Swiss Central Alps. In: P. K. Harvey, T. S. Brewer, P. A. Pezard, and V. A. Petrov, (eds.), *Petrophysical Properties of Crystalline Rock*. Vol.240 of *Special Publications*.p.15–24. The Geological Society, London.
- Giese, R. and Lüth, S. (2008). *Integrated Seismic Imaging System (ISIS) - How-to Manual*. German Research Centre for Geosciences GFZ.
- Girmscheid, G. (2008). *Baubetrieb und Bauverfahren im Tunnelbau*. Ernst & Sohn, Berlin, 2. edition.
- Goel, R. K., Jethwa, J. L., and Paithankar, A. G. (1996). Correlation between Barton's Q and Bieniawski's RMR - A new approach. *International Journal of Rock Mechanics and Mining Science and Geomechanics Abstracts*, 33(2): 179 – 181. URL <http://www.sciencedirect.com/science/article/B6V4V-4CJ6NYC-1G1/2/062c8ea4b69ddf8a7e9fc316c6f6c640>.
- Gokceoglu, C., Yesilnacar, E., Sonmez, H., and Kayabasi, A. (2004). A neuro-fuzzy model for modulus of deformation of jointed rock masses. *Computers and Geotechnics*, 31: 375–383.
- Grima, M. (2000). *Neuro-Fuzzy Modeling in Engineering Geology - Application to Mechanical Rock Excavation, Rock Strength Estimation, and Geological Mapping*. A. A. Balkema.

- Großbauer, K. (2009). Expert System Development for the Evaluation and Interpretation of Displacement Monitoring Data in Tunnelling. Ph.D. thesis, Graz University of Technology.
- Götz, J. (2008). Development of a heterogeneous velocity model for seismic prediction ahead of tunnel construction. Master's thesis, Technical University Berlin.
- Heim, A. (2007). S-351: Geological Tunnel Wall Mapping in the Glendoe Hydro Electric Power Plant - Headrace Tunnel. Unpublished.
- Hsu, C.-W., Chang, C.-C., and Lin, C.-J. (2010). A practical guide to support vector classification. Department of Computer Science, National Taiwan University, Taipei.
- Hsu, C.-W. and Lin, C.-J. (2002). A Comparison of Methods for Multiclass Support Vector Machines. *IEEE Transactions on Neural Networks*, 13(2): 415–425.
- Huang, T.-K., Weng, R., and Lin, C.-J. (2006). Generalized Bradley-Terry Models and Multiclass Probability Estimates. *Journal of Machine Learning Research*, 7: 85–115.
- Jacobs (2004). Reference Ground Conditions. Technical report, Scottish and Southern Energy plc.
- Jetschny, S. (2010). Seismic prediction and imaging of geological structures ahead of a tunnel using surface waves. Technical report, Karlsruher Institut für Technologie (KIT). URL <http://digbib.ubka.uni-karlsruhe.de/volltexte/1000019075>.
- Jetschny, S., De Nil, D., and Bohlen, T. (2010). On the propagation characteristics of tunnel surface-waves for seismic prediction. *Geophysical Prospecting*, 2: 245–256.
- Joachims, T. (1998). Text Categorization with Support Vector Machines: Learning with Many Relevant Features. In: *Proceedings of the 10th European Conference on Machine Learning*. Vol.1398 of *Lecture Notes in Computer Science*. 137–142. Springer.
- Johnson, M. R. W., Sanderson, D. J., and Soper, N. J. (1979). Deformation in the Caledonides of England, Ireland and Scotland. In: *The Caledonides of the British Isles - reviewed*. Geological Society of London, London.
- Kanevski, M., Pozdnoukhov, A., and Timonin, V. (2009). *Machine Learning for Spatial Environmental Data - Theory, Applications and Software*. EPLF Press.
- Keerthi, S. S. and Lin, C.-J. (2003). Asymptotic behaviours of support vector machines with Gaussian kernels. *Neural computation*, 15(7): 1667–1689.
- Kim, K.-Y., Kim, C.-Y., Kim, K.-S., and Yoon, H.-K. (2008). Relationship of drilling data and rock properties using drilling data acquisition system. In: *World Tunnel Congress 2008 - Underground Facilities for Better Environment and Safety*. p.155–163. ITA-AITES, Agra - India.

- Klose, C. (2004). Engineering geological rock mass characterisation of granitic gneisses based on seismic in-situ measurements. In: GeoForschungsZentrum Potsdam Scientific Technical Report. Vol.4pp.127. URL <http://www.gfz-potsdam.de/bib/pub/str0408/0408.htm>.
- Klose, C., Löw, S., Giese, R., and Borm, G. (2007). Spatial prediction of geological rock mass properties based on in-situ interpretations of multi-dimensional seismic data. *Engineering Geology*, 93: 99–116.
- Klose, C. D. (2002). Fuzzy rule-based expert system for short-range seismic prediction. *Computers and Geosciences*, 28(3): 377 – 386. URL <http://www.sciencedirect.com/science/article/B6V7D-45PS8WC-9/2/87811ea063127c62b5cd5dd2c462e031>.
- Kneib, G., Kassel, A., and Lorenz, K. (2000). Automatic seismic prediction ahead of the tunnel boring machine. *first break*, 18(7): 295–301.
- Knerr, S., Personnaz, L., and Dreyfus, G. (1990). *Neurocomputing: Algorithms, Architectures and Applications* Vol.F68 of NATO ASI. Springer-Verlag.
- Kulatilake, P., Fellow, A., and Panda, B. (2000). Effect of Block Size and Joint Geometry on Jointed Rock Hydraulics and REV. *Journal of Engineering Mechanics*, 126(8): 850–858.
- Kulatilake, P. H. S. W., Um, J., Wang, M., Escandon, R. F., and Narvaiz, J. (2003). Stochastic fracture geometry modeling in 3-D including validations for a part of Arrowhead East Tunnel, California, USA. *Engineering Geology*, 70(1-2): 131–155. URL <http://www.sciencedirect.com/science/article/B6V63-48NKR9R-1/1/532d0201fc674c5bd5c548877ce9b478>.
- Lifeng, Y. and Youshu, Z. (2006). Debris Flow Hazard Assessment Based on Support Vector Machine. *Wuhan University Journal of Natural Sciences*, 11(4): 897–900.
- Lin, H.-T. and Lin, C.-J. (2003). A study on sigmoid kernels for SVM and the training of non-PSD kernels by SMO-type methods. Technical report, Department of Computer Science, National Taiwan University. URL <http://www.csie.ntu.edu.tw/~cjlin/papers/tanh.pdf>.
- Lüth, S., Giese, R., Otto, P., Krüger, K., Mielitz, S., Bohlen, T., and Dickmann, T. (2008a). Seismic investigations of the Piora Basin using S-wave conversions at the tunnel face of the Piora adit (Gotthard Base Tunnel). *International Journal of Rock Mechanics and Mining Sciences*, 45(1): 86–93.
- Lüth, S., Giese, R., Rechlin, A. J., Heim, A., and Consortium (2009). *Seismic Prediction in Tunneling: New Trends in Hardware Development and Interpretation Concepts*.

- In: EURO: TUN 2009, 2nd International Conference on Computational Methods in Tunnelling Ruhr University Bochum, 9-11 September 2009. p.1–4.
- Lüth, S., Rechlin, A., Giese, R., Tzavaras, J., Gross, C., Buske, S., Jetschny, S., DeNil, D., and Bohlen, T. (2008b). Seismic Prediction ahead of a tunnel face - Modeling, field surveys, geotechnical interpretation. *International Journal of the JCRM*, 4(2): 47–51.
- Lüth, S., Rechlin, A. J., Giese, R., Buske, S., Groß, K., Tzavaras, J., Bohlen, T., De Nil, D., and Jetschny, S. (2008c). Seismic Prediction Ahead of a Tunnel Face - Modelling, Field Surveys, Geotechnical Interpretation. In: *Proc. of the 8th International Workshop on the Application of Geophysics to Rock Engineering*, June 29th 2008 San Francisco, USA. .
- Marschall, P., Fein, E., Kull, H., Lanyon, W., Liedtke, L., Müller-Lyda, I., and Shao, H. (1999). Conclusions of the tunnel near-field program, Nagra Technical Report 99-07. Technical report, Nagra, Baden, Switzerland.
- Martino, J. B. and Chandler, N. A. (2004). Excavation-induced damage studies at the Underground Research Laboratory. *International Journal of Rock Mechanics and Mining Sciences*, 41: 1413–1426.
- May, F. and Highton, A. J. (1997). Geology of the Invermorriston district Memoir for 1:50 000 Geological Sheet 73W (Scotland).
- McCann, D. M., Culshaw, M. G., and Northmore, K. J. (1990). Rock mass assessment from seismic measurements. *Engineering Geology Special Publications*, Geological Society of London, 6: 257–266.
- McDowell, P. W. (1990). The determination of the dynamic elastic moduli of rock masses by geophysical methods. *Engineering Geology Special Publications*, 6: 267–274.
- Miranda, A. and Mello-Mendes, F. (1983). Drillability and drilling methods. In: *Proceedings of the 5th Congress International Society on Rock Mechanics*. Vol.5p.E195–E200.
- Mito, Y., Yamamoto, S., T. Shirasagi, and Aoki, K. (2003). Prediction of the geological condition ahead of the tunnel face in TBM tunnels by geostatistical simulation technique. *ISRM 2003 - Technology roadmap for rock mechanics*, *Proceedings International Symposium*.833–836.
- Mitterlechner, G., Mayer, H. A., and Furtmüller, G. (2007). Automatische Geologie-Klassifikation von TBM-Daten -Statistische Mustererkennung als Ansatz zur automatischen Klassifikation geologischer Eigenschaften in einem TBM-Sensordatenbestand. In: *ÖGG Fachseminar computerorientierte Methoden in der Geomechanik*. Vol.23 of B.
- Müller, B. (2007). Empfehlungen von geotechnisch-felsmechanischen Klassifikationen des

- Festgesteines und Festgebirges für den Felsbau. In: 35. Geomechanik Kolloquium, Veröff. Inst. für Geotechnik TU Bergakademie Freiberg. 5p.187–205.
- Mohr, J., Puls, I., Wrase, J., Priller, J., Behr, J., Kitzrow, W., Makris, N., Breiter, H., Obermayer, K., and Heinz, A. (2008). Synergistic effects of the dopaminergic and glutamatergic system on hippocampal volume in alcohol-dependent patients. *Biological Psychology*, 79(1).
- Nauck, D., Klawonn, F., and Kruse, R. (1994). *Neuronale Netze und Fuzzy-Systeme*. vieweg.
- Nauck, D. and Kruse, R. (1997). A neuro-fuzzy method to learn fuzzy classification rules from data. *Fuzzy Sets and Systems*, 89: 277–288.
- Nellessen, P. (2005). Vortriebssynchrone Prognose der Setzungen bei Flüssigkeitsschildvortrieben auf Basis der Auswertung der Betriebsdaten mit Hilfe eines Neuro-Fuzzy-Systems. Ph.D. thesis, Fakultät für Bauingenieurwesen, Ruhr-Universität Bochum.
- Otto, R., Button, E., Bretterebner, H., and Schwab, P. (2002). The Application of TRT - True Reflection Tomography - at the Unterwald Tunnel. *Felsbau*, 20(2): 51–56.
- Palmström, A. (1982). The volumetric joint count - A useful and simple measure of the degree of rock mass jointing. In: *Conference Proceedings of the 4th International Congress of IAEG. Vol.V. Balkema. India*, p 220-228,.
- Petronio, L. and Poletto, F. (2002). Seismic-while-drilling by using tunnel boring machine noise. *Geophysics*, 67(6): 1798–1809.
- Pettke and Klaper (1992). Zur Petrographie und Deformationsgeschichte des südöstlichen Gotthardmassivs. *Schweizer mineral. petrogr. Mitt.*, 72: 197–211. URL <http://dx.doi.org/10.5169/seals-54907>.
- Platt, J. C. (1998). Sequential Minimal Optimization: A fast Algorithm for training Support Vector Machines. Technical report, Microsoft Research.
- Platt, J. C., Cristianini, N., and Shawe-Taylor, J. (2000). Large Margin DAGs for Multiclass Classification. In: *Advances in Neural Information Processing Systems. Vol.12*p.547–553. MIT Press.
- Poisel, R., Tenschert, E., Bach, D., and Zettler, A. (1999a). Gebirgsklassifizierung und Regelung von Tunnelbohrmaschinen mittels Fuzzy Logik. *Felsbau*, 17(5): 486–492.
- Poisel, R., Zettler, A. H., Bach, D., Lakovits, D., and Kastner, W. (1999b). Rock mass rating based on Tunnel Boring Machine Data. *Felsbau*, 17(3): 168–174.
- Priest, S. D. (1993). *Discontinuity Analysis for Rock Engineering*. Chapman and Hall, London.

- Priest, S. D. and Hudson, J. A. (1976). Discontinuity spacings in rocks. *International Journal of Rock Mechanics and Mining Sciences Abstracts*, 13: 135–148.
- Rechlin, A. J., Lüth, S., and Giese, R. (2009). OnSITE: Integrated Seismic Imaging System and Interpretation for Tunnel Excavation. In: *Proceedings of the International Conference on Rock Joints and Jointed Rock Masses*, Tucson, Arizona, USA. .
- Ribacchi, R. and Fazio, A. L. (2005). Influence of Rock Mass Parameters on the Performance of a TBM in a Gneissic Formation (Varzo Tunnel). *Rock Mechanics and Rock Engineering*, 38(2): 105–127. URL <http://dx.doi.org/10.1007/s00603-004-0032-5>.
- Rüping, S. (2001). SVM Kernels for Time Series Analysis. In: *LLWA 01 - Tagungsband der GI-Workshop-Woche Lernen-Lehren-Wissen-Adaptivität*. Forschungsberichte des Fachbereichs Informatik der Universität Dortmundp.43–50.
- Rummel, F. and van Heerden, W. (1978). Suggested Methods for Determining Sound Velocity. *Journal of Rock Mechanics and Mining Sciences & Geomechanics Abstracts*, 15(2): 53–58.
- Sapigni, M., Berti, M., Bethaz, E., Busillo, A., and Cardone, G. (2002). Performance estimation using rock mass classifications. *International Journal of Rock Mechanics and Mining Sciences*, 39: 771–788.
- Scheidler, A. (2008). Zeitreihenprognose mittels lokaler Modelle und ihrer Globalisierung. Technical report, Fachbereich Informatik, Technische Universität Darmstadt.
- Schlicke, D., Schockemöhle, B., and Pierson, R. (2005). Bohrklassenermittlung im maschinellen Tunnelbau mittels Maschinendatenauswertung. *LACER*, 10: 407–416.
- Schölkopf, B. (1997). Support Vector Learning. Ph.D. thesis, Technical University of Berlin.
- Schölkopf, B. and Smola, A. (2002). *Learning with Kernels - Support Vector Machines, Regularization, Optimization, and Beyond*. MIT Press.
- Schneider, T. (1997). Gotthard-Basistunnel - Sondiersystem Piora-Mulde: Schlussbericht Sondierstollen Piora-Mulde, Phase 1, Geologie/Geotechnik/Hydrogeologie/Geothermie, Bericht 425cs. Technical report, Schweizerische Bundesbahn, Bauabteilung der Generaldirektion.
- Shahin, M. A., Jaksa, M. B., and Maier, H. (2009). Recent Advances and Future Challenges for Artificial Neural Systems in Geotechnical Engineering Applications. *Advances in Artificial Neural Systems*p.9.
- Shi, J., Ortiage, J. A. R., and Bai, J. (1998). Modular Neural Networks for Predicting Settlements during Tunneling. *Journal of Geotechnical and Geoenvironmental Engineering*p.389–395.

- Shirasagi, S., Yamamoto, T., Inou, M., Yamamoto, S., Yoshitada, M., and Aoki, K. (2001). Development of Intelligent TBM excavation control system. In: Särkkä and Eloranta, (eds.), *Rock Mechanics - a Challenge for Society*. p.615–620.
- Singh, B. and Goel, R. K. (1999). *Rock Mass Classification - A Practical Approach in Civil Engineering*. Elsevier Academic Press.
- Sjøgren, B. (1984). *Shallow Refraction Seismics*. Chapman and Hall.
- Sjøgren, B., Øfsthus, A., and Sandberg, J. (1979). Seismic classification of rock mass qualities. *Geophysical Prospecting*, 27: 409–442.
- SSE (2004a). Glendoe Hydro Electric Scheme - Annex R: Tenderer's Reference Ground Conditions. unpublished. Scottish Southern Energy plc.
- SSE (2004b). Glendoe Hydro Electric Scheme - Headrace and Tailrace Tunnels -Geological Longitudinal Section. unpublished. Scottish and Southern Energy plc.
- SSE (2007). Glendoe Hydro Project - TBM TRT Geological Fold Out Mapping. unpublished. Scottish and Southern Energy plc.
- Stacey, T. (1974). *Seismic Techniques in the Assessment of Rock Properties*. Ph.D. thesis, Imperial College of Science and Technology, Department of Geology, London.
- Stacey, T. R. (1976). Seismic assessment of rock masses. In: *Symposium on Exploration for Rock Engineering*. .
- Tanimoto, C. and Ikeda, K. (1983). Acoustic and mechanical properties of jointed rock. In: *Proceedings of 5th International Congress Rock Mechanics (ISRM)*. .
- Telford, W. M., Geldart, L. P., and Sheriff, R. E. (1990). *Applied Geophysics*. Cambridge university Press.
- Thuro, K. and Brodbeck, F. (1998). Auswertung von TBM-Vortriebsdaten - Erfahrungen beim Erkundungstollen Schwarzach. *Felsbau*, 16(1): 8–17.
- Thuro, K. and Spaun, G. (1997). Ingenieursgeologische und felsmechanische Untersuchungen. In: *Taschenbuch für den Tunnelbau*. Vol.21p.61–106. Deutsche Gesellschaft für Geotechnik e.V., Essen.
- Ulusay, R. and Hudson, J. (2007). The complete ISRM suggested methods for rock characterisation, testing and monitoring: 1974-2006. ISRM Turkish National Group, Ankara.
- Vanajakshi, L. and Rilett, L. R. (2004). A comparison of the performance of artificial neural networks and support vector machines for the prediction of traffic speed. In: *2004 IEEE Intelligent Vehicle Symposium, Parma, Italy, June 14-17*. .

- Vapnik, V. N. (1998). *Statistical Learning Theory*. John Wiley and Sons.
- Wang, W. and Liao, H. (2007). Rock fracture tracing based on image processing and SVM. In: *Third International Conference on Natural Computation*. p.632–635. IEEE.
- Welle, T. (2009). Niederschlagsbestimmung aus METEOSAT-Second Generation-Zeitreibendaten mit dem Methodenverbund ORFEUSS -Fallbeispiel Namibia-. Ph.D. thesis, Mathematisch-Naturwissenschaftliche Fakultät, Rheinische Friedrich-Wilhelms-Universität Bonn.
- Wittke, W., Druffel, R., Erichsen, C., Gattermann, J., Kiehl, J., Schmitt, D., Tegelkamp, M., Wittke, M., Wittke-Gattermann, P., and Wittke-Schmitt, B. (2007). *Stability Analysis and Design for Mechanized Tunneling*. VGE-Verlag, Aachen.
- Won, G. W. and Raper, R. W. J. (1997). Downhole geophysical investigations for a proposed deep highway cutting adjacent to a rail tunnel at Murrurundi, NSW, Australia. *Geological Society of London, Engineering Geology Special Publications*, 12: 283–291.
- Wu, T.-F., Lin, C. J., and Weng, R. C. (2004). Probability estimates for multi-class classification by pairwise coupling. *Journal of Machine Learning Research*, 5: 975–1005.
- Yao, X., Tham, L. G., and Dai, F. C. (2008). Landslide susceptibility Mapping Based on Support Vector Machine: A Case Study on Natural Slopes of Hong Kong, China. *Geomorphology*, 101: 572–582.
- Zettler, A. H., Poisel, R., and Stadler, G. (1996). Bewertung geologisch-geotechnischer Risiken mit Hilfe von Fuzzy Logik und Expertensystemen. *Felsbau*, 14(5): 352–357.

List of Figures

1.1	Schematic illustration of the tunnel-boring machine used in the Glendoe Tunnel.	16
1.2	Physical and dynamic properties of hard, unweathered igneous and metamorphic rocks.	21
1.3	Calculating of the maximal margin and determination of the optimally separating decision surface.	29
1.4	Introduction of slack variables to deal with noisy data and outliers.	32
1.5	Mapping data to a higher-dimensional feature space by usage of a mapping function.	33
2.1	Overview of the geographic position and geological setting of the Faido Adit in southern Switzerland.	37
2.2	Geological cross sections along the seismic surveys in the Faido Adit.	39
2.3	Rock-mass properties ($\sigma, s_t, Q, f, e, r, TRQD, RMR$) along the Faido Adit.	40
2.4	Geological setting of the Glendoe Hydro Electric Power Plant.	43
2.5	Geological cross section along the seismic survey in the Glendoe Tunnel.	45
2.6	Rock-mass properties ($s_t Q, f, e, r RMR, TRQD$) along the seismic survey in the Glendoe Tunnel.	47
2.7	Source and receiver geometry of the seismic surveys in the Faido Adit.	48
2.8	Seismic P- and S-wave velocities along the seismic profiles in the Faido Adit.	49
2.9	Schematic illustration of the source and receiver points of the seismic survey in the Glendoe Tunnel.	50
2.10	Configuration of the ISIS hardware on a tunnel-boring machine and schematic illustration of the wave-field propagation during the measurements in the Glendoe Tunnel.	51
2.11	Seismic P- and S-wave velocities along the seismic profile in the Glendoe Tunnel.	52
2.12	Tunnel-driving parameters along the survey in the Glendoe Tunnel.	55
3.1	Boxplots of the seismic velocities, the RQD and the RMR from the Faido Adit data set.	58
3.2	Relationship between the elastic dynamic modulus E_{dyn} and the rock-mass quality descriptive parameters RQD and RMR.	61

3.3	Boxplots of the tunnel-driving parameter and the target parameters, RQD and RMR, of the Glendoe Tunnel data set.	64
3.4	Boxplots of the seismic velocities of the Glendoe Tunnel data set.	65
3.5	Correlation matrix for the "1-m data set" of the Glendoe Tunnel.	66
3.6	Regression curves between tunnel-driving parameters and the RQD from the Glendoe Tunnel data set.	67
3.7	Regression curves between tunnel-driving parameters and the RMR from the Glendoe Tunnel data set.	68
3.8	Relationship between the elastic dynamic modulus E_{dyn} and the rock-mass quality descriptive parameters RQD and RMR.	69
4.1	Work flow of the implemented multi-class SVM.	73
4.2	Construction of the label vector and the feature matrix from a dataset. . .	74
4.3	Generation of data subsets for training and testing.	75
4.4	The selection of values for penalty parameter C and kernel bandwidth γ influences the model complexity and can lead underfitting, overfitting or good model generalization ability.	80
4.5	Comparison of the DAGSVM approach to the <i>one-against-one</i> method. . .	81
5.1	Results from the grid search on C and γ for the RQD classification based on the data set of the Faido Adit.	86
5.2	Spatial distribution of training and correctly or incorrectly classified test samples in the RQD classification along the tunnel alignment of the Faido Adit.	87
5.3	2-D plots of the binary classifiers in the RQD multi-class classification based on the Faido Adit data set.	89
5.4	Results from the grid search on C and γ for the RMR classification based on the Faido Adit data set.	90
5.5	Spatial distribution of training and correctly or incorrectly classified test samples in the RMR classification along the tunnel alignment of the Faido Adit.	91
5.6	2-D plot of the binary classifier of the RMR classification based on the Faido Adit data set.	92
5.7	Results from the grid search on C and γ for the RQD classification based on data from the Glendoe Tunnel survey with 1-m sample spacing.	94
5.8	Spatial distribution of training and correctly or incorrectly classified test samples in the RQD classification along the tunnel alignment of the 1-m data set from the Glendoe Tunnel.	95

5.9	2-D plots of the binary classifiers in the multi-class classification of the RQD classes based on the 1-m data set from the Glendoe Tunnel.	97
5.10	Results from the grid search on C and γ for the RMR classification based on data from the Glendoe Tunnel survey with 1-m sample spacing.	98
5.11	Spatial distribution of training and test samples along the tunnel alignment for the RMR classification based on data from the Glendoe Tunnel survey with 1-m sample spacing.	99
5.12	2-D plot of the binary classifier of the RMR classification task based on the 1-m data set from the Glendoe Tunnel.	100
5.13	Results from the grid search on C and γ for the RQD classification based on data from the Glendoe Tunnel survey at a 4-m sample spacing.	102
5.14	Spatial distribution of training and test samples along the tunnel alignment for the RMR classification based on data from the Glendoe Tunnel survey with 4-m sample spacing.	102
5.15	2-D plots of the binary classifiers in the multi-class classification of the RQD classes based on the 4-m data set from the Glendoe Tunnel.	104
5.16	Results from the grid search on C and γ for the GT-4-m-RMR.	105
5.17	Spatial distribution of training and test samples along the tunnel alignment for the RMR classification based on data from the Glendoe Tunnel survey with 4-m sample interval. The test samples are tagged as either correctly or incorrectly predicted labels.	105
5.18	2-D plot of the binary classifier of the RMR classification task based on the 4-m data set from the Glendoe Tunnel.	106
8.1	Linear regression between geotechnical and seismic variables from the Faido Adit data set.	147
8.2	Parallel coordinate plot of the seismic velocities and the RQD classes in the Faido Adit.	148
8.3	Parallel coordinate plot of the seismic velocities and the RMR classes in the Faido Adit.	149
8.4	Boxplots of the tunnel-driving parameter and the target parameters, RQD and RMR, of the Glendoe Tunnel "4-m data set".	151
8.5	Parallel coordinates for the RQD classification on the Glendoe Tunnel survey for both 1-m and 4-m sample interval.	152
8.6	Parallel coordinates for the RMR classification on the Glendoe Tunnel data set for both 1-m and 4-m sample interval.	153

List of Tables

1.1	Qualitative rating of the RQD.	11
1.2	Rating of RMR classes and short description of the corresponding intensity of tunnel support.	13
2.1	Orientation of the three major joint sets occurring in the Leventina and Lucomagno gneisses along the Faido Adit.	41
2.2	Geotechnically important structures along the Glendoe Tunnel surveyed area.	44
3.1	Basic statistics of the data from the Faido Adit.	59
3.2	Basic statistics of the data from the Glendoe Tunnel.	63
4.1	Overview of the classification tasks for the Faido and Glendoe surveys. . .	72
5.1	Description of the training and test data set for the RQD and RMR classification tasks in the Faido Adit.	84
5.2	Details on the training and test results of the RQD and RMR classification tasks in the Faido Adit.	85
5.3	Description of the training and test data set for the RQD and RMR classification tasks in the Glendoe Tunnel.	93
5.4	Details on the training and test results of the RQD or RMR classification tasks in the Glendoe Tunnel.	94
8.1	Details of construction of the Faido Adit.	145
8.2	Description of the Glendoe Tunnel and specifications of the TBM layout. .	145
8.3	Mineralogic composition of the Leventina Gneiss.	146
8.4	Mineralogic composition of the Lucomagno Gneiss.	146
8.5	Mineral composition of the Tarff Banded Formation.	146
8.6	Basic statistics of the Glendoe Tunnel data set at a 4-m sample spacing. .	150

Appendices

A Nomenclature

T_{Aci}	Training accuracy for a single class
s_{Ci}	Number of support vectors in a class
(X)	Training dataset
A_w	Weighted averaged training accuracy
A_t	Average accuracy over all classes (default in LIBSVM)
B_{Ci}	Decision boundary between two classes
CF_{ep}	Correction factor for engineering purpose, e.g., tunneling
CF_{od}	Correction factor for orientation of discontinuities with respect to the direction of construction
C_d	Condition of discontinuities
D_S	Discontinuity (plane or surface that marks a change in physical or chemical characteristics in a soil or rock mass) spacing
E_{dyn}	Young's modulus
H	Hyperplane
K	Kernel function
L	Length of the considered interval
L_D	Dual formulation of the optimization problem
L_p	Lagrangian formulation of the optimization problem
P_w	Weighted prediction accuracy
N_{ci}	Number of samples in a class
N_x	Size of training data set
P_{Aci}	Weighted prediction accuracy

P_x	Size of test set
Q	Water inflow (into the underground construction)
R^N	Feature space
T_{Aci}	Weighted prediction accuracy
T_c	Sum of correctly classified labels over all classes
V_p	Seismic compressional wave velocity
V_{pF}	Seismic compressional wave velocity measured in the field
V_{pL}	Seismic compressional wave velocity measured in the laboratory
V_s	Seismic shear wave velocity
W	Weathering of discontinuities
Φ	Mapping function
α_l	Percentage of occurrences of a specific rock variety
λ	Mean discontinuity frequency
μ	Shear modulus
ν	Poisson's ratio
ρ	Maximal margin
ρ_b	In-situ bulk density
σ_c	Uniaxial (also: unconfined) compressive strength
ξ_i	Slack variables
b	Offset of the decision surface
d_A	Discontinuity set A
d_B	Discontinuity set B
e	Aperture of discontinuities
f	Infilling of discontinuities

i	Index
k	Bulk modulus
l	Any given location
p	Persistence of discontinuities
r	Roughness of discontinuities
s_i	Support vectors
s_t	Total discontinuity spacing
t	Threshold value in the determination of the TRQD
w	Normal vector on the decision surface
x	Feature vector
x_{ti}	The length of the i th piece of drill core that exceeds the threshold value
y	Label vector
R_x	Rating value
ANN	Artificial neural network
DAGSVM	Directed acyclic graph support vector machine
FA	Faido Adit
GBT	Gotthard Base Tunnel
GT	Glendoe Tunnel
IQD	Interquartile distance
ISIS	Integrated Seismic Imaging System
ISRM	International Society for Rock Mechanics
LeG	Leventina Gneiss
LIBSVM	A library for support vector machines
LuG	Lucomagno Gneiss

QP	Quadratic programming problem
RBF	Gaussian radial basis function
SVM	Support vector machine
TBM	Tunnel-boring machine
TRQD	Theoretical Rock-Mass Quality Designation index

B Field Surveys

Technical Specifications

The Faido Adit

Tunnel Name		Faido Adit
Purpose		support and escape (GBT)
Rock Type		gneiss
Tunnel Excavation Method		drill-and-blast
Tunnel Length	[m]	2600
Tunnel Diameter	[m]	5
Total Surveyed Section Length	[m]	594
Tunnel Slope in Surveyed Section	[%]	12

Table 8.1: Details of construction of the Faido Adit.

The Glendoe Tunnel

Name		Glendoe Tunnel
Purpose		Hydro Electric Power Plant
Rock type		Hard rock: quartz-mica-schist, quartz-schist
Tunnel length	[m]	7524
Tunnel diameter	[m]	5.03/4.8
Length of survey	[m]	293.2
Tunnel slope along survey	[%]	0.080
Tunnel excavation method		TBM
Machine type		Open gripper TBM
Stroke	[mm]	1830
Cutter diameter	[mm]	5030
Number of cutters	No.	Single: 27 double: 4 total: 35
Cutter spacing	[mm]	Unknown
Cutter-head power	[kW]	2200
Cverage cutter-head speed	$\left[\frac{rev.}{min}\right]$	9.55
Max. applicable thrust force	[MN]	241 bar on 4 thrust cylinders
Max. applicable torque	[kNm]	2105

Table 8.2: Description of the Glendoe Tunnel and specifications of the TBM layout.

Mineralogic Composition

The Faido Adit

Minerals	Leventina Gneiss
	Orthogneiss [%]
Quartz	25-43
Feldspar	38-60
Mica	9-24
Accessories	1-5

Table 8.3: Mineralogic composition of the Leventina Gneiss in the Faido Adit Schneider (1997).

The Glendoe Tunnel

Minerals	Lucomagno Gneiss	
	Orthogneisses [%]	Paragneisses [%]
Quartz	20-55	20-70
Alkali-feldspar	0-45	-
Plagioclase	0-70	10-35
Sericite, Muscovite	0-20	0-30
Biotite	0-6	3-30
Garnet	-	0-15

Table 8.4: Mineralogic composition of the Lucomagno Gneiss in the Faido Adit with differentiation in sedimentary or granitic origin Schneider (1997).

Minerals	Tarff Banded Formation
	[%]
Quartz	69.38 ± 11.58
Mica	42.50 ± 20.77)
Garnet	10.00
Accessories	22.14 ± 8.81

Table 8.5: Mineral composition of the Tarff Banded Formation (Jacobs, 2004). Accessories, such as pyrite, chlorite and calcite are mainly encountered in joint fillings.

C Statistics

The Faido Adit

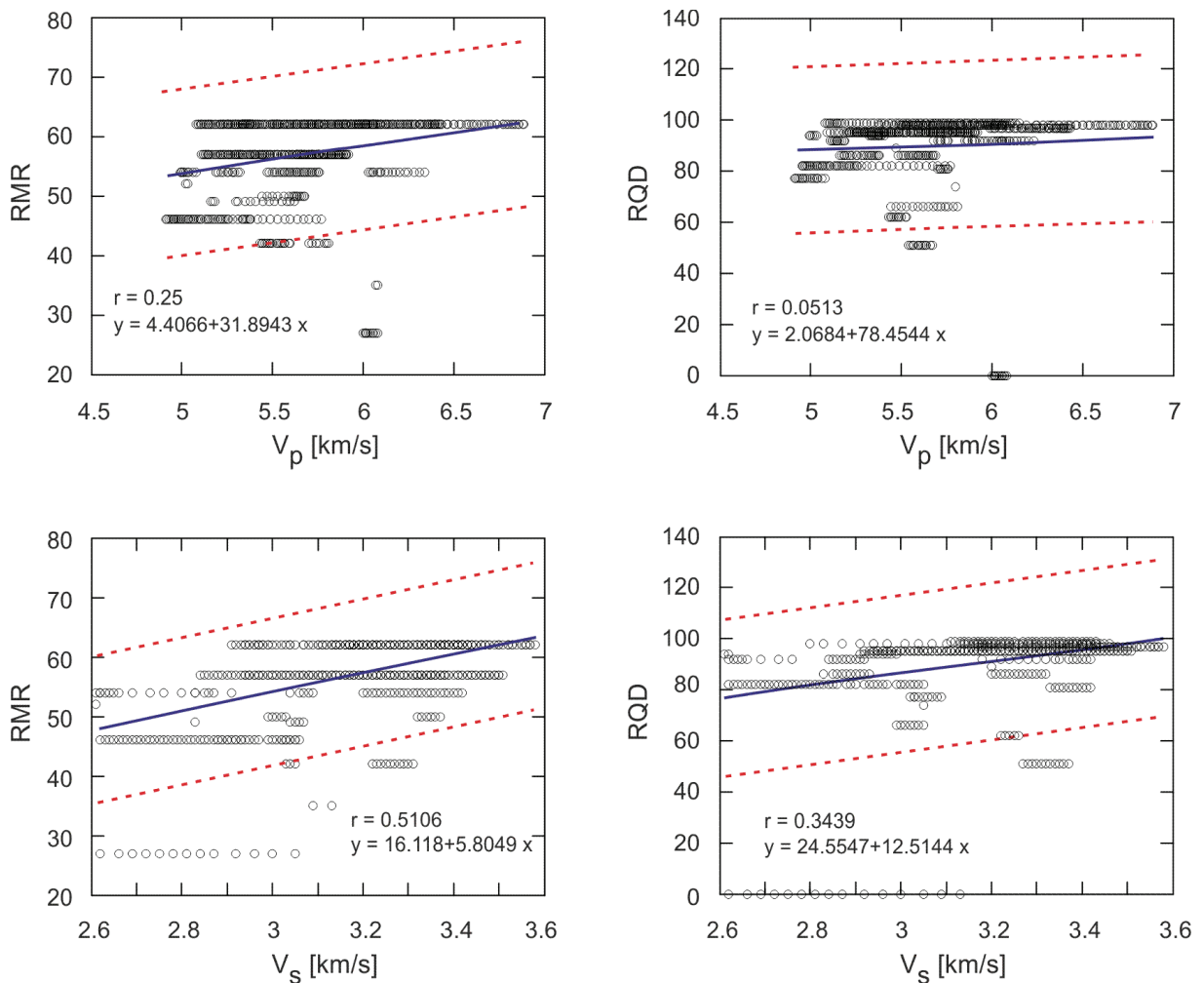


Figure 8.1: Linear regression between geotechnical and seismic variables from the Faido Adit data set. Black circles mark single data points, red dashed lines mark the 95 % confidence bounds and the blue line is the regression line. Generally, there is no linear correlation detectable between the targets of the SVM construction, which are either RMR or RQD, and the seismic velocities.

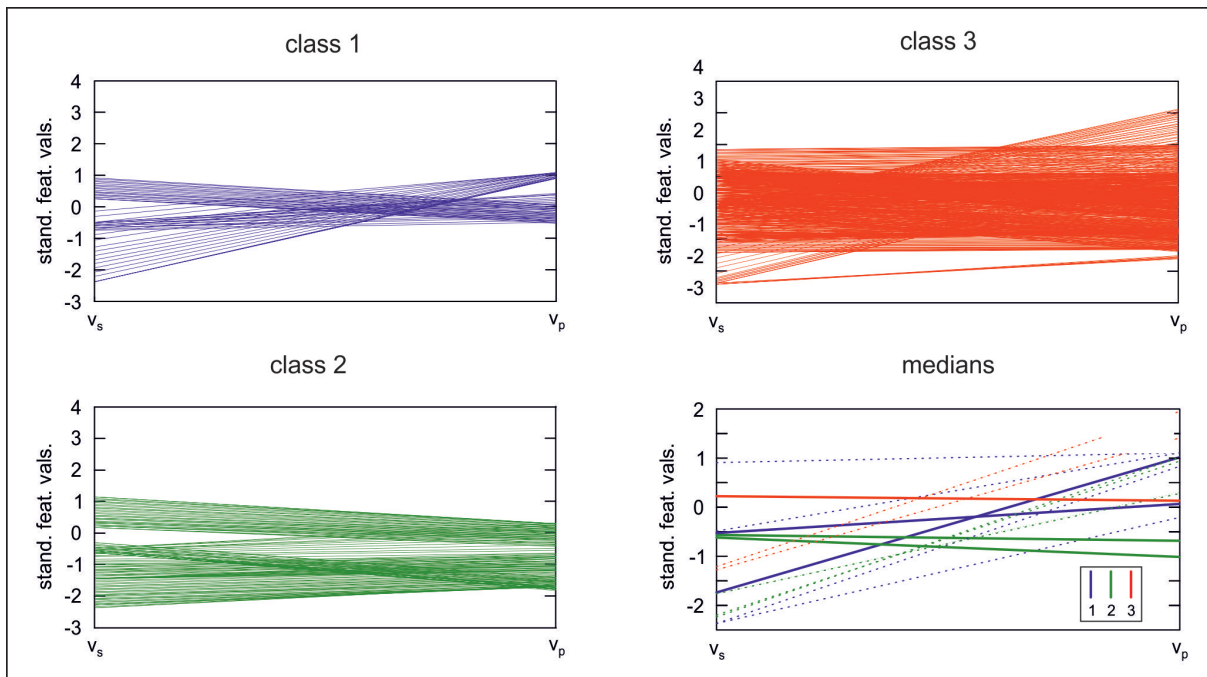


Figure 8.2: Parallel coordinate plot of the seismic velocities and the RQD classes in the Faido Adit. Each observational point in the n -dimensional space is represented as a polyline for which the intercepts with the vertical axes are the seismic velocities. The observational points are colored according to the class label attributed to the specific data points. Each feature is scaled to have a mean of 0 and a standard deviation of 1. (a) The values in Class 1 range from 0 to 75. (b) Class 2 includes values between 75 and 90, while (c) values contained in Class 3 range from 91 to 100. In (d) the median curve of each class and their 95 % confidence boundaries are depicted. The parallel coordinate plot does not reveal distinctive, unique patterns but different mean gradients of the polylines.

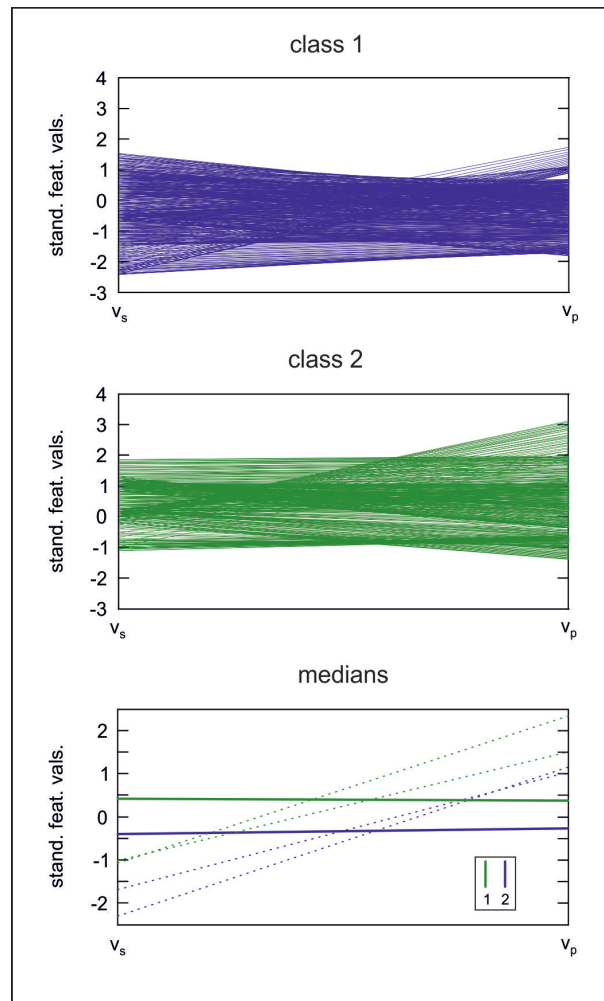


Figure 8.3: Parallel coordinate plot of the seismic velocities and the RMR classes in the Faido Adit. Each observational point in the n -dimensional space is represented as a polyline for which the intercepts with the vertical axes are the seismic velocities. The observational points are colored according to the class label attributed to the specific data points. Each feature is scaled to have a mean of 0 and a standard deviation of 1. (a) Class 1 comprises RMR values up to 60 and (b) Class 2 RMR values above 60. (c) The medians of both classes show a marked difference in their y -axis intercepts but similar gradients and no distinctive, unique patterns.

The Glendoe Tunnel

	Min	Max	Mean	Median	Std. Dev.	Skew	Kurt.
Penetration $[\frac{mm}{rev.}]$	5.19	59.22	23.47	21.11	13.11	0.81	3.19
Thrust Force $[kN]$	2875.6	6114.9	4530.8	4866.8	485.13	-1.46	4.58
C. Torque $[kNm]$	25.82	1225.1	639.76	658.06	109.94	-0.73	2.87
C. Speed $[\frac{1}{min}]$	8.54	9.74	9.51	9.59	0.26	-3.15	11.51
$V_s[\frac{km}{s}]$	1.01	5.43	3.44	3.38	0.62	0.46	3.16
$V_p[\frac{km}{s}]$	1.15	3.67	2.4	2.45	0.36	0.14	2.84
RQD	0	100	86	100	27.88	-1.93	5.32
RMR	28	81	63	67	12.24	-1.03	3.2

Table 8.6: Basic statistics evaluation of the Glendoe Tunnel data set at a 4-m sample spacing. By enlarging the sample interval to 4 m, the outliers in the tunnel-driving parameters are reduced, as is concluded from the reduced skew and thus smaller tails, the closeness of the kurtosis to the normal distribution as compared to the 1-m sample spacing, and the convergence of the mean and median values (cf. Table 8.6).

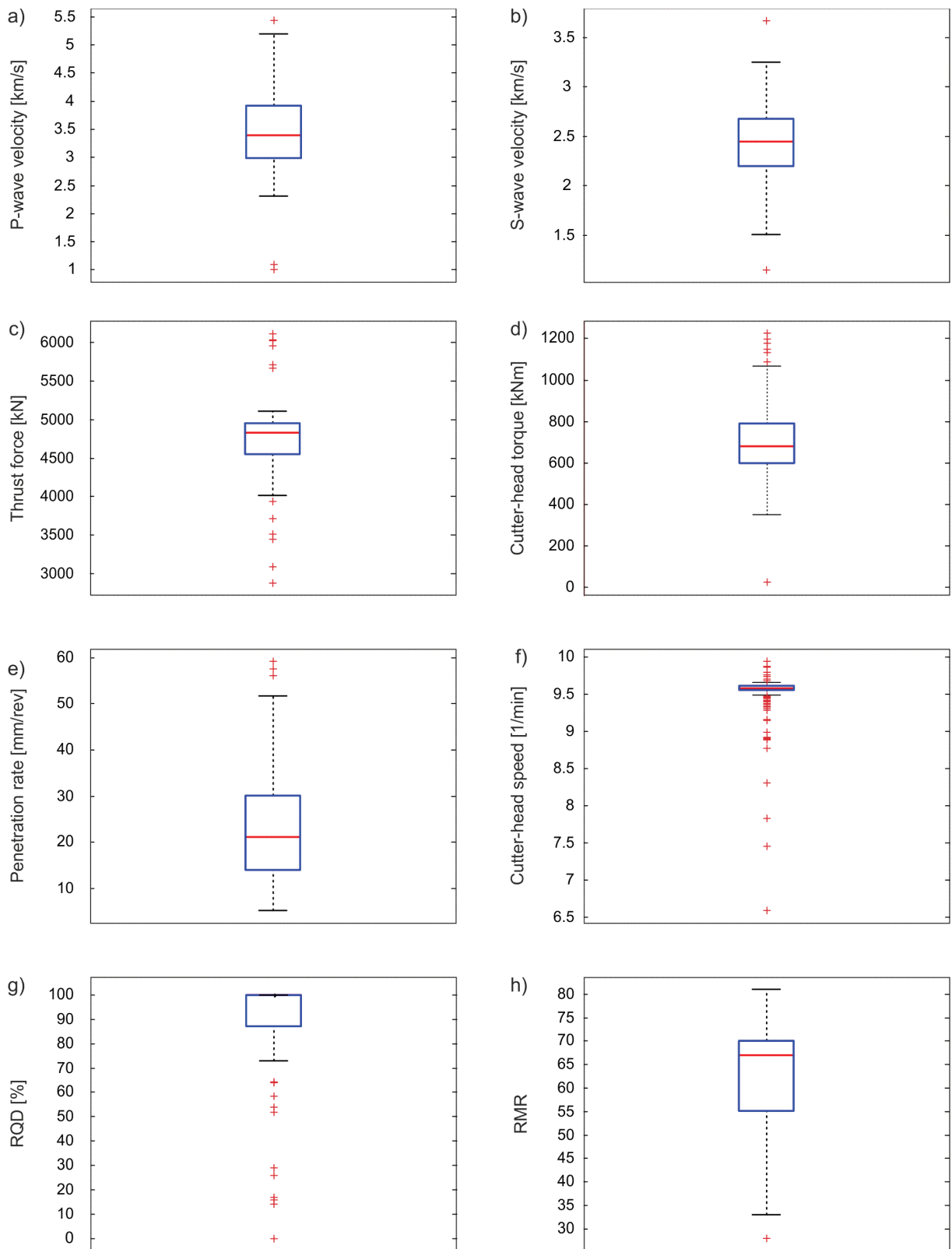


Figure 8.4: Boxplots of the tunnel-driving parameter and the target parameters, RQD and RMR, of the Glendoe Tunnel "4-m data set".

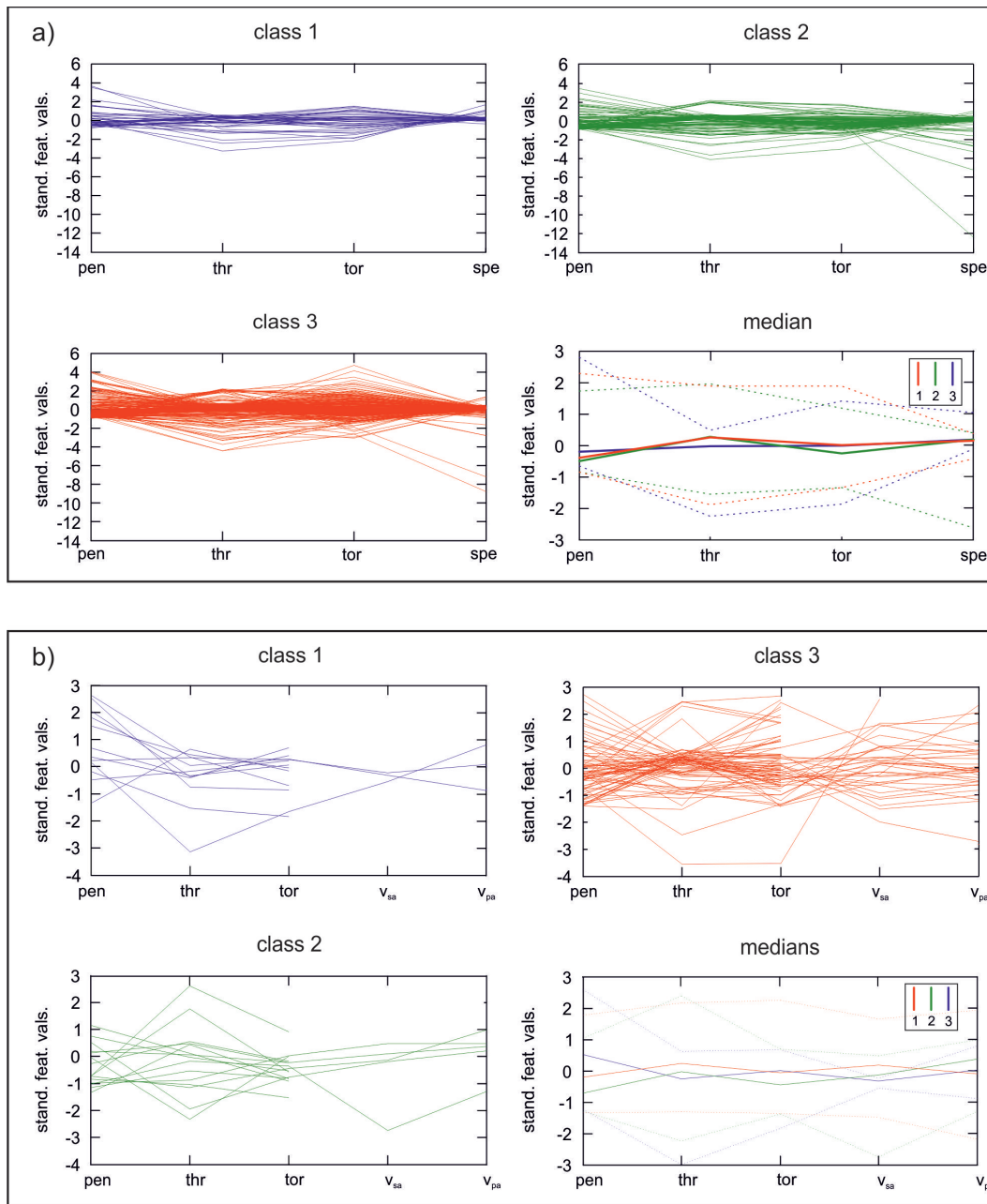


Figure 8.5: Parallel coordinate plots for the RQD classification on the Glendoe tunnel survey at (a) 1-m and (b) 4-m sample interval. Each observational point in the n -dimensional space is represented as a polyline for which the intercepts with the vertical axes are the seismic velocities. The observational points are colored according to the class label attributed to the specific data points. Each feature is scaled to have a mean of 0 and a standard deviation of 1. In (a) the tunnel-driving parameters are the intercepts with the vertical axes because they form the basis for the classification tasks on the GT-1-m data set. The patterns in (a) show only slight differences between the classes. The cutter-head drive bundles nearly all parallel into one point, with the exception of a few outliers. In (b) both tunnel-driving parameters and seismic velocities are included in the feature matrix and show thus intercepts with the vertical axes. The sparse character of the data base and the high amount of missing values in the seismic data is visible.

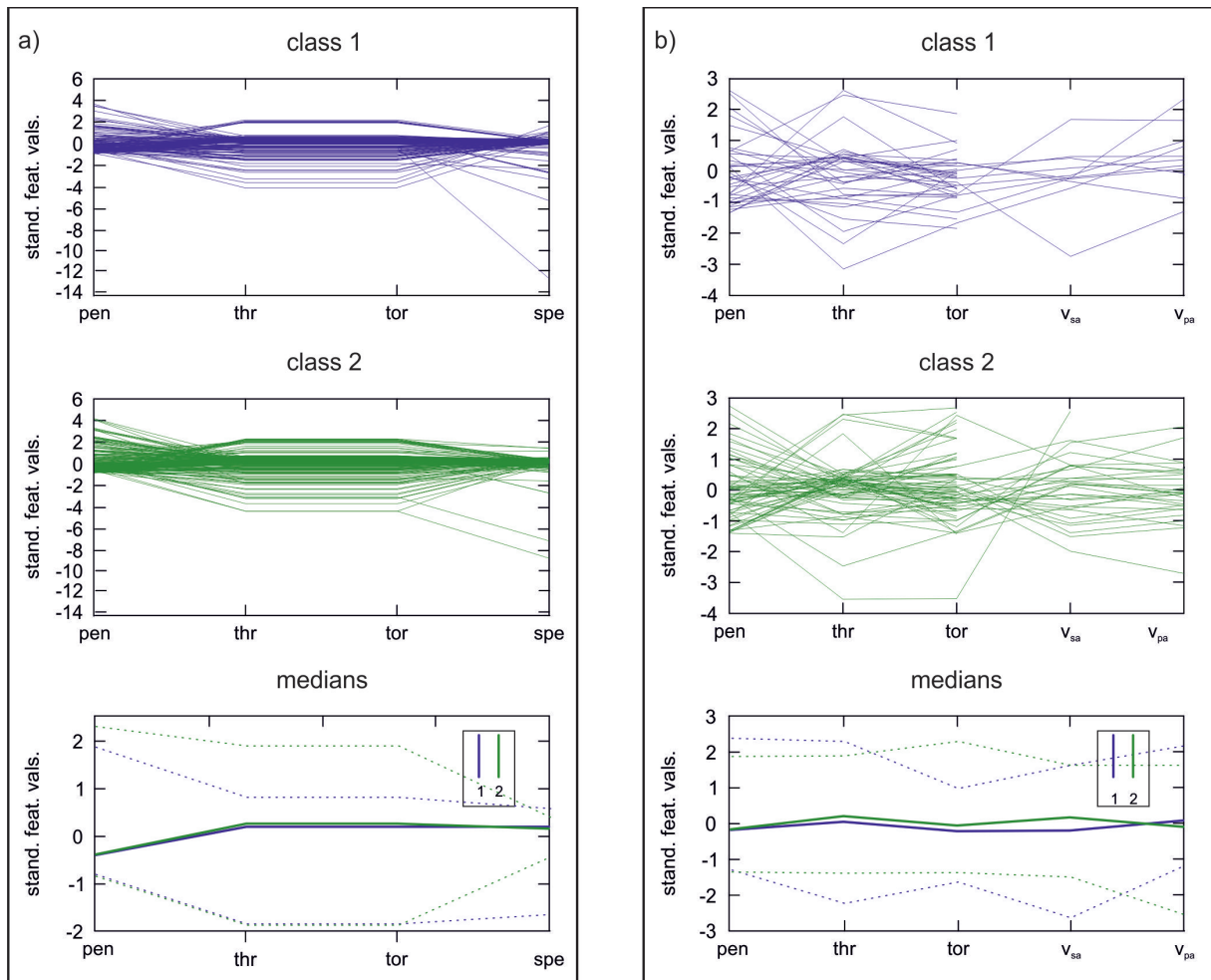


Figure 8.6: Parallel coordinates for the RMR classification on the Glendoe Tunnel data set for both 1-m and 4-m sample interval. Each observational point in the n -dimensional space is represented as a polyline for which the intercepts with the vertical axes are the seismic velocities. The observational points are colored according to the class label attributed to the specific data points. Each feature is scaled to have a mean of 0 and a standard deviation of 1. Only one "low" class ($RMR \leq 60$) and one high class ($RMR > 60$) were defined because of the concentration of the values close to $RMR = 60$ classes. (a) Even though the data is separated in merely 2 classes, the parallel coordinate plot for the 1-m sample interval does not show distinct patterns for Class 1 or Class 2 in the features. In (b) both tunnel-driving parameters and seismic velocities are included in the feature matrix and show thus intercepts with the vertical axes. The sparse character of the data base and the high amount of missing values in the seismic data is visible, just as for the GT-4-m-RQD classification.

Curriculum Vitae

Der Lebenslauf ist in der Online-Version
aus Gründen des Datenschutzes nicht enthalten.

